2000

The absorption spectrum of the hydrogen atom in crossed electric and magnetic fields

Dongmei Wang
College of William & Mary - Arts & Sciences

INFORMATION TO USERS

This manuscript has been reproduced from the microfilm master. UMI films the text directly from the original or copy submitted. Thus, some thesis and dissertation copies are in typewriter face, while others may be from any type of computer printer.

The quality of this reproduction is dependent upon the quality of the copy submitted. Broken or indistinct print, colored or poor quality illustrations and photographs, print bleedthrough, substandard margins, and improper alignment can adversely affect reproduction.

In the unlikely event that the author did not send UMI a complete manuscript and there are missing pages, these will be noted. Also, if unauthorized copyright material had to be removed, a note will indicate the deletion.

Oversize materials (e.g., maps, drawings, charts) are reproduced by sectioning the original, beginning at the upper left-hand corner and continuing from left to right in equal sections with small overlaps.

Photographs included in the original manuscript have been reproduced xerographically in this copy. Higher quality 6" x 9" black and white photographic prints are available for any photographs or illustrations appearing in this copy for an additional charge. Contact UMI directly to order.

Bell & Howell Information and Learning
300 North Zeeb Road, Ann Arbor, MI 48106-1346 USA
800-521-0600

UMI®

The Absorption Spectrum of the Hydrogen Atom in Crossed Electric and Magnetic Fields

---

A Dissertation

Presented to The Faculty of the Department of Physics

The College of William and Mary

In Partial Fulfillment

Of the Requirements for the Degree of

Doctor of Philosophy

By

Dongmei Wang

July 2000

APPROVAL SHEET

This dissertation is submitted in partial fulfillment
of the requirements for the degree of

Doctor of Philosophy.

Dongmei Wang

Approved, July 2000

John B. Delos

Roy L. Champion

William E. Cooke

Stephen K. Knudson
Chemistry Department

Robert G. Voigt
Computational Science

To My Parents

and

My Husband

Contents

Acknowledgments viii

Abstract viii

Chapter 1 Introduction 2

1.1 Where I am . . . 2

1.2 The advances in quantum chaos . . . 4

1.2.1 The correspondence between the classical trajectories and wave functions . . . 4

1.2.2 The correspondence between the large scale structure in the quantum spectrum and the periodic orbits . . . 8

1.2.3 The correspondence between the large scale structure in the absorption spectrum and the closed orbits . . . 9

1.3 Thesis objectives . . . 11

1.3.1 The crossed fields system . . . 11

1.3.2 Experimental measurements . . . 11

1.3.3 Thesis objectives . . . 13

1.4 Thesis contributions . . . 15

1.5 Thesis outline . . . 16

Chapter 2 The Hamiltonian and Monte-Carlo simulation 18

2.1 The rescaling of the Hamiltonian and the symmetries in the Hamiltonian . 19

2.2 The regularizing of the Hamiltonian . . . 22

2.3 Monte-Carlo simulation – Poincaré surface of section . . . 25

2.3.1 The reduced 2-D Hamiltonian . . . 25

2.3.2 Poincaré surface of section . . . 26

2.4 The atomic units . . . 31

Chapter 3 The large scale structure in the absorption spectrum **33**
3.1 Closed orbit theory 34
3.2 The calculated absorption spectrum 37
3.3 Comparison between the theoretical and experimental absorption spectrum with the same resolution 41
3.4 Comparison between the theoretical and experimental recurrence spectrum 44
3.4.1 The conventional Fourier-Transform and its failure in the crossed field system 44
3.4.2 The basic idea of the Chirped-Fourier-Transform 46
3.4.3 The theory of the Chirped-Fourier-Transform 49
3.4.4 The application of the Chirped-Fourier-Transform to the crossed field system 55

Chapter 4 The continuum absorption **61**
4.1 The continuum threshold 61
4.2 The continuum intensity 65
4.2.1 Estimation of the critical time T_{crit} 69
4.2.2 Definition of the lifetime of a trajectory 70
4.2.3 Calculation of the lifetimes of the trajectories 70
4.2.4 Calculation of the continuum absorption 74

Chapter 5 The long-lived regular quasidiscrete states in the absorption spectrum **75**
5.1 Theory of the Fourier transform method 76
5.2 The computational procedure and techniques of EBK quantization 81
5.3 Semiclassical energy spectrum 90

Chapter 6 Organization and Bifurcations of planar closed orbits **94**
6.1 The observed sequence of bifurcations of the closed orbits 96
6.2 Two elementary periodic orbits and their role in the organization of planar motions 99
6.3 Poincaré half-map 99
6.3.1 Full Poincaré map 101
6.3.2 Poincaré half-map 101
6.3.3 Periodic orbits of the Poincaré half-map and the winding ratio of the periodic orbits 102
6.4 A model of the half-map 105
6.4.1 A model Hamiltonian 106

6.4.2 Normal sequence of bifurcations of closed orbits of the model Hamiltonian . . . 108
6.4.3 The bifurcation sequences of longer trajectories . . . 111
6.4.4 Truncated sequence of bifurcations of closed orbits of the model Hamiltonian . . . 112
6.4.5 Bifurcation sequence of closed orbits at fixed t and varying ω_0 . . . 113
6.4.6 Local bifurcations *vs.* regional sequences of bifurcations . . . 113
6.5 Local bifurcations and regional sequences of bifurcations in crossed field system 114
6.5.1 Creation and evolution of rational tori . . . 114
6.5.2 The sequence of the bifurcation patterns of closed orbits . . . 116
6.6 Some large scale connections of regional bifurcations . . . 121
6.6.1 The symmetry properties of the regularized two-dimensional Hamiltonian . . . 123
6.6.2 Some of the large scale connections of regional bifurcations . . . 124
6.7 The organization of the closed orbits . . . 125
6.8 summary . . . 128

Chapter 7 Summary and open problems **129**

Appendix A Another application of The Chirped-Fourier-Transform **132**

Appendix B Closed orbit theory **136**
B.1 The derivation of the closed orbit theory of the crossed field system . . . 136
B.2 The implementation of closed orbit theory . . . 141

Appendix C The derivation of the boundary between bound and free motions in an electric field **154**

Appendix D Proofs of the relation (6.4) and the two theorems **158**

Appendix E Algorithms and implementations **164**
E.1 Programs from Our Group and Internet . . . 164
E.1.1 Integration program for differential equations from our group . . . 165
E.1.2 The root finding program for a system of nonlinear equations . . . 166
E.1.3 A nonlinear function minimization program . . . 166
E.1.4 Fast-Fourier-Transform program . . . 167
E.2 Programs developed by myself . . . 168
E.2.1 General trajectory calculation program 1 . . . 168
E.2.2 Trajectory calculation program 2 . . . 170
E.2.3 Simulation program . . . 171

E.2.4 Closed-orbit searching program 1 172
E.2.5 Closed-orbit searching program 2 174
E.3 Closed-orbit parameter calculation subroutine 175
E.4 Least-square fit subroutine 177
E.5 Theoretical absorption spectrum calculation program 178
E.6 Lifetime calculation program 180
E.7 Continuum calculation program 182
E.8 Measured absorption spectrum convolution program 183
E.9 Chirped-Fourier-Transform program 184
E.10 The equal steplength time series calculation program 186
E.11 Torus's fundamental frequencies calculation program 1 187
E.12 Torus's fundamental frequencies calculation program 2 190
E.13 Torus's fundamental frequencies calculation program 3 192
E.14 Torus's action variables calculation program 193
E.15 Simple shell scripts 195

Bibliography **196**

Vita **200**

Acknowledgments

I would like to thank my advisor Dr. Delos for the enormous time he spent on guiding my research, the great effort he made to help me learn as much as possible, his encouragement which kept me going and helped me reach my academic goal, and his parental love which made me enjoy my stay in William and Mary very much.

I would like to thank Dr. Vladmir Kondratovich for helping me with the computer and Mathematica, and his useful suggestions on my project. I also would like to thank Dr. Marcus Beims and Dr. Michael Haggerty for helping with graphical software. I enjoyed working with all of them.

I thank Dr. Champion, Dr. Cook and Dr. Voigt for sitting in my annual review. Their comments and suggestions helped me keep up my steps. I thank all of them and Dr. Knudson for agreeing to review my dissertation and serve on my committee.

I would like to thank Ms. Dianne Fannin, Ms. Paula Perry, Ms. Sylvia Stout for their knowledgeable help.

My acknowledgment finally comes to my husband – Guangzhi who played a very important role in helping me arrive at this point. His persistent love, comfort and drive supported me to overcome all kinds of difficulties and reach my goal. I thank him the most.

I also wish to thank my department for providing me the chance to study and do research. And I thank all professors who taught me the knowledge and helped me in all respects.

Abstract

This dissertation reports the theoretical interpretation of the measured absorption spectrum of hydrogen atoms in crossed electric and magnetic fields. Closed-orbit theory is modified from two-dimensions to three-dimensions to interpret the large scale structure in the absorption spectrum. A new computational method — a Chirped-Fourier-Transform — is developed to extract the closed orbits from an energy spectrum. A quantitative model is provided to calculate the continuum absorption. We prove that the observed continuum absorption is proportional to the flux of electrons along trajectories which escape within a short time. Einstein-Brillouin-Keller (EBK) quantization theory is applied to obtain an approximate energy spectrum. Our results prove that some of the observed regular quasidiscrete states correspond to quantized regular tori. This thesis also includes a new theoretical study of bifurcation patterns of planar closed orbits.

The Absorption Spectrum of the Hydrogen Atom in Crossed Electric and Magnetic Fields

Chapter 1

Introduction

This chapter provides a road map of this thesis, including a general idea about my research area (quantum chaos), my research problem (the hydrogen atom in crossed fields), and my research results. The details of mathematical derivations and computational methods are presented in the following chapters. For those who want to understand my research projects and contributions in a few minutes, this chapter should provide adequate information; for those who want to know more about my research, this chapter is also a good starting place.

1.1 Where I am

There are two descriptions of dynamical systems: classical mechanics and quantum mechanics. Classical dynamics is governed by Newton's Laws and quantum dynamics is governed by Schrödinger equations. Classical systems can be classified into linear and nonlinear systems: all the linear systems are regular, but nonlinear systems can be regular or chaotic. We are studying quantum chaos - those quantum systems whose classical analogue is chaotic. Our mission is to explore the connections between classical mechanics and

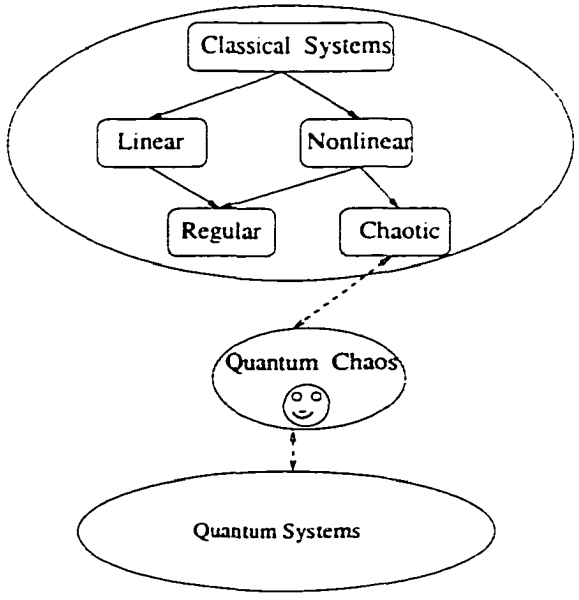

Figure 1.1: Research direction.

quantum mechanics and find the regular patterns hidden behind the chaos (Fig. 1.1).

A highly excited hydrogen atom in the presence of external, static fields is an ideal system to study quantum chaos since it is theoretically simple and experimentally approachable. The system we study in this thesis – the hydrogen atom in a crossed electric and magnetic field – is a good example. On the theoretical side, its exact Hamiltonian can be written down; on the experimental side, the transition of this system from order to chaos can be observed if the atom is excited to high Rydberg states with $n \geq 40$ with magnetic field $B \approx 6T$ and electric field $F \approx 10^5 V/m$.

The purpose of the work reported in this thesis is to study correlations between calculated classical trajectories and the observations of the absorption spectrum of this system. Although similar studies have been carried out for other systems [1–5], hydrogen in a crossed electric and magnetic field provides a more general testing ground for these

connections since it is the simplest, chaotic atomic system with three strongly coupled degrees of freedom. To make this thesis easy to follow, we first give a quick review of the main advances in quantum chaos since they form the foundation of this thesis work.

1.2 The advances in quantum chaos

1.2.1 The correspondence between the classical trajectories and wave functions

Classical mechanics describes the motions of the particles by classical trajectories, and quantum mechanics describes the motions of the particles by waves. De Broglies's matter wave theory unifies these two different descriptions: the momentum p of the classical motion is related to the wave length λ of the quantum propagation:

$$p = h/\lambda.$$

Therefore, as a wave propagates a distance dq along a classical trajectory, the phase change of a quantum wave is given by:

$$d\phi = 2\pi \frac{dq}{\lambda} = p \cdot dq/\hbar.$$

Then the phase of the wave following a classical path is given by:

$$\phi(q) = S(q)/\hbar + const.$$

where $S(q) = \int^q p \cdot dq$ is the classical action of the classical path. The amplitude of the wave function is related to the density of classical trajectories. Hence an approximate quantum wave function can be constructed from classical trajectories:

$$\psi(q) = \sqrt{\rho(q)} e^{iS(q)/\hbar}$$

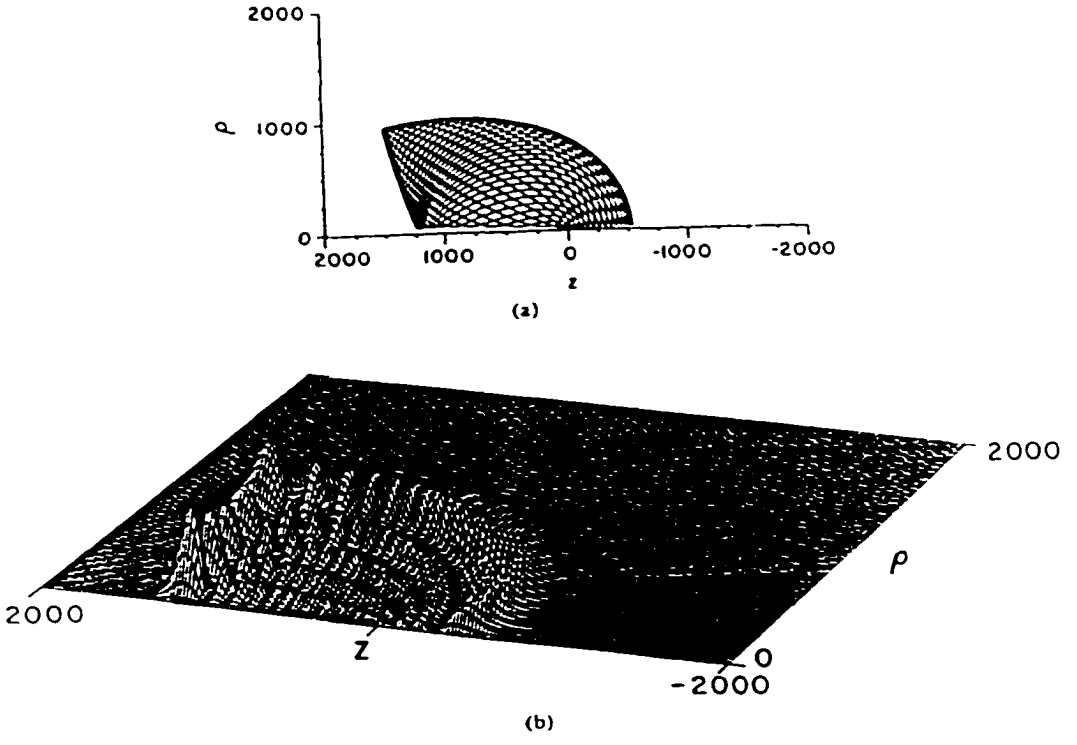

Figure 1.2: (a) A regular trajectory representing the motion of the atomic electron in $H(n = 30)$ in a magnetic field of a few teslas. (b) The exact quantum wave function $|\psi(q)|^2$ correlated with the trajectory in (a).

where $\rho(q)$ is the density of the classical trajectories as a function of q. Details about the construction of wave functions from classical trajectories are presented in [6]. Fig. 1.2 provides an example of the correspondence between a regular trajectory and a wave function. Both the trajectory and the wave function are calculated for an electron in a hydrogen atom in a magnetic field $B \approx$ a few teslas. The trajectory moves in a certain region of configuration space; the boundaries of the trajectory are called caustics. The wave function occupies the same region of space as the classical trajectory, and waves propagate in the same directions along which the classical trajectory goes. Four traveling waves pass through each point in the space and the interference of the four waves produces a standing wave. Due to the tunneling effect, the standing wave slightly spills over the classical boundary.

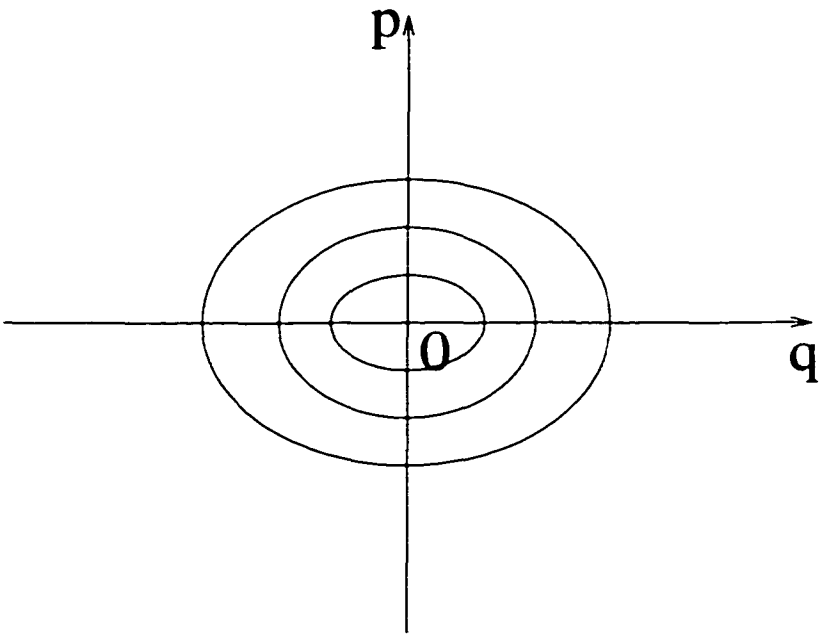

Figure 1.3: For a harmonic oscillator, the trajectories in phase space are ellipses, or "one-dimensional tori". The action variable for each torus $\oint pdq$, is the area inside the ellipse, and it is proportional to the energy. For a continuous range of energy, the tori form a continuous family. Quantum states correspond to a discrete set of tori having quantized values of the action.

For an n-dimensional system, a regular trajectory fills up an n-dimensional torus in 2n-dimensional phase space. An n-dimensional torus is an object which can be described by n angular variables varying from 0 to 2π and n constant action variables. On the torus, we can find n independent closed loops c_i and the n action variables are defined by:

$$I_i = \oint_{c_i} p \cdot dq/2\pi \tag{1.1}$$

Classical tori form continuous families defined by values of the action variables, and in these families lie a discrete set of tori whose action variables are appropriately quantized - either integer or half integer (see Fig.1.3 and Fig.1.4). We call these quantized tori eigentori.

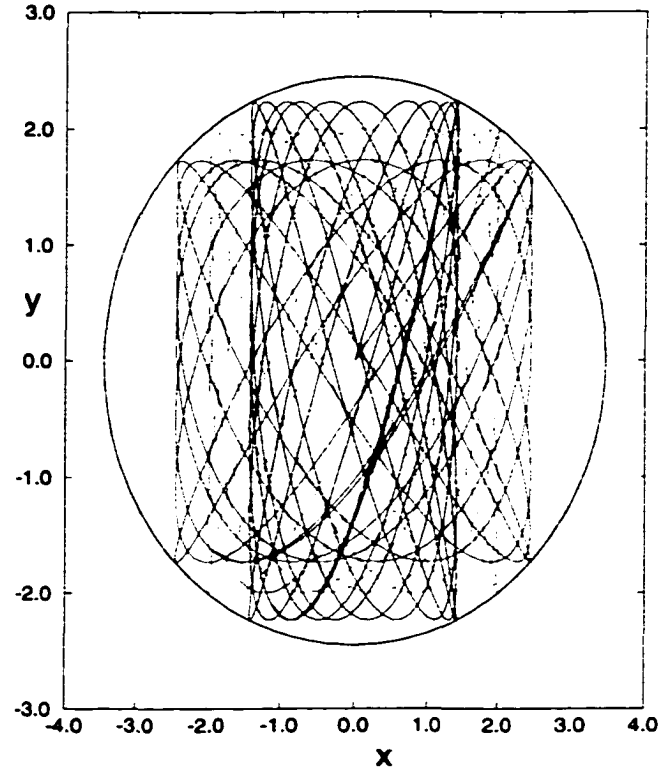

Figure 1.4: For a two-dimensional harmonic oscillator, the trajectories in (x, p_x) space and in (y, p_y) space form ellipses, and the combined motion is a two-dimensional torus. In (x, y) space, each trajectory fills a rectangle with corners on the equipotential curve $E = \frac{1}{2}k_x x^2 + \frac{1}{2}k_y y^2$. At each total energy, the orbits form a continuous family of rectangles with varying amplitudes of x and y oscillations, and therefore varying action variables. Quantum states correspond to tori of quantized actions $I_x = \frac{1}{2\pi}\oint_{c_x} p_x dx = (n_x + 1/2)$ and $I_y = \frac{1}{2\pi}\oint_{c_y} p_y dy = (n_y + 1/2)$ where c_x is a horizontal line which goes from the left side to the right side of the rectangle and c_y is a vertical line which goes from the top to the bottom side of the rectangle.

The Einstein-Brillouin-Keller (EBK) quantization theory states that each eigenstate for an N dimensional regular system corresponds to an eigentorus with n quantized action variables I_i,

$$I_i = n_i + \mu_i/4. \tag{1.2}$$

Then the phase change of the wave around the closed loop c_i is:

$$\Delta\phi = \oint_{c_i} p \cdot dq = (n_i + \mu_i/4)2\pi \tag{1.3}$$

Eq. (1.3) implies that each closed loop should contain an integer number or half integer number of waves. That is, each eigenstate corresponds to an n dimensional torus which can support a standing wave along each dimension. The additional half integer phase $\mu_i\pi/2$ results from quantum tunneling and μ_i is the Maslov index which is the number of the times that the closed loop touches caustics. A detailed discussion about the determination of the μ_i is provided in [7].

1.2.2 The correspondence between the large scale structure in the quantum spectrum and the periodic orbits

Fig. 1.5 shows energy levels of a typical model Hamiltonian system, defined in Appendix A. We see that the quantum states are clustered, that is, the density of quantum states is varying with respect to the energy. Periodic Orbit Theory relates the variation in the density-of-states to classical periodic orbits. Each periodic orbit produces one sinusoidal oscillation in the density $\rho(E)$ as a function of energy. The sum of all contributions from periodic orbits with period $T_k \leq T_m$ gives the quantum spectrum with resolution $\Delta E = 2\pi\hbar/T_m$.

$$\rho(E) = \rho_0(E) + \rho_{osc}(E) = \rho_0(E) + \sum_k a_k(E) sin[S_k(E)/\hbar + \phi_k]$$

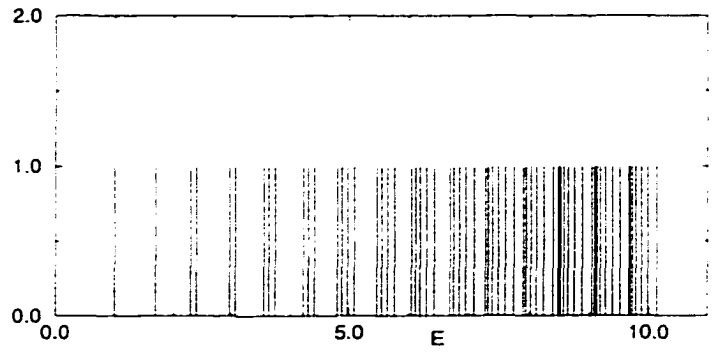

Figure 1.5: Energy spectrum of the model Hamiltonian in appendix A. Units are not defined for this model.

where $\rho_0(E)$ is a smooth "background" density, which is proportional to the volume in phase space. The oscillatory terms arise from periodic classical orbits. The coefficients $a_k(E)$ are related to the density of the classical trajectories near the periodic orbits. S_k is the classical action associated with the kth periodic orbit, and ϕ_k is an additional phase constant. The detailed derivation of Periodic Orbit Theory is discussed in [8].

1.2.3 The correspondence between the large scale structure in the absorption spectrum and the closed orbits

Experiments measure the oscillator strength density with finite resolution. The oscillator strength density is proportional to the rate of the production of atoms in excited quantum states. The measurement of the absorption spectrum of the hydrogen atom in a magnetic field shows large scale oscillatory structure at very high energies [1] (indicated by an arrow in Fig. 1.6). In 1988, Du and Delos established a Closed Orbit Theory to interpret this large scale structure (Trajectories which start and end at the origin are called closed orbits). They found that each closed orbit produces one sinusoidal oscillation in the absorption spectrum and the sum of the contributions from the closed orbits results in the

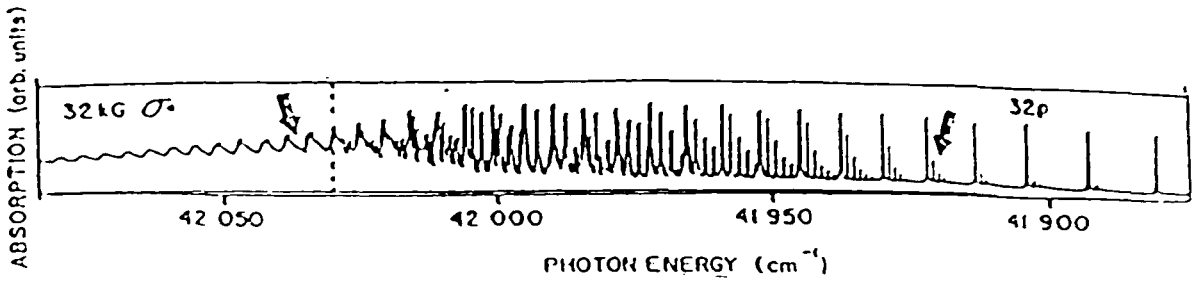

Figure 1.6: The measured absorption spectrum of the hydrogen atom in magnetic field.

oscillatory structure in the absorption spectrum [1,2].

$$Abs(E) = Abs_0(E) + \sum_{k_m} C_{m,k_m} sin(T_{mk_m} E + \Delta_{mk_m})$$

Again we have a smooth background $Abs_0(E)$ plus a sum of sinusoidal oscillations. This theory is different from Periodic Orbit Theory because it provides a quantitative formula for the absorption spectrum which can be compared with the experiment directly. The original purpose of the closed orbit theory was to interpret the measured absorption spectrum of the hydrogen atom in a strong magnetic field, but with some modifications, it also has been successfully applied to other systems [2–5]. Usually it has been applied to systems having cylindrical symmetry in which the number of degrees of freedom is reduced to two.

In this thesis, we extend and modify the closed orbit theory and apply it to a system with three degrees of freedom – the hydrogen atom in crossed electric and magnetic fields.

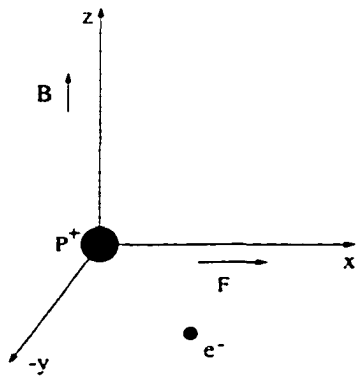

Figure 1.7: The hydrogen atom in crossed electric and magnetic fields

1.3 Thesis objectives

1.3.1 The crossed fields system

We define coordinates so that the electric field, F, is along the $+x$ direction and the magnetic field, B, is along the $+z$ direction (see Fig. 1.7). We assume that the proton is stationary [9]. The Hamiltonian function for the electron in the field of the proton and the applied fields is given in atomic units by:

$$\hat{H} = \frac{\hat{P}^2}{2} - \frac{1}{\hat{r}} + F\hat{x} + \frac{B}{2}\hat{L}_z + \frac{B^2}{8}(\hat{x}^2 + \hat{y}^2) \tag{1.4}$$

Due to the electric field force, the electron may escape from the proton and due to the strong magnetic force, the motion of the electron may be chaotic. Hence our system admits both chaos and field ionization.

1.3.2 Experimental measurements

Measurements of the absorption spectrum of the hydrogen atom in crossed electric and magnetic fields were done by the Bielefeld group in Germany [10].

They excited deuterium atoms to high energies in two steps: In the first step, $D(1s)$ absorbs a photon and goes to $D(2p)$ using an excimer-laser-pumped dye-laser, frequency tripled to $121.6nm$, with $\Delta\nu_1 \approx 1.8GHz$. In the second step, $D(2p)$ absorbs a photon and goes to a high Rydberg state $D^*(n, m_l = 0)$ by an excimer-laser-pumped dye-laser, seeded by a single-frequency Ti-Sa-laser, frequency doubled to $\lambda_2 \approx 365nm$, with $\Delta\nu_2 \approx 180MHz$. Both lasers are linearly polarized along the magnetic-field axis, which we call the z-axis.

Electrons from atoms promptly ionized within the interaction region (short-lived states) are prevented from E×B-drift by turning off the electric field about $120ns$ after excitation; after trapping them for about $3.5\mu s$ they are guided by the ring-electrodes to the detector, arriving there about $3.5 - 18\mu s$ after the laser pulse. Meanwhile D^* atoms in long−lived states are continuing to move at thermal velocity, and they arrive at the grid about $30 - 180\mu s$ after the laser pulse. There they are detected via electrons created by field ionization.

In the process of switching off the electric field, the long-lived neutral atoms evolve, presumably adiabatically, from crossed-field states to pure-magnetic-field states. Long-lived neutral atoms were created at negative energies, and presumably remain at negative energies while the field is switched off, and therefore they are stable after $100ns$.

We say, then, that the "prompt" electrons are those which are excited to states having lifetimes less than or of order $100ns$. The "delayed" electrons therefore arise from crossed-field states having lifetimes greater than or of order $100ns$. The total absorption spectrum is the sum of the signals associated with prompt and delayed electrons. Spectra were measured over a wide range (-195 to +5 cm^{-1}) at $1KV/cm$, and then at higher resolution over a narrow range (-138 to -112 cm^{-1}) at $B = 6.002T$, $F = 750$ to $1000\ V/cm$ in steps of $50\ V/cm$. (see Fig. 1.8 and Fig. 1.9)

It is difficult to know whether the overall detection efficiencies of long-lived and short-

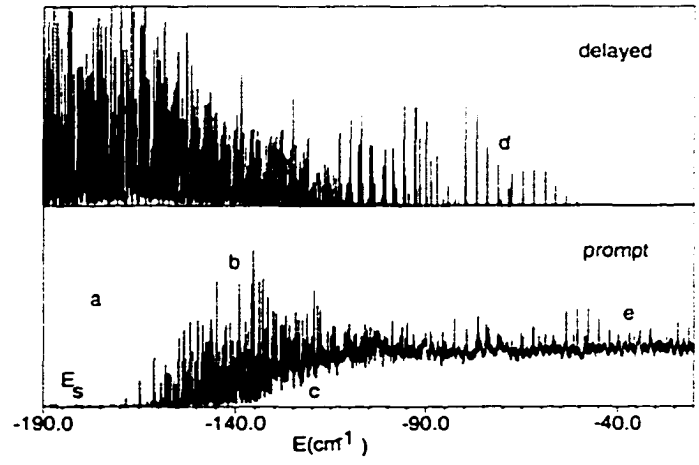

Figure 1.8: The measured prompt and delayed absorption spectrum at $B = 6.002T$, $F = 1000V/cm$. The dotted line marked E_s is the energy of the saddle point ($-193cm^{-1}$).

lived states are exactly equal. To test this, we smoothed the two data sets and summed them to see if the smoothed total absorption is reasonably independent of energy. The result suggested that we should multiply the delayed-electron signal by 1.43 before comparing it with the prompt-electron signal. We have done this in all of our calculations.

1.3.3 Thesis objectives

The main goal of this thesis is to interpret the measured absorption spectrum of the hydrogen atom in crossed electric and magnetic fields discussed above. We are particularly interested in understanding the following observations:

- In Fig. 1.9, the wiggly line is the convoluted spectrum. The oscillatory structure in that line indicates the oscillations in the absorption spectrum, and we call it the large scale structure. We want to understand the correlation between the large scale structure and the classical trajectories.

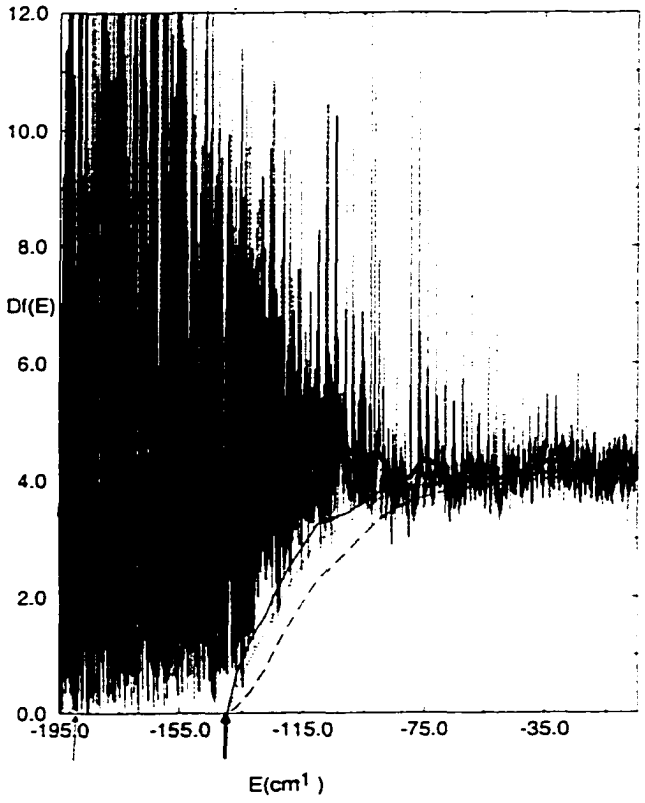

Figure 1.9: The measured total absorption spectrum at $B = 6.002T$, $F = 1000V/cm$. The wiggly line is a convolution of the measurement; its fluctuations are correlated with closed orbits. The other curves are calculations based on a model for continuum absorption, discussed in chapter 4. From lowest to highest, they have $T_{crit} = 15, 20$ and $25T_c$(respectively long-dashed line, dotted line and solid line). Light arrow: saddle energy E_s $(-193cm^{-1})$. Heavy arrow: vicinity of fuzzy threshold for continuum absorption $[-140, -135]cm^{-1}$.

- In the prompt signal (Fig. 1.8), the lower envelope of the spectrum is the zero axis at low energies near a, and it starts to rise at energies near b. As we continue to increase the energy, the lower envelope keeps increasing near c and finally flattens out at very high energies near d. We call the lower envelope "continuum absorption" and we want to find how it is correlated with trajectories that escape from the atom.

- In the delayed signal (Fig. 1.8), at low energies near a and b, the states are very dense. As we move to the region near c, individual states start to be visible and as we reach the region near d, the spectrum shows a regular pattern – the states are well separated and fall into a sequence with nearly equal spacings. We want to understand the regular pattern near d.

1.4 Thesis contributions

The main results of this thesis are summarized in following:

- Interpretation of the large scale structure: We have extended, modified and applied Closed Orbit Theory to interpret the large scale structure in the measured absorption spectrum of the crossed field system. We have proved that the observed large scale structure is correlated with short closed orbits, and each closed orbit produces one sinusoidal oscillation in the absorption spectrum. To extract the closed orbits from the absorption spectrum, we developed a new computational method – a Chirped-Fourier-Transform (CFT). We have applied this CFT to another system, and the result proves that CFT is a powerful way to extract sinusoidal waves with both varying amplitude and wavelength.

- Interpretation of the continuum absorption: we produced a model to calculate the continuum and showed that the intensity of the continuum absorption is proportional

to the flux of outgoing electrons that escape within 20-25 cyclotron times.

- Interpretation of the regular structure in the delayed signal at very high energies near d in Fig. 1.8: we applied EBK quantization theory to find the states which correspond to the 3-dimensional regular tori with quantized action variables. We found that the regular states in the delayed signal correspond to a group of quantized regular tori lying close to the xy plane (perpendicular to the magnetic field).

- In addition, we have studied properties of closed orbits that are not directly visible in the measurements: we studied the patterns of creation and splitting of planar closed orbits and identified an orderly sequence of bifurcations. A "tangent bifurcation" creates one closed orbit that splits into two; subsequently, one of them becomes periodic, and splits by a "pitchfork bifurcation" into two periodic orbits and one closed orbit. We created a model Hamiltonian to give a simple interpretation of this sequence of bifurcations.

1.5 Thesis outline

In chapter 2, we present transformations we made on the Hamiltonian – rescaling and regularization. Regularization is a method to get rid of the Coulomb singularity. This requires expanding the configuration space from three dimensions to four dimensions. We also give a brief discussion about the intuition we obtained about our system by Monte-Carlo simulation. Since we use atomic units for all the theoretical derivations and computations, we tabulate the values of the atomic units of the different quantities in terms of familiar units in this chapter as well.

In chapter 3, we focus on the interpretation of the large scale structure. We modify and extend Closed Orbit Theory from a 2-dimensional system theory to a 3-dimensional

system theory. We provide the schemes to implement the theory in a 4-dimensional space. Most of all, we discuss the new computational method – Chirped-Fourier-Transform (CFT) which was developed to extract the closed orbits from the measured absorption spectrum.

In chapter 4, we provide a model to interpret the continuum spectra and discuss the strategy used to carry out the calculation.

In chapter 5, we review the Fourier transform method invented by Martens and Ezra [11] which we use to quantize 3-dimensional tori. Also we apply the theory to obtain the states observed in the delayed absorption spectrum near region d in Fig. 1.8.

In chapter 6, we study the bifurcation patterns of the planar closed orbits and illustrate the pattern in the sequence of the bifurcations. We present a model Hamiltonian to help understand the new sequence.

In chapter 7, we summarize the contributions and discuss the remaining problems for our future work. The computational methods involved in this thesis are summarized in appendix E.

Chapter 2

The Hamiltonian and Monte-Carlo simulation

This chapter is devoted to the transformations of the Hamiltonian, including rescaling and regularizing. We also present some intuition about the crossed field system obtained by Monte-Carlo simulation.

As stated in chapter 1, the system we are studying is the hydrogen atom in crossed electric and magnetic fields, and the Hamiltonian is given by:

$$\hat{H} = \frac{\hat{P}^2}{2} - \frac{1}{\hat{r}} + F\hat{x} + \frac{B}{2}\hat{L}_z + \frac{B^2}{8}(\hat{x}^2 + \hat{y}^2) \tag{2.1}$$

where $\hat{H}$, F, B are three parameters. According to the classical rescaling law, we can rescale the variables and the parameters to eliminate one of the parameters.

Due to the Coulomb interaction, the Hamiltonian is singular at the origin. This singularity results in a numerical problem in trajectory calculations: when the electron approaches the origin, the large Coulomb interaction produces sharp bends of the orbit. To accurately follow the sharp bend, we have to use many small steps to do the integration near

the origin. The cost is that truncation and round-off error result in poor numerical precision. We apply a Kustaanheimo-Stiefel(KS) transformation [12] to get rid of the singularity.

The Hamiltonian has reflection symmetry with respect to the xy plane (which is perpendicular to the magnetic field direction), and therefore the trajectories which initially start and move in the xy plane stay in the xy plane forever. We use a Poincarè surface of section to study this group of motions by Monte-Carlo simulation, and obtain some intuition about the crossed field system.

2.1 The rescaling of the Hamiltonian and the symmetries in the Hamiltonian

Based on the classical rescaling law, we transform variables and parameters to new variables and parameters which are defined as the original ones multiplied by some power of the parameter we want to eliminate. Here we want to rescale everything by the magnetic field, therefore we transform the variables and the parameters in the following way:

$$f = FB^{\alpha}, \epsilon = EB^{\beta} \text{ or } H = \hat{H}B^{\beta}, r = \hat{r}B^{\gamma}, P = \hat{P}B^{\eta}$$

where f, ϵ are the rescaled electric field and energy, H is the rescaled Hamiltonian and r, P are coordinates and momenta. Inserting the transformations into the Hamiltonian (2.1), we obtain a new Hamiltonian in the rescaled variables and parameters:

$$H = B^{\beta-2\eta}\frac{P^2}{2} - B^{\beta+\gamma}\frac{1}{r} + B^{\beta-\alpha-\gamma}fx + B^{\beta-\eta-\gamma+1}L_z + \frac{1}{8}B^{\beta-2\gamma+2}(x^2+y^2)$$

Since we want to eliminate the parameter B from the rescaled Hamiltonian, we set all the exponents of B to zero, and solve for $\alpha, \beta, \gamma, \eta$:

$$\alpha = -4/3, \beta = -2/3, \gamma = 2/3, \eta = -1/3.$$

Therefore, we have

$$f = FB^{-4/3}, \epsilon = EB^{-2/3} \text{ or } H = \hat{H}B^{-2/3}, r = \hat{r}B^{2/3}, P = \hat{P}B^{-1/3}$$

which leads to the scaled Hamiltonian H:

$$H = \frac{P^2}{2} - \frac{1}{r} + fx + \frac{1}{2}L_z + \frac{1}{8}(x^2 + y^2) \tag{2.2}$$

This rescaling tells us that the classical properties of the trajectories are similar for all the values in E, F, B which lead to the same rescaled ϵ and f, i.e. the shapes of the trajectories depend only on ϵ and f, and the size varies with B such that the classical action is proportional to $B^{-1/3}$.

We know that the Hamiltonian has two symmetry properties which put some restrictions on the classical trajectories [15]:

- The reflection symmetry of the system with respect to the xy plane ($z \to -z$) results in two consequences: (a) any trajectory with initial position and velocity in the xy plane stays in the xy plane forever; therefore we can use a Poincarè surface of section to study trajectories in the xy subspace; (b) any trajectory which moves in the three dimensional space must have another sibling orbit which is the reflection of the trajectory with respect to the xy plane. Based on this property, we only need to study the trajectories launched in the upper half plane to study the orbits.

- The symmetry of reflection of the system with respect to the xz plane together with time reversal ($y \to -y, t \to -t$) results in a consequence: any closed orbit starting and ending at the origin is either symmetric with respect to the xz plane, or has another sibling closed orbit which is the time reversed reflection of the closed orbit with respect to the xz plane. Pictures of such orbits are shown in Fig. 2.1: the siblings are drawn in the same graph with different colors.

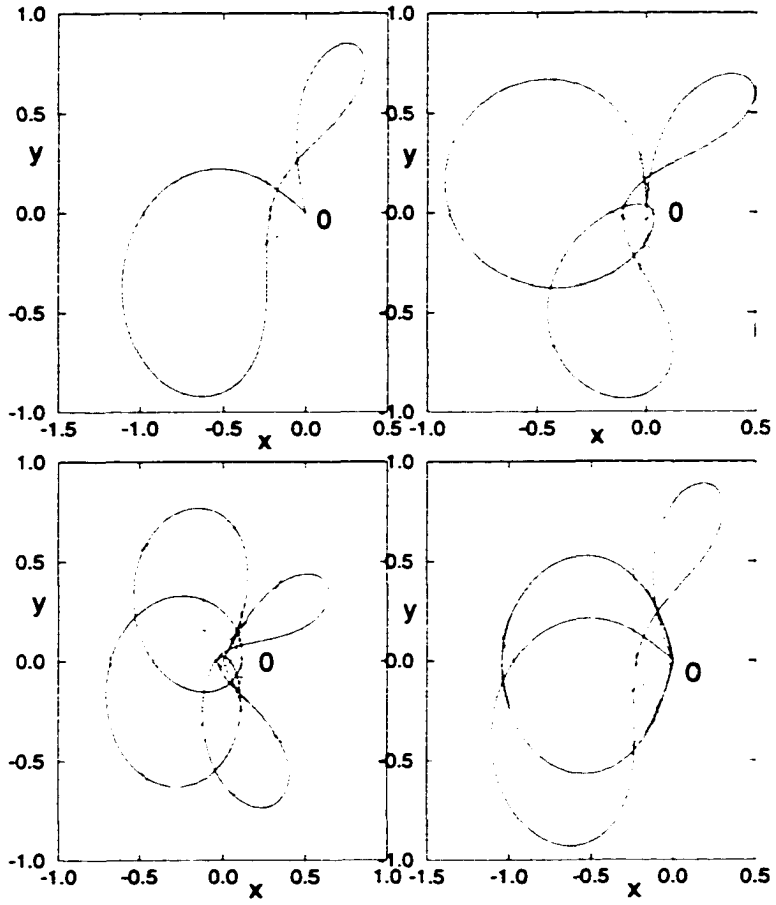

Figure 2.1: We show four pairs of the sibling trajectories. The siblings are drawn in the same graph with different colors

2.2 The regularizing of the Hamiltonian

A transformation for "regularizing" this system (eliminating the singularity) was invented by Kustaanheimo and Stiefel [12]. The transformation matrix is defined as

$$M_{KS} = \begin{bmatrix} u_1 & -u_2 & -u_3 & u_4 \\ u_2 & u_1 & -u_4 & -u_3 \\ u_3 & u_4 & u_1 & u_2 \\ u_4 & -u_3 & u_2 & -u_1 \end{bmatrix} \tag{2.3}$$

with (u_1, u_2, u_3, u_4), the coordinates in R_4. Then the coordinates (x, y, z) in the three-dimensional physical space are obtained as

$$\begin{bmatrix} z \\ x \\ y \\ 0 \end{bmatrix} = M_{KS} \begin{bmatrix} u_1 \\ u_2 \\ u_3 \\ u_4 \end{bmatrix} = \begin{bmatrix} u_1^2 - u_2^2 - u_3^2 + u_4^2 \\ 2u_1u_2 - 2u_3u_4 \\ 2u_1u_3 + 2u_2u_4 \\ 0 \end{bmatrix} \tag{2.4}$$

The variables $[u_1, u_2, u_3, u_4]$ determine $[z, x, y]$ uniquely, but the converse is not true. Since one of u's is arbitrary, we set u_4 initially to zero, then let its time-development be governed by equations of motion defined below.

In particular, the radius in the 3-D space equals

$$r = \sqrt{x^2 + y^2 + z^2} = u_1^2 + u_2^2 + u_3^2 + u_4^2.$$

The momenta (p_x, p_y, p_z) of the initial phase space R_6 are expressed in terms of coordinates (u_1, u_2, u_3, u_4) and conjugated momenta (p_1, p_2, p_3, p_4) in R_8 as

$$\begin{bmatrix} P_z \\ P_x \\ P_y \\ 0 \end{bmatrix} = \frac{M_{KS}}{2r} \begin{bmatrix} p_1 \\ p_2 \\ p_3 \\ p_4 \end{bmatrix} = \frac{1}{2r} \begin{bmatrix} u_1p_1 - u_2p_2 - u_3p_3 + u_4p_4 \\ u_2p_1 + u_1p_2 - u_4p_3 - u_3p_4 \\ u_3p_1 + u_4p_2 + u_1p_3 + u_2p_4 \\ u_4p_1 - u_3p_2 + u_2p_3 - u_1p_4 \end{bmatrix} \tag{2.5}$$

with

$$P_x^2 + P_y^2 + P_z^2 = (p_1^2 + p_2^2 + p_3^2 + p_4^2)/(4r)$$

One of the p's is arbitrary. It can be shown from the equations of motion that the quantity $u_4p_1 - u_3p_2 + u_2p_3 - u_1p_4$ is conserved. We choose the initial value of p_4, such that

$$u_4p_1 - u_3p_2 + u_2p_3 - u_1p_4 = 0 \tag{2.6}$$

Using the KS formula (2.4) and (2.5) together with condition (2.6), we can express the angular momentum

$$\vec{L} = \vec{r} \times \vec{P}$$

in the 3-space in terms of R_8:

$$L_z = u_1p_3 - u_3p_2 \tag{2.7}$$

$$L_x = (u_2p_4 + u_3p_1 - u_1p_3 - u_4p_2)/2 \tag{2.8}$$

$$L_y = (u_1p_2 + u_3p_4 - u_2p_1 - u_4p_3)/2 \tag{2.9}$$

The KS transformation is canonical in the sense that the Poisson brackets $[x_\alpha, P_\beta]$ and the equations of motion $\dot{x}_\alpha, \dot{P}_\alpha$ calculated with (u_1, u_2, u_3, u_4) and (p_1, p_2, p_3, p_4) all have the canonical form [16].

We substitute the formula (2.4) and (2.5) into the scaled Hamiltonian in (2.2) and regularize it by multiplying both sides by $4r$. We have

$$\begin{aligned} 4 &= p^2/2 - 4u^2c - 8f(u_2u_1 - u_4u_3)u^2 \\ &\quad +2(u_2p_3 - u_3p_2)u^2 + 2(u_2^2 + u_3^2)(u_1^2 + u_4^2)u^2 \end{aligned} \tag{2.10}$$

with $p^2 = p_1^2 + p_2^2 + p_3^2 + p_4^2$ and $u^2 = u_1^2 + u_2^2 + u_3^2 + u_4^2$. This regularization is equivalent to defining a new "fictitious time" variable s such that

$$\frac{dt}{ds} = 4r \tag{2.11}$$

After rescaling, the Hamiltonian becomes a constant and the rescaled energy ϵ becomes a parameter. The equations of motion in KS space are given by

$$
\begin{aligned}
u_1' &= p_1 \\
u_2' &= p_2 - 2u_3u^2 \\
u_3' &= p_3 + 2u_2u^2 \\
u_4' &= p_4 \\
p_1' &= 8u_1\epsilon + 8fu_2u^2 + 16f(u_2u_1 - u_4u_3)u_1 \\
&\quad -4(u_2p_3 - u_3p_2)u_1 - 4u_1(u_2^2 + u_3^2)u^2 \\
&\quad -4(u_2^2 + u_3^2)(u_1^2 + u_4^2)u_1 \\
p_2' &= 8u_2\epsilon + 8fu_1u^2 + 16f(u_2u_1 - u_4u_3)u_2 \\
&\quad -2p_3u^2 - 4(u_2p_3 - u_3p_2)u_2 - 4u_2(u_1^2 + u_4^2)u^2 \\
&\quad -4(u_2^2 + u_3^2)(u_1^2 + u_4^2)u_2 \\
p_3' &= 8u_3\epsilon - 8fu_4u^2 + 16f(u_2u_1 - u_4u_3)u_3 \\
&\quad +2p_2u^2 - 4(u_2p_3 - u_3p_2)u_3 - 4u_3(u_1^2 + u_4^2)u^2 \\
&\quad -4(u_2^2 + u_3^2)(u_1^2 + u_4^2)u_3 \\
p_4' &= 8u_4\epsilon - 8fu_3u^2 + 16f(u_2u_1 - u_4u_3)u_4 \\
&\quad -4(u_2p_3 - u_3p_2)u_4 - 4u_4(u_2^2 + u_3^2)u^2 \\
&\quad -4(u_2^2 + u_3^2)(u_1^2 + u_4^2)u_4
\end{aligned}
\tag{2.12}
$$

All the differentiations are with respect to the fictitious time s.

The lowest-order terms in (2.10) or (2.12) correspond to harmonic oscillation. Thus we have eliminated the singular behavior at the origin. The KS transformation is the classical expression of the close relationship between the 3-dimensional hydrogen atom and a four-dimensional harmonic oscillator. In embedding the system in a four-dimensional

space, the KS-transformation somewhat complicates calculations. However, the reward is smoother behavior and more accurate computations than obtained from the original Hamiltonian.

2.3 Monte-Carlo simulation – Poincaré surface of section

One of the effective ways to obtain intuition about a nonlinear system is calculating the Poincaré surface of section. In this section we use a Poincaré surface of section with Monte-Carlo simulation to study the group of motions which explore the xy plane.

2.3.1 The reduced 2-D Hamiltonian

In the rescaled Hamiltonian (2.2), if we set $z = 0$, the reduced 2-D Hamiltonian is given by [13, 14]:

$$H = \frac{P^2}{2} - \frac{1}{\rho} + fx + \frac{1}{2}L_z + \frac{1}{8}(x^2 + y^2) \tag{2.13}$$

with $\rho = \sqrt{x^2 + y^2}$.

For this Hamiltonian, we can make a canonical transformation to get rid of singularity without lifting the coordinate space to a higher dimension. The transformation is the semiparabolic coordinate transformation,

$$\begin{aligned} x = \frac{1}{2}(U^2 - V^2) \qquad & P_x = \frac{UP_U - VP_V}{U^2 + V^2}, \\ y = UV \qquad & P_y = \frac{UP_V + VP_U}{U^2 + V^2}. \end{aligned} \tag{2.14}$$

We substitute this into Eq. (2.13), and multiply by U^2+V^2, and the Hamiltonian becomes:

$$2 = \frac{1}{2}(P_U^2+P_V^2)-(U^2+V^2)\epsilon+\frac{f}{2}(U^4-V^4)+\frac{1}{4}(UP_V-VP_U)(U^2+V^2)+\frac{1}{32}(U^2+V^2)^3 \tag{2.15}$$

This transformation corresponds to using a fictitious time:

$$dt/ds = U^2 + V^2.$$

Now the U axis is "uphill" while the V axis is "downhill" for the electric field.

Furthermore, we rescale the variables via another transformation:

$$U = u/\sqrt{\omega} \qquad P_U = p_u\sqrt{\omega}.$$
$$V = v/\sqrt{\omega} \qquad P_V = p_v\sqrt{\omega}. \tag{2.16}$$

The Hamiltonian changes to:

$$\frac{2}{\omega} = \frac{1}{2}(p_u^2+p_v^2)+\frac{1}{2}(u^2+v^2)+\frac{f}{2\omega^3}(u^4-v^4)+\frac{1}{4\omega^2}(up_v-vp_u)(u^2+v^2)+\frac{1}{32\omega^4}(u^2+v^2)^3 \tag{2.17}$$

with $\omega = \sqrt{-2\epsilon}$. The equations of motion are given by:

$$\begin{aligned}
u' &= p_u - \frac{1}{4\omega^2}v(u^2+v^2) \\
v' &= p_v + \frac{1}{4\omega^2}u(u^2+v^2) \\
p_u' &= -u - \frac{2f}{\omega^3}u^3 - \frac{1}{4\omega^2}p_v(u^2+v^2) - \frac{1}{2\omega^2}u(up_v-vp_u) - \frac{3}{16\omega^4}u(u^2+v^2)^2 \\
p_v' &= -v + \frac{2f}{\omega^3}v^3 + \frac{1}{4\omega^2}p_u(u^2+v^2) - \frac{1}{2\omega^2}v(up_v-vp_u) - \frac{3}{16\omega^4}v(u^2+v^2)^2
\end{aligned} \tag{2.18}$$

All the differentiations are with respect to the fictitious time s.

The coordinate transformations (2.14) and (2.16) together map the whole xy plane to the half (u, v) plane. Therefore, we only need to consider the trajectories launched with $u' > 0$ or $v' > 0$ to study the motions in the xy plane.

2.3.2 Poincaré surface of section

The Poincaré surface of section is defined in [17, 18]. For a physical system with n degrees of freedom, the phase space has 2n dimensions. Since the energy is conserved , we can reduce by one dimension. Usually we use n coordinates and n-1 momenta to represent the energy shell in phase space. In this (2n-1)-dimensional energy shell, we can select a 2n-2 dimensional surface of section S. Ideally, all trajectories will at some time pass through this

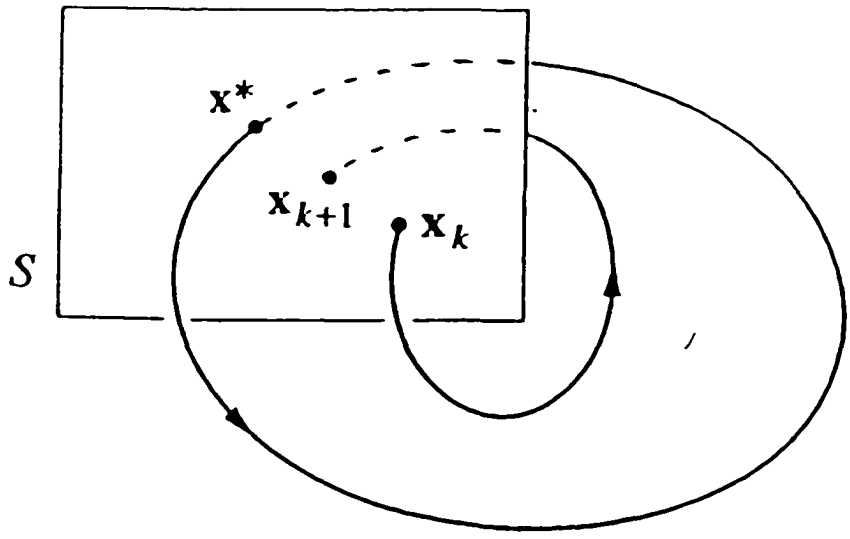

Figure 2.2: An illustration of the Poincaré surface of section

surface transversely, and no trajectory will ever touch the surface tangentially. We define a Poincaré map P which maps S to itself and is obtained by following the trajectories from one intersection with S to the next. If $x_k \in S$ denotes the kth intersection, then the Poincaré map is defined by

$$x_{k+1} = P(x_k).$$

The 2n-2 dimensional surface and the Poincaré map together are called the Poincaré surface of section (see Fig. 2.2).

The Poincarè surface of section is useful and practical to study both regular and chaotic motions of a two dimensional system. It condenses many trajectories onto a two dimensional surface, and converts the regular motions into smooth curves and chaotic motions into scattered dots. It converts periodic orbits into fixed points which might be easily located. Here, we use a Poincaré surface of section to obtain the evidence that the crossed

field system is a generic system, with order and chaos mixed.

To obtain the Poincaré surface of section, we first choose the surface as $v = 0$, and randomly pick initial values (u_i, p_{u_i}). Then we input $v = 0, u_i, p_{u_i}$ into (2.17) to calculate p_{v_i}. There are two solutions and we pick up the branch that gives $v' > 0$. We use those as initial values, and integrate the equations of motion (2.18). Whenever the trajectory passes through the surface with $v' \geq 0$, we record u and p_u, and make a dot in the (u, p_u) plane. We initiate twenty trajectories and integrate each of them until it makes two hundred dots on the surface to obtain Fig. 2.3. We have the following observations:

- There are two fixed points (S_+, S_-) which are two fundamental periodic orbits [13]. We draw them at various energies in Fig. 2.4. S_+ is a stable periodic orbit - as we increase the energy, S_+ changes in size, but it stays elliptical: S_- is stable at very low energies and becomes unstable at high energies. As we increase the energy, the shape of S_- dramatically changes: it is elliptical at very low energies (curve 1 in Fig. 2.4. As energy increases, it first develops a cusp on the negative x axis (curve 2), then the cusp becomes a loop (curve 3) and finally another cusp on the positive axis appears (curve 4).

- These two fundamental periodic orbits act as "organizers" of the xy-plane motions. The stable periodic orbit organizes the stable trajectories. All the trajectories around S_+ are regular tori at the energies we study. The tori around S_- are regular at low energies. As we increase the energy, the tori which are the closest to S_- go chaotic first, and more and more tori around S_- become chaotic as we continue to increase the energy. The chaotic trajectories launched in the white space in Fig. 2.3 go to ionization in a short time.

Hence we conclude that our system has a mixture of order and chaos plus ionization. Chaos

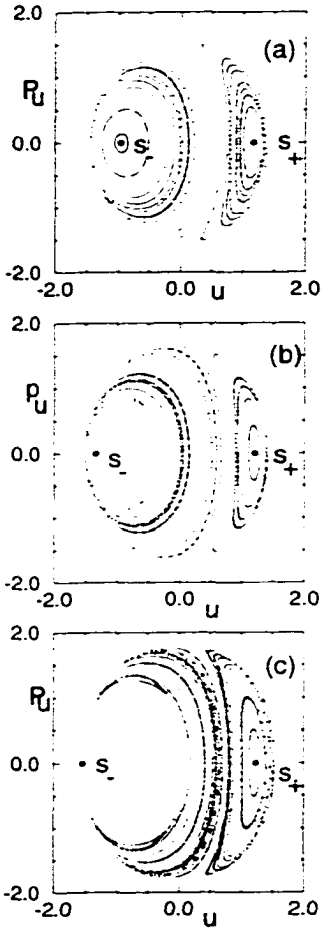

Figure 2.3: A collection of surface of section at three different energies with fixed external fields $B = 6T$, $F = 1000V/cm$: (a) $E = -250cm^{-1}$, (b) $E = -190cm^{-1}$, (c) $E = -140cm^{-1}$

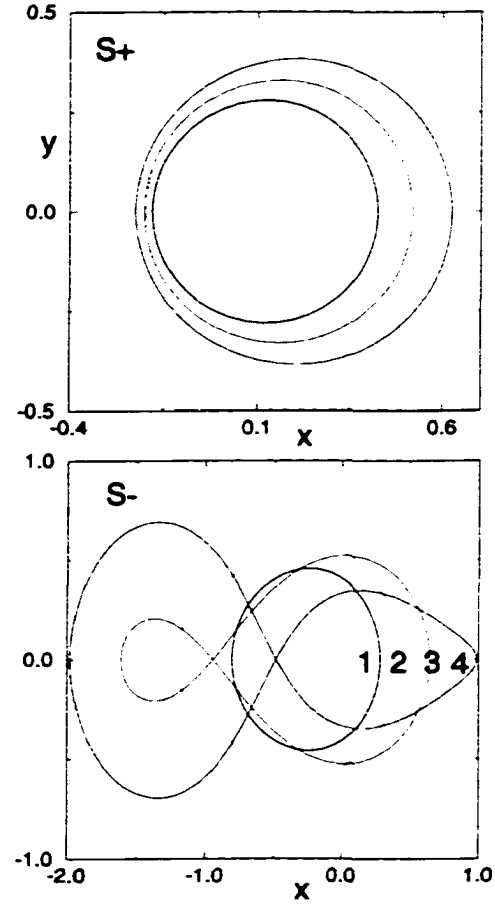

Figure 2.4: Two elementary periodic orbits at different energies with external fields $B = 6T$, $F = 1000V/cm$: $E = -250, -210, -190, -140cm^{-1}$ from curve 1 to 4.

increases as we increase the energy and many of the orbits in the large chaotic zone go to ionization in a short time.

2.4 The atomic units

In this thesis, we use atomic units for all the theoretical derivations and numerical computations. Therefore in this section, we define the meaning of the atomic units for the quantities involved in this thesis and tabulate the values of the atomic units of the different quantities in terms of familiar units.

1. The atomic unit of charge is the charge of the electron:

$$e = 1.60218 \times 10^{-19} C$$

2. The atomic unit of mass is the mass of the electron:

$$m_e = 9.10939 \times 10^{-31} kg$$

3. The atomic unit of angular momentum is the Plank constant:

$$\hbar = 1.05457 \times 10^{-34} Js$$

4. The atomic unit of length is the radius of the lowest orbit of the electron in a hydrogen atom:

$$a_0 = \frac{\hbar^2}{m_e e^2} = 5.28927 \times 10^{-11} m$$

5. The atomic unit of time is the time to go $1a_0$ at the speed of the electron in the lowest orbit. Since the speed in the lowest orbit is $e^2/\hbar$, the time to go $1a_0$ at this speed is:

$$\frac{a_0}{e^2/\hbar} = \frac{\hbar^3}{m_e e^4} = 2.41660 \times 10^{-17} s$$

6. The atomic unit of energy is defined as twice the lowest energy of the electron in a hydrogen atom:

$$\frac{m_e e^4}{\hbar^2} = 4.36388 \times 10^{-18} J = 27.2372 eV.$$

Also we can express it in wave number. Spectroscopists measure wavelength of light emitted in a transition from one state to another and report $K = 1/\lambda$. Since $\Delta E = h\nu = hc/\lambda = hcK$, wave-number is an effective energy unit:

- The atomic unit of energy expressed in wave-numbers is:

$$27.2372 eV/hc = 2.19682 \times 10^5 cm^{-1}.$$

7. The atomic unit of electric field is the electric field felt by an electron at $1a_0$ from a proton:

$$\frac{m_e^2 e^5}{\hbar^4} = 5.14951 \times 10^{11} V m^{-1}.$$

8. The atomic unit of the magnetic field can be derived from the known atomic units. It is the field which acts upon the electron moving at an atomic unit speed with an atomic unit force. Since the atomic unit of the force is the force felt by an electron at $1a_0$ from a proton which is $m_e^2 e^6/\hbar^4$, the atomic unit of the magnetic field is

$$\frac{m_e^2 e^3}{\hbar^3} = 2.35274 \times 10^5 T.$$

Chapter 3

The large scale structure in the absorption spectrum

In this chapter we first give a brief discussion about the modified closed orbit theory for the crossed field system. The detailed mathematical derivation of the closed orbit theory and its implementation are presented in appendix B. As we mentioned in chapter 1, a modified form of closed orbit theory can be used to describe the large-scale structure of the absorption spectrum of hydrogen atoms in crossed electric and magnetic fields. Then the direct comparison of the theoretical and experimental absorption spectrum with the same resolution is discussed in section 3.3. In order to compare the theoretical and experimental results in the time domain, we develop in section 3.4 a new computational method called a Chirped-Fourier-Transform (CFT) and apply it to extract the closed orbits from the measured absorption spectrum. Another application of CFT can be found in appendix A.

The closed orbit theory originally was established by Du and Delos [1] to interpret the large scale structure in the measured absorption spectrum of the hydrogen atom in a strong magnetic field. It relates the absorption spectrum of an atom to closed classical

orbits of the electron - orbits which go out from an atom and later return.

With some modification, closed-orbit theory has been successfully applied to many other atomic systems [2–5]. All these systems have cylindrical symmetry, such that these systems possess just two coupled non-integrable degrees of freedom. The crossed field system we are studying in this thesis is the first system with three non-integrable degrees of freedom. Hence we need to extend and modify the closed orbit theory from two dimensions to three dimensions.

To eliminate the singularity at the origin, we have lifted our system from a three dimensional Cartesian space to a four dimensional KS space. We will address the schemes of implementing the closed orbit theory in the KS space. Since each closed orbit produces one sinusoidal oscillation in the absorption spectrum, we try to extract individual sinusoidal oscillations to obtain signals of the closed orbits. In previous systems, ordinary Fourier-Transformation converted oscillations into well separated peaks. The Fourier-Transform of the absorption spectrum is called the recurrence spectrum, and the peaks in the recurrence spectrum provide a wealth of information about the closed orbits. In the current system, the ordinary Fourier transform fails. We develop a new computational technique called Chirped-Fourier-Transform to extract the oscillations produced by the closed orbits. We also show that this CFT has more general applications in data processing.

3.1 Closed orbit theory

In this section, we give a qualitative explanation of closed-orbit theory and a discussion of the differences between the modified closed orbit theory for the crossed field system and the closed orbit theory for the magnetic field only system. For more details, see appendix B.

The closed orbit theory was invented by Du and Delos [1] to interpret the oscillatory

structures in the absorption spectrum of hydrogen atoms in a strong magnetic field. The oscillatory structures can be understood by reviewing the absorption process of an atom in external fields: the atom initially in a low Rydberg state is excited by a laser (see (1) in Fig. 3.1). The excitation produces Coulomb waves, which propagate outward in all directions (see (2) in Fig. 3.1). When the wave propagates to the region far from the nucleus ($> 50a_0$), the propagation of the wave follows the classical trajectories (see (3), (4) in Fig. 3.1). Finally, the trajectories turn around and the waves return toward the atom (see (5), (6), (7), (8) and (9) in Fig. 3.1). Around $50a_0$, the returning wave continues to propagate inward as a Coulomb wave (see (10) in Fig. 3.1). The returning wave overlaps and interferes with the outgoing wave near the atom. The interference produces the oscillations in the absorption spectrum (see (11) in Fig. 3.1).

Closed orbit theory says that the oscillations in the absorption spectrum are correlated with the closed orbits which start and end at the origin. Each closed orbit produces one sinusoidal oscillation, and the sum of the contributions from the closed orbits gives the oscillatory structure in the absorption spectrum. Our derivation of the closed orbit theory for the crossed field system closely follows the method used in [1]. The only difference is that the approximations they made due to the cylindrical symmetry in magnetic field do not apply in crossed fields, so we discard those approximations in our derivation.

The quantitative formula for the absorption spectrum in crossed fields is given by:

$$Df(E) = Df_0(E) + \sum_j C_j(E) sin\Delta_j(E). \tag{3.1}$$

It is a smooth background plus a sum of oscillatory contributions from the closed orbits. The smooth term is the same as Eq. (5.10) in [1]b. In the oscillatory term, the phase is given by

$$\Delta_j = S_j(E)/h - \frac{\pi}{2}\mu_j, \tag{3.2}$$

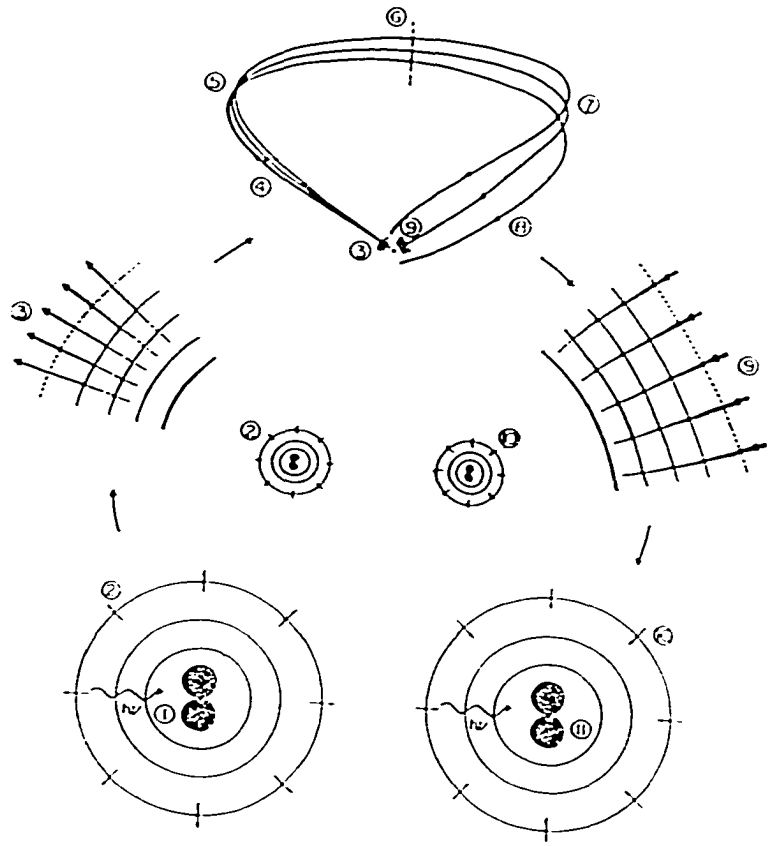

Figure 3.1: Physical picture of the absorption process. (1) The atom initially in a low energy state is excited by a laser; (2) The excitation produces zero-energy Coulomb waves, which propagate outward in all directions; (3) For distance greater than $50a_0$, waves propagate along the classical trajectories; (4) A ray of trajectories propagates outward, encounters a caustic (5), a focus (6), and another caustic (7), then turns around and returns toward the atom. Around $50a_0$, the incoming wave continues to propagate inward as an incoming Coulomb wave. The interference between the incoming and outgoing wave produces the oscillatory structures in the absorption spectrum.

and the amplitude is given by

$$C_j = (E - E_i)2^{9/2}\pi r_{out}^{-3/4} r_{ret}^{-1/4} A_j(q_{ret}^j) y^*(\theta_{ret}^j, \phi_{ret}^j) y(\theta_{out}^j, \phi_{out}^j) \tag{3.3}$$

with

$$y(\theta, \phi) = \sum_{l_1 m} (-1)^{l_1} I(n, l, l_1) b_{l_1,m} Y_{l_1 m}(\theta, \phi)$$

When we compare the C_j here with C_{m,k_m} in Eq. (5.13a) of [1]b, there are three differences:

1. C_j is much smaller than C_{m,k_m}. Because of the cylindrical symmetry in pure magnetic field case, each closed orbit stands for a family with the same polar angle and different azimuthal angle in the region $[0, 2\pi]$. However, in the crossed-fields system, each term comes from the contribution of an isolated closed orbit. Hence the effect of each closed orbit is much weaker in crossed-fields than in a pure magnetic field.

2. C_j depends on both polar and azimuthal angles. In contrast, again because of cylindrical symmetry in a pure magnetic field, C_{m,k_m} only depends on polar angle.

3. C_j includes the sum over both l (the magnitude of the angular momentum) and m (z component of the angular momentum). In the pure magnetic field case, since the z component of angular momentum is conserved, m is fixed, and C_{m,k_m} only includes a sum over l.

3.2 The calculated absorption spectrum

Applying the strategy discussed in appendix B, we can search for the closed orbits systematically. In Fig. 3.2, we show the twenty short closed orbits we found. Fifteen of them lie in the xy plane and are labeled P_i (planar); the remaining five of them explore three dimensional space and are labeled by S_i (spatial). As we mentioned in chapter 2, if a

xy plane closed orbit is asymmetric with respect to the xz plane or x axis, the time-reversed reflection of the closed orbit with respect to the x axis is a closed orbit as well. We call these two closed orbits a pair. $(P_4, P_5), (P_8, P_9), (P_{11}, P_{12}), (P_{14}, P_{15})$ drawn in Fig. 3.2 are some examples. Due to the z reflection symmetry, corresponding to each spatial closed orbit with initial $z' > 0$, we have another spatial closed orbit with initial $z' < 0$. These two orbits are reflections of each other through the xy plane. Here we show only the spatial closed orbits with initial $z' > 0$.

We first calculate the classical action $S_j(E)$, classical amplitude $A_j(E)$ and Maslov index $\mu_j(E)$ of each closed orbit at energies which go from -195 to $+5$ cm^{-1} with stepsize 1 cm^{-1} where $B = 6T$ and $F = 1KV/cm$. Then we input the $S_j(E)$, $A_j(E)$ and $\mu_j(E)$ into (3.1) to calculate the absorption produced by the jth closed orbit. Since the planar or spatial pairs have the same classical action, classical amplitude and Maslov index, we only calculate once and double contribution to the absorption. In Fig. 3.3, we show the contributions from the first two in-plane closed orbits labeled by P_1, P_2 and the first two spatial closed orbits labeled by S_1, S_2 individually and the sum of the contributions from the twenty closed orbits drawn in Fig. 3.2. The number of the trajectories included in the spectrum calculation is determined by the resolution we want to achieve. Here, twenty trajectories are enough to achieve the resolution $2cm^{-1}$.

The calculated absorption spectrum sharply rises near the bifurcation points where either a closed orbit disappears or a new closed orbit is created. In general, the oscillations produced by each isolated closed orbit are weak, and their wavelengths and amplitudes mostly decrease as the energy increases. These characteristics of the oscillations produced by the closed orbits create a new challenge for us to extract them from the experimental signal. We will discuss this challenge and our solution in section 3.4.

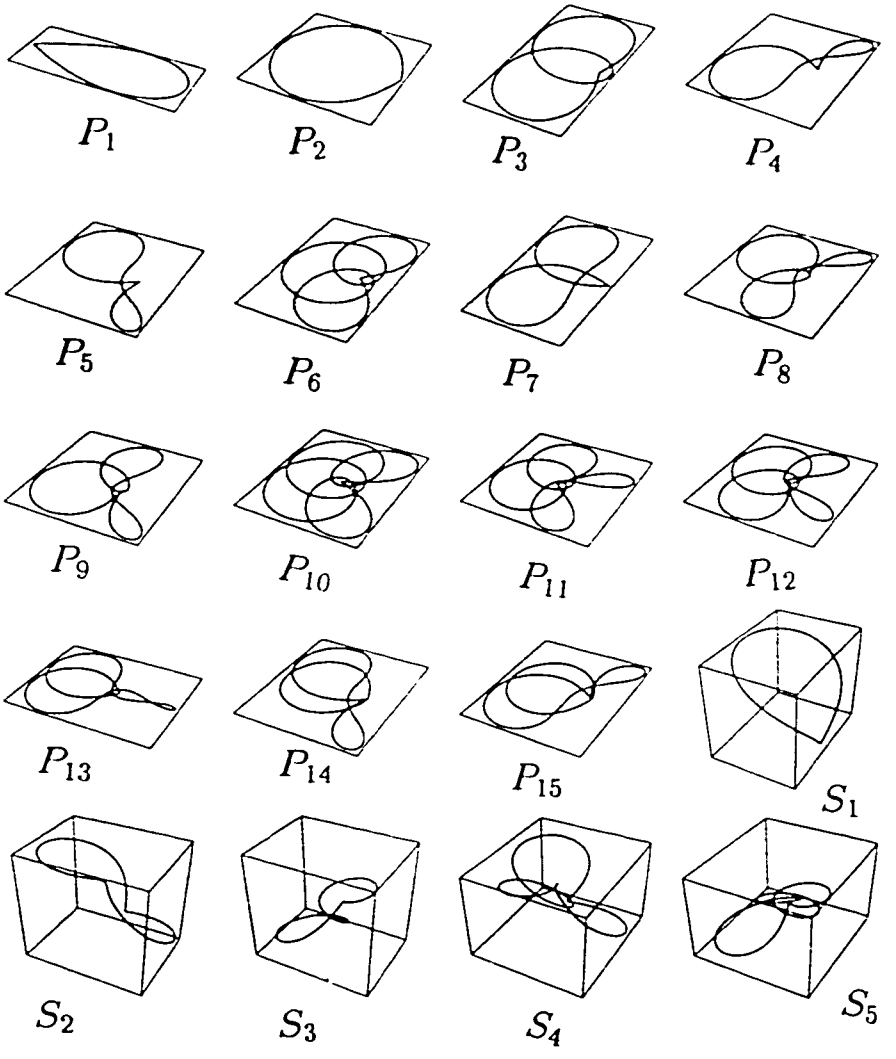

Figure 3.2: The twenty shortest closed orbits we found. Fifteen of them lie in the xy plane and we label them by P_i; the remaining five of them explore xyz space and we label them by S_i.

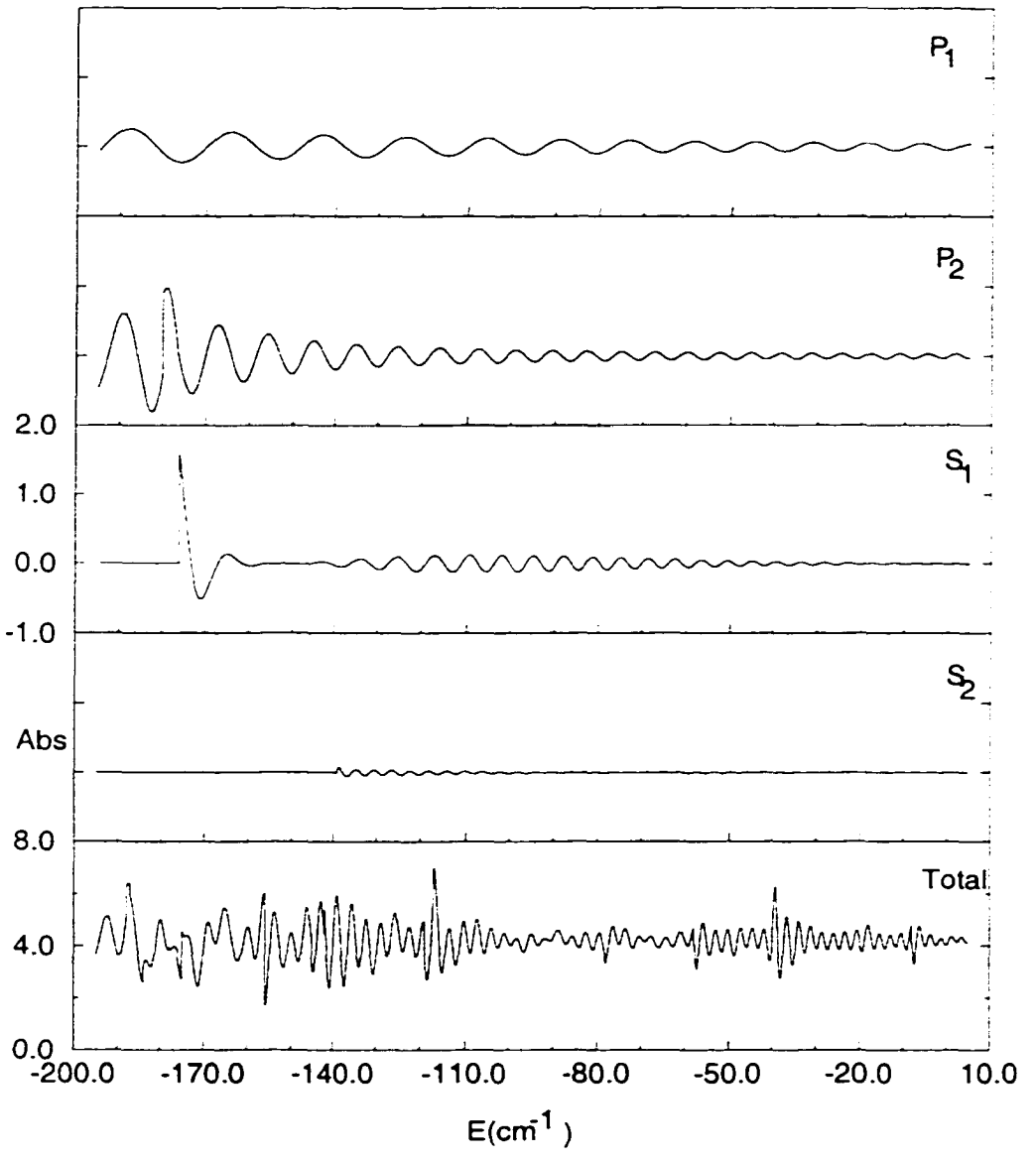

Figure 3.3: The individual absorptions produced by P_1, P_2, S_1, S_2 closed orbits and the total absorption associated with the twenty closed orbits shown in Fig. 3.2.

3.3 Comparison between the theoretical and experimental absorption spectrum with the same resolution

We can compare theory and experiment by two methods (see Fig. 3.4):

1. Compare the theoretical absorption spectrum to the measured absorption spectrum with the same resolution.

   Ideally the more closed orbits we include in the absorption spectrum calculation, the better resolution in the calculated spectrum we will get. However, searching for long closed orbits is time consuming and unrewarding. Therefore instead of trying to achieve better resolution, we convolute both measured and calculated absorption spectrum to achieve the same resolution, then make the comparison.

2. Compare the theoretical recurrence spectrum to the measured recurrence spectrum.

   The Fourier-Transform of the measured absorption spectrum is called the recurrence spectrum. The Fourier-Transform converts each oscillatory term in the absorption spectrum into a sharp peak, and the location of the peak tells the return-time of the closed orbit. Therefore the recurrence spectrum drawn with the time axis going from 0 to T_{max} provides information about the closed orbits with return-time up to T_{max}. Hence we only need to include those orbits to do the calculation. This method has been proved to be an effective way to make the comparison.

The comparison by method 1 is presented in this section, and the comparison by method 2 will be presented in the next section.

The theoretical calculation includes contributions from the 20 short closed orbits shown in Fig. 3.2, which produce the largest-wavelength oscillations. We convolute both this theoretical absorption spectrum and the measured absorption spectrum to extract the

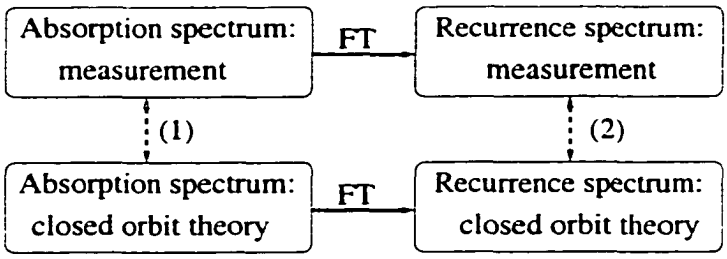

Figure 3.4: Two ways to make the comparison between theory and experiment:(1) Compare the theoretical and experimental energy spectrum directly; (2) Fourier-Transform both theoretical and experimental spectrum, then compare the theoretical and experimental recurrence spectrum.

large-scale structure.

The convoluted spectrum is defined as:

$$C_\delta(E_0) = \int_{-\infty}^{\infty} Abs(E) G_\delta(E - E_0) dE \tag{3.4}$$

where $Abs(E)$ is the signal and G_δ is a Gaussian function

$$G_\delta(E) = \frac{1}{\sqrt{2\pi\delta^2}} e^{-E^2/2\delta^2}.$$

The meaning of the integration in (3.4) is that we replace each signal at each point E by a Gaussian function, and then the value of the convoluted spectrum at E_0 is the sum of the contributions from all these Gaussian functions. The parameter δ determines the resolution of the convoluted spectrum. In Fig. 3.5, we show the theoretical convoluted spectrum (dashed line) and the experimental convoluted spectrum (solid line) both with the resolution $\delta = 2\ cm^{-1}$. To match the theoretical curve with the experimental curve, we multiply the convoluted experimental spectrum by the ratio of the average value of the theoretical absorption and the average value of the measured absorption. This method works well only if we include many closed orbits in the calculation. Mostly, the locations

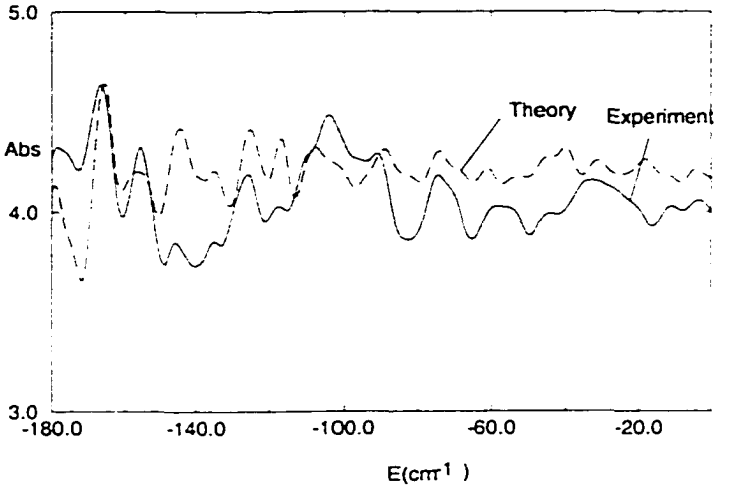

Figure 3.5: The dashed line is the theoretical absorption spectrum including 20 closed orbits and the solid line is the experimental spectrum. Both have been convoluted with $\delta = 2$ cm^{-1}. The experiment spectrum was measured by Bielefeld group in Germany.

of peaks and valleys in theory and experiment line up, but the heights are not entirely consistent.

3.4 Comparison between the theoretical and experimental recurrence spectrum

3.4.1 The conventional Fourier-Transform and its failure in the crossed field system

Closed orbit theory tells us that the large scale structure in the absorption spectrum results from the superposition of sinusoidal oscillations produced by the closed orbits. If the sinusoidal components are sine waves with constant or nearly constant wavelength and amplitude, the Fourier-Transform converts each component into a sharp peak well separated from others. The Fourier-Transform is defined as

$$\tilde{Abs}(T) = \int_{E_1}^{E_2} Abs(E)\epsilon^{-\imath TE/\hbar} dE. \tag{3.5}$$

Fig. 3.6 shows the Fourier-Transform of some ideal absorption. Recurrence spectra allow us to extract the information about the closed orbits:

- The location of the jth peak tells the return time T_j of the jth closed orbit. Since the classical action of a closed orbit is related to the return time of the closed orbit by [1]

  $$\partial S_j(E)/\partial E = T_j,$$

  the phase of the absorption is related to the return time by

  $$S_j(E) = T_j E.$$

  If the return time of the closed orbit is nearly constant as energy changes, then the Fourier-Transform converts the oscillation produced by the closed orbit into a sharp

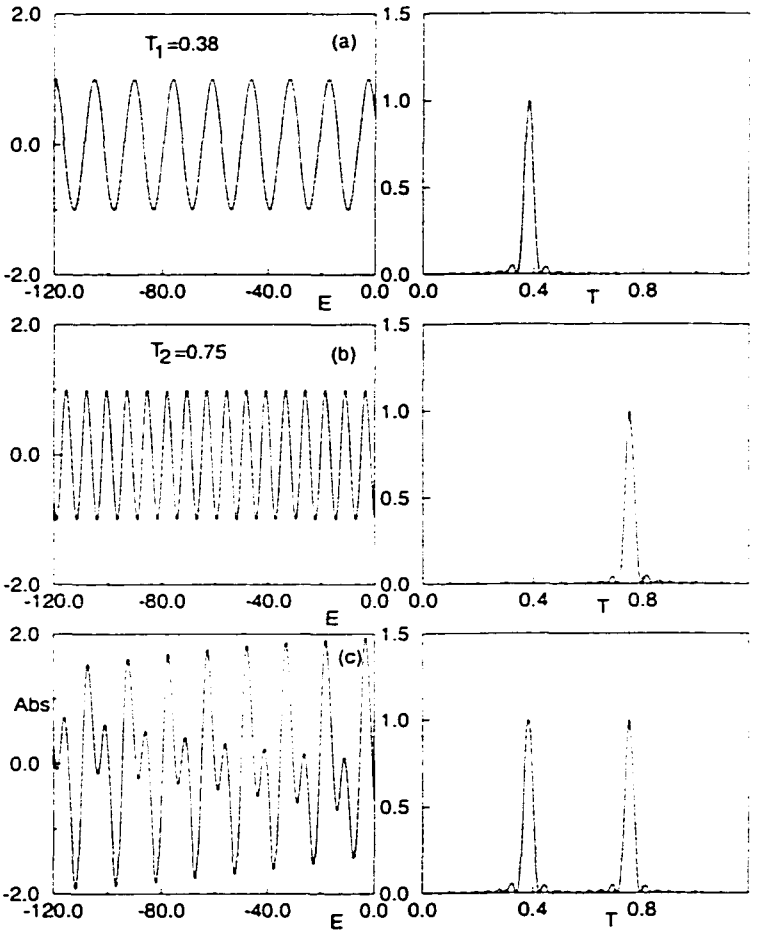

Figure 3.6: Two sine waves and their sum: (a) $sin(T_1E)$; (b) $sin(T_2E)$: (c) $sin(T_1E) + sin(T_2E)$. The absolute square of their Fourier transforms are shown on the right.

peak at $T = T_j$.

- The height of the jth peak is proportional to the classical amplitude correlated with the jth closed orbit.

This method has been successfully applied to other systems [2.4], but it fails for this data set. The waves produced by the closed orbits in the crossed field system are chirped waves whose wavelengths and amplitudes dramatically change with energy. The Fourier-Transform converts chirped waves into a mountain range of peaks (see Fig. 3.7), and we cannot extract information about the closed orbits from these mountain ranges. Therefore we need a new computational method to convert chirped waves into sharp and well-separated peaks.

3.4.2 The basic idea of the Chirped-Fourier-Transform

Considering that the waves produced by the closed orbits are chirped waves, we multiply the chirped wave by another chirped wave whose phase changes in the same way as the original wave and whose amplitude changes opposite to the original wave. Then we integrate to change the variable from energy E to time T. For example, in Fig. 3.8, the chirped wave (a) is given by

$$Abs(E) = e^{-\gamma(E-E_0)} sin[T_0(E - E_0) + \alpha(E - E_0)^2].$$

where E_0 is the center point of the energy range $E_0 = (E_1 + E_2)/2$ and T_0 is the return time of the closed orbit at $E = E_0$. We multiply it by another chirped wave (b) to do the transformation:

$$\bar{Abs}(T) = \int_{E_1}^{E_2} Abs(E) e^{\gamma(E-E_0)} e^{-i[T(E-E_0)+\alpha(E-E_0)^2]} dE,$$

where E_1 is the lower bound of the energy range and E_2 is the upper bound of the energy range. This is equivalent to first multiplying the wave (a) by

$$e^{\gamma(E-E_0)} e^{-i[\alpha(E-E_0)^2]}$$

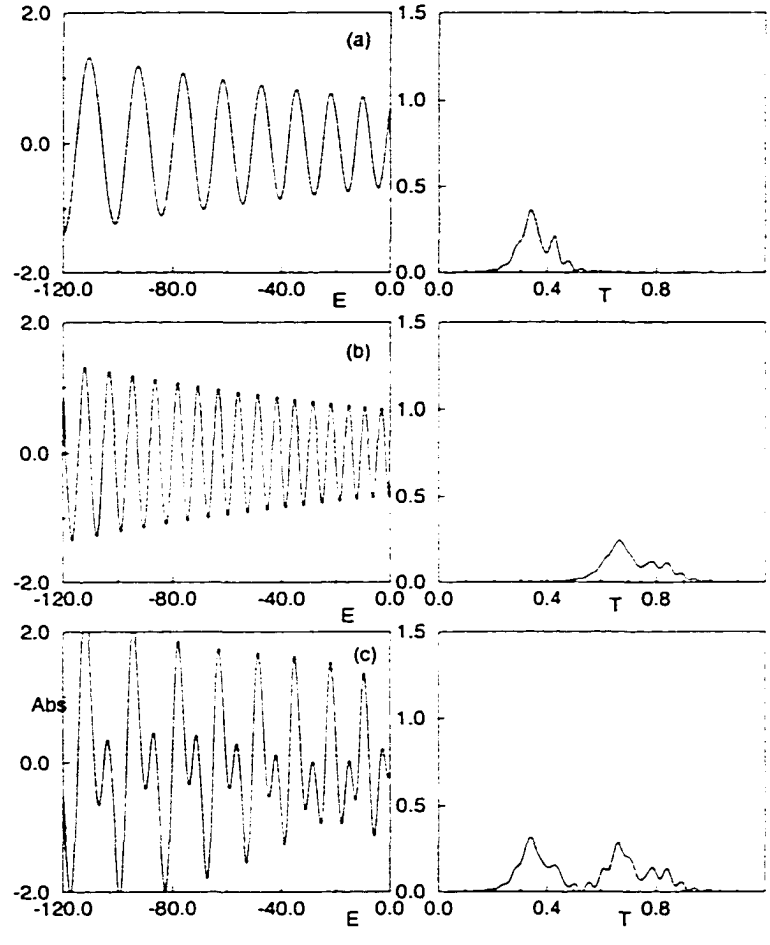

Figure 3.7: Two chirped waves and their sum: (a) $e^{-\gamma(E-E_0)}sin[T_1(E-E_0)+\alpha_1(E-E_0)^2]$: (b) $e^{-\gamma(E-E_0)}sin[T_2(E-E_0)+\alpha_2(E-E_0)^2]$; (c) the sum of (a) and (b). The absolute square of their Fourier transforms are shown on the right. $T_1 = 0.38$, $T_2 = 0.75$, $\alpha_1 = 9.4 \times 10^{-4}$, $\alpha_2 = 1.4 \times 10^{-3}$ and $\gamma = 0.006$.

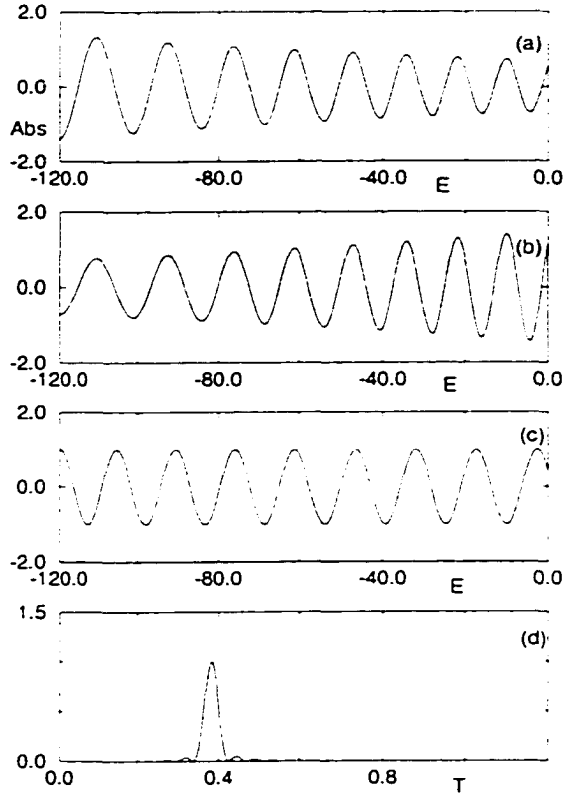

Figure 3.8: (a) A chirped wave: $exp(-\gamma(E-E_0))sin[T_0(E-E_0)+\alpha(E-E_0)^2]$; (b) the complementary chirped wave, for use in the CFT: $exp(-\gamma(E-E_0))exp[-i(T(E-E_0)+\alpha(E-E_0)^2)]$; (c) $sin(T(E-E_0)$;(d) Chirped-Fourier-Transform of (a) with $T_0 = 0.38$, $E_0 = -65$ and $\alpha = 9.4 \times 10^{-4}$.

to convert one of the exponential terms in the chirped sine wave (a) into a perfect exponential wave (c):

$$exp[iT_0(E - E_0)],$$

then multiply (c) by

$$e^{-iT(E-E_0)}$$

to do the transformation. This transformation produces a sharp peak at $T = T_0$ (see Fig. 3.8(d)). Following this idea, we develop a new computational method called the Chirped-Fourier-Transform (CFT) to extract the closed orbits from the absorption spectrum.

3.4.3 The theory of the Chirped-Fourier-Transform

Definition of Chirped-Fourier-Transform: Suppose we have a signal $A(\omega)$ which is a superposition of chirped waves:

$$A(\omega) = \sum_k exp[iS_k(\omega)]f_k(\omega)C_k \tag{3.6}$$

We define $T_k(\omega) = \partial S_k(\omega)/\partial\omega$ and call $A(\omega)$ a "frequency spectrum". In our case, ω corresponds to E, $A(\omega)$ corresponds to the absorption spectrum as a function of energy, $f_k(\omega)C_k$ corresponds to the recurrence amplitude of a classical orbit, and $S_k(\omega)$ corresponds to the action of the classical orbit.

Suppose the functions $S_k(\omega)$ and $f_k(\omega)$ are known, but the constant coefficients C_k are not known, and $T_k(\omega)$ and $T_j(\omega)$ are "well-separated" in a sense that will be defined below. Then to determine the coefficients C_k, we multiply the signal by some chosen function,

$$g(\omega)exp[-ir(\omega; p)] \tag{3.7}$$

where p is a collection of parameters. Let us define the integral

$$R(p) = \int_{\omega_1}^{\omega_2} g(\omega)exp[-ir(\omega; p)]A(\omega)de \tag{3.8}$$

With appropriate specification of $g(\omega)$ and $r(\omega;p)$, this integral is what we call the Chirped-Fourier-Transform (CFT).

Several strategies are available to specify $g(\omega)$ and $r(\omega;p)$:

Method A: Let the parameter p be a multiplicative constant, $p = a$, let $r(\omega;a) = aS_j(\omega)$. $g(\omega) = \frac{dS_j(\omega)}{d\omega}/f_j(\omega)$, and assume $f_j(\omega) \neq 0$ in the observation range, then

$$R(a) = \sum_k \int_{\omega_1}^{\omega_2} expi[aS_j(\omega) - S_k(\omega)][\frac{dS_j(\omega)/d\omega}{f_j(\omega)}]f_k(\omega)C_k d\omega$$

This is the form used by Bonmassar and Schwartz in [19]. The term with $k = j$ is

$$\begin{aligned} R_j(a) &= \int_{S_{min}}^{S_{max}} exp[i(a-1)S_j(\omega)]C_j dS_j \\ &= C_j exp[i(a-1)\overline{S}]\frac{2\sin[(a-1)(\Delta S/2)]}{a-1} \end{aligned} \tag{3.9}$$

where $\overline{S} = (S_{max} + S_{min})/2$ and $\Delta S = S_{max} - S_{min}$. Therefore

$$|R_j(a)|^2 = |C_j|^2(\pi\Delta S)\delta_{\Delta S}(\frac{a-1}{2}) \tag{3.10}$$

where

$$\delta_\eta(u) = \frac{\sin^2 \eta u}{\pi \eta u^2}$$

which is a widened delta function with the properties:

$$\begin{aligned} Lim_{\eta\to\infty}\delta_\eta(u) &= 0 \quad u \neq 0 \\ Lim_{\eta\to\infty}\delta_\eta(0) &\to \infty \\ \int_{-\infty}^{\infty} \delta_\eta(u)du &= 1 \end{aligned}$$

Therefore the term $k = j$ by itself produces a peak at $a = 1$. This is the "physically interesting" peak: we chose $r(\omega;a)$ to match the oscillations in this term. The height of this peak is proportional to $(\Delta S)^2$, while its width is proportional to $(\Delta S)^{-1}$.

The terms with $k \neq j$ give

$$R_{k\neq j} = C_k \int expi[aS_j(\omega) - S_k(\omega)] \frac{f_k(\omega)}{f_j(\omega)} dS_j(\omega)$$

We want these terms to be small. They may give significant contributions in two cases:

Case 1: For some $k = k_0$, there exists a value $a = a_0$ such that $a_0 S_j(\omega) - S_{k_0}(\omega) \approx$ const. over the whole range of integration, that is, $S_{k_0} \approx a_0 S_j(\omega) -$ const. We approximate $C_{k_0} \frac{f_{k_0}(\omega)}{f_j(\omega)} \approx$ constant $\equiv C'_{k_0}$. Then the term with $k = k_0$ is

$$R_{k_0\neq j} = C'_{k_0} e^{-i\text{const.}} \int_{S_{min}}^{S_{max}} e^{i(a-a_0)S_j(\omega)} dS_j(\omega),$$

$$|R_{k_0\neq j}|^2 = |C'_{k_0}|^2 \pi \Delta S \delta_{\Delta S}(\frac{a-a_0}{2}).$$

and we get a "physically uninteresting" peak at $a = a_0$. At least we would like the uninteresting peak to be "well-separated" from the interesting one. The condition $a_0 S_j(\omega) \approx S_{k_0}(\omega) +$ const. implies

$$a_0 = T_{k_0}(\omega)/T_j(\omega) \approx \text{constant}$$

We need a_0 to be separated from 1 by more than the width of the δ-function.

$$|a_0 - 1| = |\frac{T_{k_0}}{T_j} - 1| \gg \frac{1}{\Delta S}.$$

If this condition holds, the uninteresting peak may be large, but at least it is well-separated from the interesting one at $a = 1$.

Case 2: For some $k = k_1$, the integral has a stationary phase point, and can be evaluated by the stationary phase approximation. Typically, there exists a range of a values such that for any $a = a_1$ in this range, there exists a frequency $\omega = \omega_0$ in the domain of integration such that

$$a_1 = T_{k_1}(\omega_0)/T_j(\omega_0)$$

Then $R_{k_1\neq j}$ can be rewritten as:

$$
\begin{aligned}
R_{k_1 \neq j} &= C_{k_1} \int_{\omega_{min}}^{\omega_{max}} expi[aS_j(\omega) - S_{k_1}(\omega)] \frac{f_{k_1}(\omega)}{f_j(\omega)} T_j(\omega) d\epsilon \\
&\approx C_{k_1} \frac{f_{k_1}(\omega_0)}{f_j(\omega_0)} expi[a_1 S_j(\omega_0) - S_{k_1}(\omega_0)] T_j(\omega_0) \\
&\quad \cdot \int_{\omega_{min}}^{\omega_{max}} expi[\frac{a_1 T_j(\omega_0)' - T_{k_1}(\omega_0)'}{2} (\omega - \omega_0)^2] d\epsilon \\
&\approx C'_{k_1} expi[a_1 S_j(\omega_0) - S_{k_1}(\omega_0)] T_j(\omega_0) \\
&\quad \cdot \frac{2\pi}{|a_1 T_j(\omega_0)' - T_{k_1}(\omega_0)'|^{1/2}} \\
&\quad \cdot exp(i\frac{\pi}{4} sgn(a_1 T_j(\omega_0)' - T_{k_1}(\omega_0)')
\end{aligned}
$$

where $C'_{k_1} = C_{k_1} \frac{f_{k_1}(\omega_0)}{f_j(\omega_0)}$. Again, we get a "physically uninteresting" peak, now at $a = a_1$. The height of the peak is:

$$
|R_{k_1}(a = a_1)|^2 = |C'_{k_1} T_j(\omega_0) \frac{2\pi}{|a_1 T_j(\omega_0)' - T_{k_1}(\omega_0)'|^{1/2}}|^2.
$$

Such peaks might be substantial, but typically they will not be as large as those that occur in case 1. In case 1, the phase of the exponential is practically constant over the whole range of the integration, while in case 2, there is only an isolated stationary-phase point in the range of integration; therefore case 2 gives peaks having heights independent of the range of integration ΔS.

Of course, such uninteresting peaks are troublesome only if they occur too near to $a = 1$.

We use the word "aliasing" to mean the presence of "false" (i.e. physically uninteresting) peaks in $|R(a)|^2$ overlapping with the interesting peak at $a = 1$. It is clear that the Chirped-Fourier-Transform can give significant aliasing. For the system we are studying in this thesis, we found that a different method gives better results.

Method B: By change of origin, let $\omega_a = -\omega_b$. Choose $g(\omega) = 1/f_j(\omega)$, let p

represent the set of three parameters (t, α, β), and let $r(\omega, p) = t\omega + \alpha\omega^2 + \beta\omega^3$: then

$$R(t;\alpha,\beta) = \sum_k \int_{\omega_a}^{\omega_b} expi[S_k(\omega) - (t\omega + \alpha\omega^2 + \beta\omega^3)] \; g(\omega) f_k(\omega) C_k d\omega \tag{3.11}$$

Let's focus on the term $k = j$. We expand $S_j(\omega)$ in a power series

$$S_j(\omega) = S_j^0 + T_j\omega + \alpha_j\omega^2 + \beta_j\omega^3 + q_j(\omega)$$

where $q_j(\omega)$ is equal to the remainder of Taylor series, i.e. it is the difference between the 3-jet (terms up to 3rd order) and the exact $S_j(\omega)$. We presume $q_j(\omega)$ is small. Then the term with $k = j$ is

$$\begin{aligned} R_j(t;\alpha_j,\beta_j) &= C_j e^{iS_j^0} \int_{\omega_a}^{\omega_b} e^{i(T_j - t)\omega} d\omega \\ &= C_j e^{iS_j^0} e^{i(T_j - t)\overline{\omega}} \frac{\sin(\frac{T_j - t}{2})\Delta\omega}{\frac{T_j - t}{2}}, \end{aligned}$$

$$|R_j(t;\alpha_j,\beta_j)|^2 = C_j^2 \pi \Delta\omega \delta_{\Delta\omega}((T_j - t)/2) \tag{3.12}$$

where $\overline{\omega} = (\omega_b + \omega_a)/2$ and $\Delta\omega = \omega_b - \omega_a$. As before, we get a widened delta-function, now centered at $t = T_j$. We call $R(t;\alpha,\beta)$ the (α,β)-chirped time-spectrum of the signal.

To look at aliasing, we examine a term with $k \neq j$. Any term with $k \neq j$ is

$$\begin{aligned} & R_{k\neq j}(t;\alpha_j,\beta_j) \\ = \; & C_k e^{iS_k^0} \int e^{i(T_k - t)\omega + (\alpha_k - \alpha_j)\omega^2 + (\beta_j - \beta_k)\omega^3 + q_j(\omega)} \frac{f_k(\omega)}{f_j(\omega)} d\omega. \end{aligned}$$

It has a stationary point when

$$(T_k - t) + 2(\alpha_k - \alpha_j)\omega + 3(\beta_j - \beta_k)\omega^2 = 0.$$

For example, when $t = T_k$, there is a stationary phase point at $\omega = 0$. Suppose the cubic term is negligible and again $C_k f_k(\omega)/f_j(\omega) \approx const. = C_k'$; then the integral can be

estimated as

$$|R_{k\neq j}|^2 = |C'_k \int_{\omega_1}^{\omega_2} e^{i(\alpha_k-\alpha_j)\omega^2} d\omega|^2$$
$$= |C'_k|^2 \frac{\pi}{|\alpha_k - \alpha_j|}$$

The height of the main peak increases in proportion to $(\Delta\omega)^2$, but this peak does not. If α_k and α_j are well separated and $|C_k/C_j| \sim O(1)$, then the "false" peaks are smaller than the "real" peak.

For the two examples we give in this paper, this method B works better than method A. The reason is the following. It is a property of the orbits in our systems that if $T_k \sim aT_j$, then $\alpha_k \sim a\alpha_j$, $\beta_k \sim a\beta_j$; therefore $S_k - aS_j \sim$ constant over the observed range. If we use Method A, case 1 frequently occurs (phase is constant over the whole range) and the "false" peaks are as large as the physically interesting one. In contrast, when we use Method B, the undesired integrals have only isolated stationary-phase points, and the "false" peaks are usually smaller than the physically interesting peak.

We use Method B in all of the calculations reported in this section. For certain orbits we include an additional parameter γ, with $g(\omega) = exp(-\gamma\omega)$. There are three methods to determine the parameters (α, β, γ).

Method 1: Experimental method

Suppose we are analyzing experimental data without prior knowledge of the parameters (α, β, γ) of an orbit. Then we would search in the parameter space to maximize the height of a peak at $t = T_j$ in the CFT. We first set β, γ to zero, and gradually adjust α to make the peak at $t = T_j$ as high and narrow as possible. After we reach the optimal α, we then turn on β, and finally turn on γ. That would give an experimental determination of $(\alpha_j, \beta_j, \gamma_j)$.

Method 2: Taylor expansion

Suppose by some means such as theoretical calculations we know the values of T_j, $dT_j/d\omega, d^2T_j/d\omega^2$ at some particular ω_0 within the integration range. Then we may set:

$\alpha = \frac{1}{2}dT_j/d\omega$ and $\beta = \frac{1}{6}d^2T_j/d\omega^2$.

Method 3: Nonlinear Least-Squares fit

Suppose we have determined theoretically the quantity $S_j(\omega)$ over the whole measured range of ω. Then we can choose (α, β) by a nonlinear least-squares fit over the range.

It should be evident that the more a priori information we have about $(T_j, \alpha_j, \beta_j, \gamma_j)$, the better the result will be: the physically-interesting peaks will be higher and narrower. Obviously one can go to higher-order terms in a Taylor series, or even fit $S_j(\omega)$ to some other kind of function. In our calculations, a third-degree expansion is sufficient.

3.4.4 The application of the Chirped-Fourier-Transform to the crossed field system

In this section, we use method B to extract the closed orbits of the crossed field system from the measured absorption spectrum. According to closed orbit theory, the oscillations in the absorption spectrum are given by:

$$Df_{osc}(E) = \sum_j C_j(E) sin(S_j(E)/\hbar - \pi\mu_j/2). \tag{3.13}$$

Here j labels the closed orbits and their repetitions. $S_j(E)$ is the classical action of the j^{th} closed orbit, which satisfies

$$\partial S_j(E)/\partial E = T_j(E) \tag{3.14}$$

where $T_j(E)$ is the return-time of that orbit.

In Fig. 3.3, we show the contribution of the shortest closed orbits to the absorption spectrum, as calculated from theory [Eq. (3.1)]. As a function of energy, $C_1(E)$ gradually decreases while $S_1(E)$ increases nonlinearly, so we get a chirped sine-wave. We represent

the return-time of each closed orbit as a Taylor expansion in energy,

$$T_j(E) = T_j(E_0) + 2\alpha_j(E - E_0) + 3\beta_j(E - E_0)^2 \tag{3.15}$$

and approximate the amplitude $C_j(E)$ by an exponential function.

$$C_j(E) = C_j(E_0)exp[-\gamma_j(E - E_0)/\hbar]. \tag{3.16}$$

The corresponding Chirped-Fourier-Transform (CFT) is defined as: [19]

$$\begin{aligned} &\widetilde{Df}(T;\alpha,\beta;\gamma) \\ &= \int_{E_1}^{E_2} Df(E)e^{-i[T(E-E_0)+\alpha(E-E_0)^2+\beta(E-E_0)^3]/\hbar+\gamma(E-E_0)/\hbar}dE \end{aligned} \tag{3.17}$$

where E_0 is some point in the middle of the observed range.

Fig. 3.10 displays the Chirped-Fourier-Transform of the energy spectrum as a function of T with various selected values of α, β and γ. The dashed lines indicate the return times of the three short closed orbits in Fig. 3.9, as determined from trajectory calculations. In Fig. 3.10, the bottom graph (a) is the ordinary Fourier transform, with α, β, γ all set to zero. We see hardly any relationship between the measurements and the known closed orbits. Following the leftmost dashed line up from the bottom, we gradually increase α until we reach $\alpha_1 = 6 \times 10^{-4}$, (curve d) and we see that a peak appears there. Further increase of α would disperse this peak again. Next we turn on β; at first it weakens the peak, until we get near the correct value (curve f), where the peak is strengthened. Finally, turning on γ (curves g and h), the CFT gives a sharp peak at the right location, labeled "1".

For the second and third closed orbits, we find that the amplitudes do not change much with energy, so we vary only α and β. Again the optimal values of these parameters give clear well-resolved peaks in the correct locations (labeled "2" and "3"). Now the sharp peak in the Chirped-Fourier-Transform recurrence spectra tells us several pieces of information about the closed orbit:

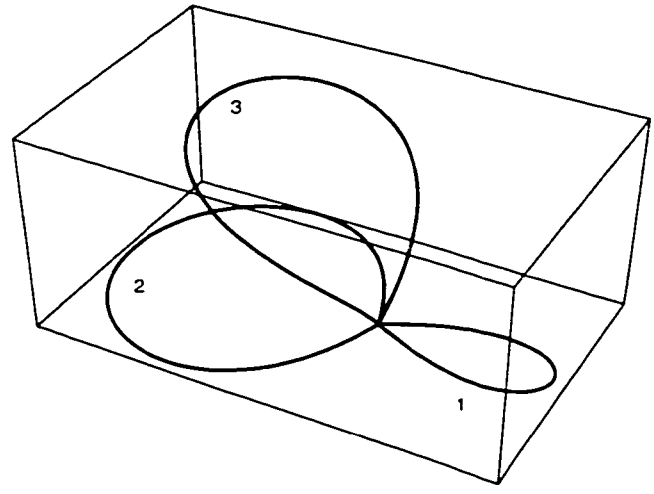

Figure 3.9: Three shortest closed orbits identified in Fig. 3.10 for $B = 6T, F = 1KV/cm$.

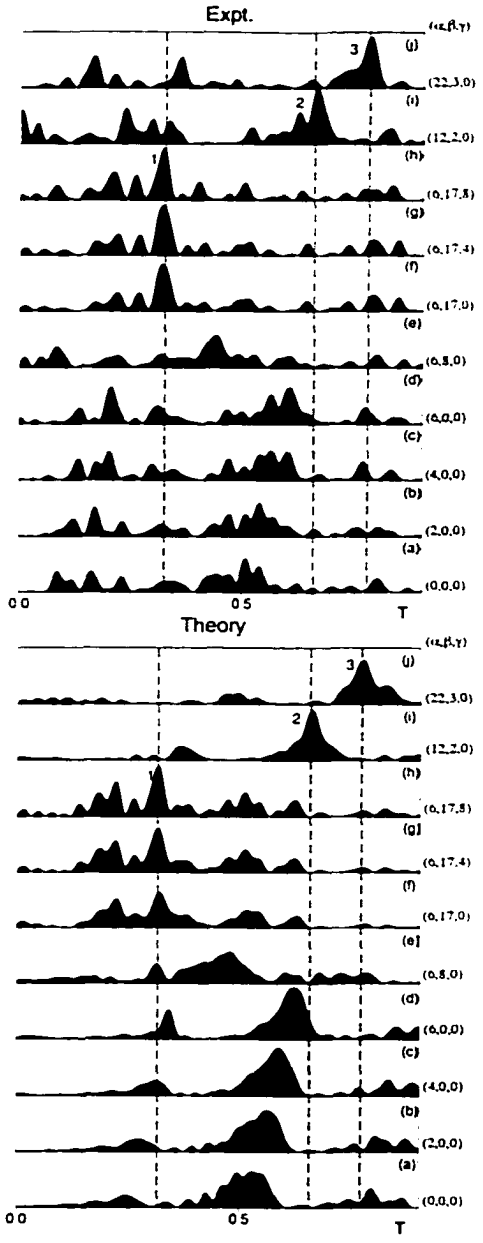

Figure 3.10: Measured and calculated recurrence spectra for $B = 6T, F = 1KV/cm$. Time is measured in units of the cyclotron time at $6.002T$ (5.95×10^{-12} sec.). The dashed lines represent the return-times of the first three closed orbits. α, β, γ are the coefficients in the Chirped-Fourier-Transformation and they are in units $1/cm^{-1}$, $cyclotron times/cm^{-1}$, $cyclotron times/cm^{-2}$. α, β, γ should be multiplied by $10^{-4}, 10^{-6}, 10^{-3}$ respectively: thus for example the calculated and observed value of α_1 is 6×10^{-4}.

- The location tells us the return time of the closed orbit at $E = E_0$ which is the middle point of the integration energy range.
- The height of the peak tells us the classical amplitude associated with the closed orbit at $E = E_0$.
- The optimal α and β tell the first derivative and second derivative of the return time of the closed orbit with respect to the energy respectively, and the optimal γ tells the decay rate of the classical amplitude of the closed orbit as the energy increases.

We use three methods introduced above to determine the parameters (α, β, γ) and list the values of T, α, β, γ for five of the shortest orbits in the crossed-field problem in Table 3.1. T is in cyclotron time and is the return−time of the closed orbits at $E = -95cm^{-1}$. α, β, γ are in the units of cyclotron times$/cm^{-1}$, cyclotron times$/cm^{-2}$ and $/cm^{-1}$ respectively. It is evident that these methods all give consistent results.

The experimental and theoretical results agree well with each other. This consistency confirms the validity and applicability of the appropriate closed-orbit formula for this system. More important, we can say that the observations give measured values of α, β to within uncertainties less than $\pm 1\%, \pm 5\%$. In many potential applications of closed-orbit or periodic-orbit theory, the scaled-variable method will be impossible to use. The chirped Fourier transform gives a new way to extract classical information from a quantum spectrum without using scaling laws [20]. In Appendix A, we show another application of CFT.

Table 3.1: The (α, β, γ) values of five closed orbits

orbit	parameters	Taylor	NLLS	Expt.
1	$\alpha(\times 10^{-2})$	0.06	0.07	0.07
	$\beta(\times 10^{-6})$	17.0	20.0	20.0
	$\gamma(\times 10^{-2})$	0.80	0.80	0.80
	T	0.34	0.34	0.34
2	$\alpha(\times 10^{-2})$	0.12	0.12	0.12
	$\beta(\times 10^{-6})$	1.88	1.95	2.00
	T	0.68	0.68	0.68
3	$\alpha(\times 10^{-2})$	0.22	0.22	0.22
	$\beta(\times 10^{-6})$	3.40	3.55	3.33
	T	0.80	0.80	0.80
4	$\alpha(\times 10^{-2})$	0.30	0.30	0.30
	$\beta(\times 10^{-6})$	3.13	3.03	3.20
	T	1.82	1.82	1.82
5	$\alpha(\times 10^{-2})$	0.17	0.17	0.17
	$\beta(\times 10^{-6})$	2.82	2.87	3.33
	T	1.96	1.96	1.96

Chapter 4

The continuum absorption

We call the lower envelope of the absorption spectrum the "continuum absorption". From Fig. 4.2, we observe that the continuum absorption stays nearly zero at low energies and starts to rise near the energy $E \approx -140cm^{-1}$. This energy defines the continuum "threshold". As the energy increases, the continuum increases and finally flattens out at high energies. In this chapter, we first give a qualitative interpretation of the continuum threshold, then present a quantitative model for the calculation of the continuum intensity.

4.1 The continuum threshold

Let us review the correlation between the prompt signal in Fig. 4.1 and the continuum in Fig. 4.2. Near b, where the prompt signal becomes significant, the continuum in the total absorption spectrum starts to set in. This region gives a fuzzy threshold for continuum absorption marked by a heavy arrow in Fig. 4.2. Near c, where more and more signals enter the prompt signal channel, the intensity of the continuum increases. As the energy approaches the region d where almost all the signals become prompt, almost all the quasidiscrete states disappear into the continuum. This correlation indicates that the

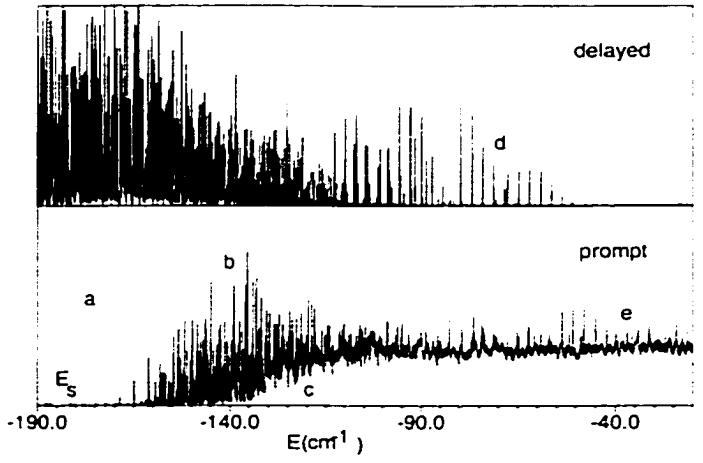

Figure 4.1: The measured prompt and delayed absorption spectrum at $B = 6.002T$, $F = 1000V/cm$. The dotted line marked E_s is the energy of the saddle point ($-193cm^{-1}$).

continuum is correlated with short lived states, or with classical trajectories that escape after a short time.

Consider the threshold of continuum absorption in a simpler system - a hydrogen atom in a purely electric field ($B = 0$). The electric field points to the positive x direction and pulls the electron in the direction opposite to the field, so we call the electric field direction ($+x$) the "uphill" direction and the opposite direction $-x$ the "downhill direction". The potential energy of the system is $V = \frac{1}{r} + Fx$. This potential energy has a local maximum $V_{max} = -2F^{1/2}$ at $x_s = -1/\sqrt{F}$. We call $E_s = V_{max}$ the saddle energy and x_s the saddle point. For energies below E_s, the classical trajectories are bound forever; for energies between E_s and zero, some of the trajectories are bound and some of them may pass over the saddle point and become free. The free motion represents ionization, so the saddle energy gives a threshold of classical ionization. In [22], it is observed that the threshold of continuum absorption in a pure electric field is the saddle energy. Hence the continuum threshold corresponds to the ionization threshold.

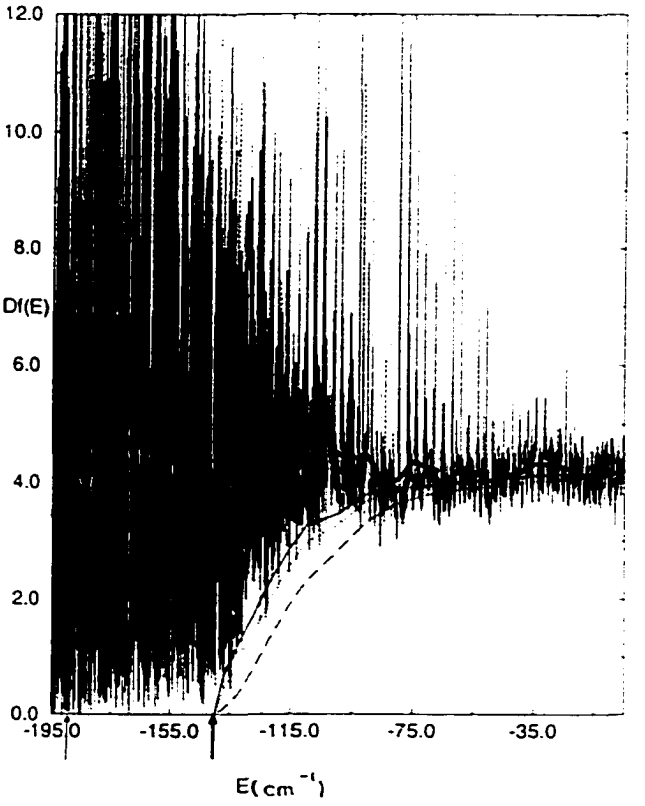

Figure 4.2: The measured total absorption spectrum at $B = 6.002T$, $F = 1000V/cm$. The wiggly line is a convolution of the measurement; its fluctuations are correlated with closed orbits. The other curves are calculations based on a model for continuum absorption, discussed in chapter 4. From lowest to highest, they have $T_{crit} = 15, 20$ and $25T_c$(respectively long-dashed line, dotted line and solid line). Light arrow: saddle energy E_s $(-193cm^{-1})$. Heavy arrow: vicinity of fuzzy threshold for continuum absorption $[-140, -135]cm^{-1}$.

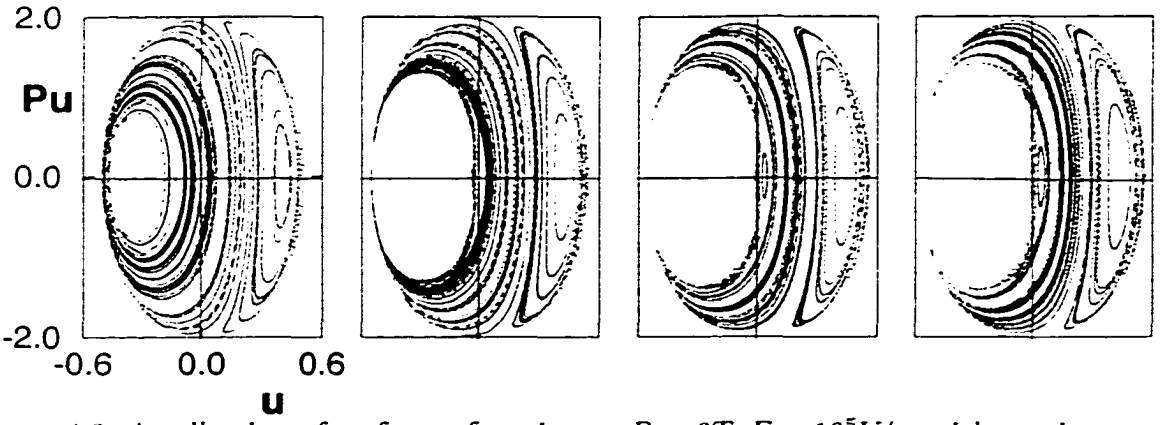

Figure 4.3: A collection of surfaces of section at $B = 6T, F = 10^5 V/m$ with varying energy. From left to right, $E = -193cm^{-1}$ (saddle energy), $-150cm^{-1}$, $-140cm^{-1}$, and $-135cm^{-1}$. $[-140, -135]cm^{-1}$ is the range for ionization threshold.

Now let us consider the boundary of the continuum in the crossed fields. In Fig. 4.2, we put a heavy arrow at $E \approx (-140, -135)cm^{-1}$ to indicate a reasonable location of this fuzzy boundary. This boundary is substantially higher than the saddle point energy $(-193cm^{-1})$, so we may say that the magnetic field stabilizes the classical motion. When the energy lies between the saddle energy and the boundary of the continuum, the trajectories which would escape in a pure electric field may turn around and stay bound in crossed fields. We get an interpretation of the continuum threshold by looking at motions in the plane perpendicular to the magnetic field. Fig. 4.3 shows some surface of section (SOS) calculations [23]. We use semiparabolic coordinates (u, v) in the plane perpendicular to B as we defined in chapter 2: $u = (r + x)^{1/2}, v = (r - x)^{1/2}$. The u-axis coincides with the positive x-axis (uphill) and the v-axis coincides with the negative x-axis (downhill). To obtain the surface of section we plot (p_u, u) when $v = 0, v' > 0$. So the p_u axis in this figure corresponds to the location of the nucleus (the origin of coordinates), and $p_u = 0$ means that all the energy is "in the v direction", i.e. downhill.

These calculations show a regular region on the right, where the trajectories are

bound forever, and a chaotic zone on the left, where electrons stay for a while before escaping, as well as a "white hole" on the left, where electrons escape rapidly. We find that the chaotic and escape zones increase rapidly in size as the energy is increased above the saddle energy. However, electrons that start from the nucleus($u = 0$) remain on regular, bound orbits until the chaotic zone touches the momentum axis. With further increase of energy, an increasing portion of the momentum axis lies within those zones, which means that electrons starting from the nucleus in a range of directions escape. The observed boundary of the continuum is the energy at which the chaotic zone first touches the momentum axis, which means that the trajectories launched at the origin may go to infinity within a short time. Thus we are seeing a threshold for chaotic ionization at the origin.

Measurements and calculations at other electric fields also support this interpretation: the observed fuzzy threshold of the continuum corresponds to the energy at which the chaotic zone begins to touch the momentum axis, i.e. the energy at which some of the electrons launched from the origin go into the chaotic zone and escape. This energy is significantly higher than the saddle energy.

4.2 The continuum intensity

Paper [22] proves that the intensity of continuum absorption is proportional to the flux of outgoing electrons that escape directly:

$$Df_{cont.}(E) = 4(E - E_i)\int_{escape} |Y(\theta,\phi)|^2 \sin\theta d\theta d\phi \qquad (4.1)$$

where $|Y(\theta,\phi)|^2$ is the angular distribution of outgoing waves, and the integral is carried out over the escaping sector.

According to [22], there is a sharp boundary between bound and escaping orbits for a pure electric field system. The sharp boundary is defined by a critical angle θ_c =

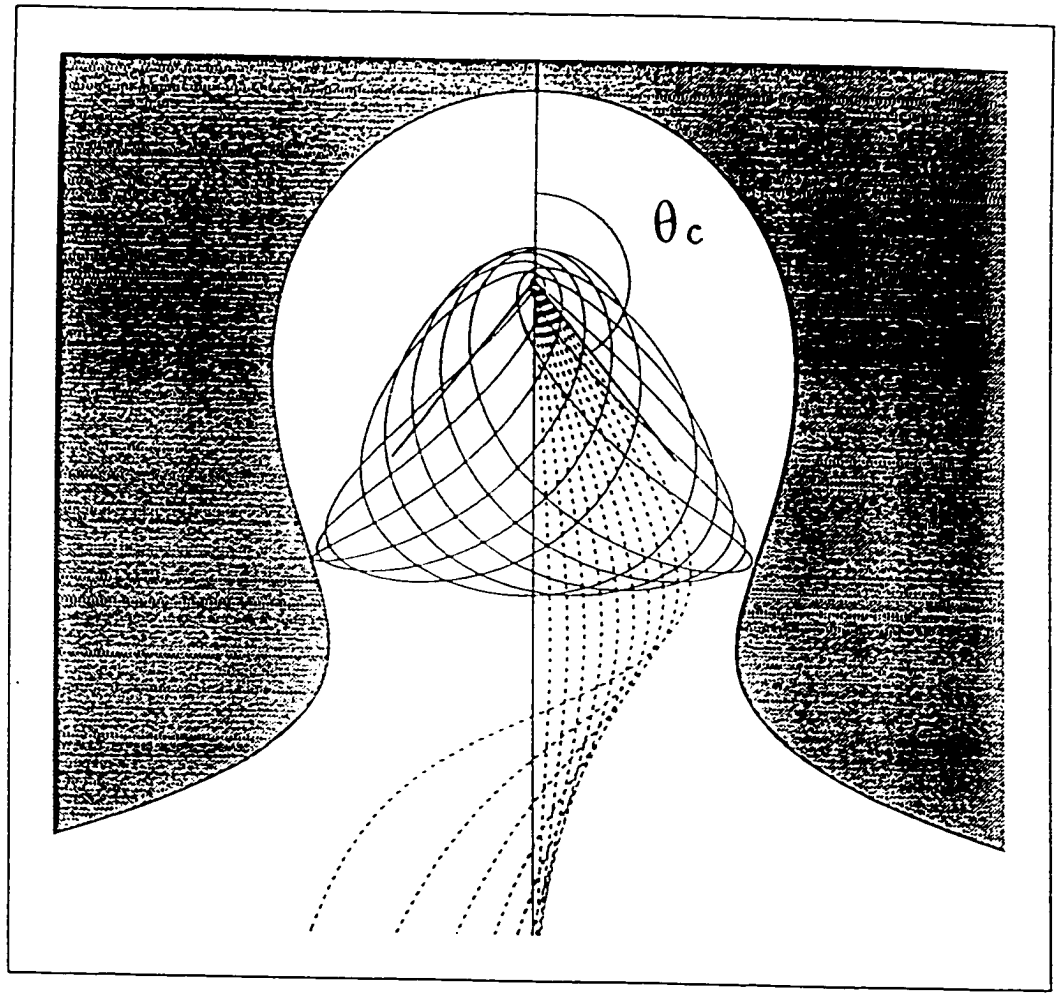

Figure 4.4: The boundary between bound and free motions in the electric field only.

$arccos(1 - E^2/2F)$ (see Fig. 4.4 from [22]). As energy increases from E_s to 0, this critical angle moves from the downhill to the uphill direction until no stable bound motion is left. The sector with ejection angle from θ_c to π is called the escape sector and the sector with ejection angle from 0 to θ_c is called the bound sector. Electrons ejected in the bound sector are bound forever, while electrons ejected in the escape sector pass over the saddle, then escape. Therefore the integration in (4.1) is an integral with θ from θ_c to π and ϕ from 0 to 2π.

After we turn on the magnetic field, the boundary between bound and free motions becomes fuzzy. In Fig. 4.5, we show the escape time of an electron as a function of its angle from the downhill direction. We observe a bound sector with angle ϕ from 120° to 180° and a quick escape sector with ϕ from 0 to 60°. Between the bound and escape sector, there is a mixture sector of the bound and escape motions with ϕ from 60° to 120°. The structure in the mixture sector is complicated and grows ever more complicated when calculations are carried out to higher resolution. We seem to be seeing here some sort of fractal boundary between bound and free motions.

This mixture of bound and free motions forces us to calculate the integral (4.1) by computing the escape time at discrete values of θ_i and ϕ_i. At each (θ_i, ϕ_i), if the escape time is less than some chosen T_{crit}, we include the increment $|Y(\theta_i, \phi_i)|^2 \sin\theta_i \Delta\theta_i \Delta\phi_i$ in the integral; otherwise that increment is excluded. Therefore, the implementation of the calculation requires an appropriate choice of T_{crit}, a clear definition of the lifetime and a scheme to calculate the lifetime of the trajectories. We address all of these points in this section.

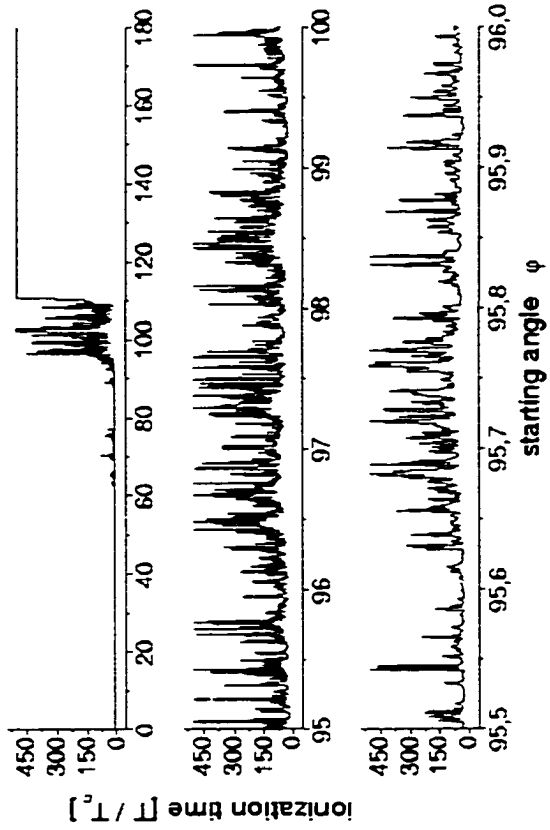

Figure 4.5: The ionization times of the electrons which move in the plane perpendicular to the magnetic field show multifractal structure in the range $\phi = 95^0 - 110^0$.

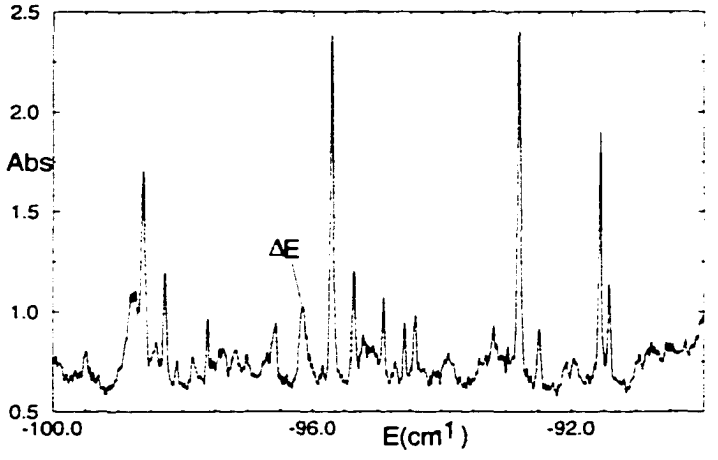

Figure 4.6: The measured absorption spectrum over the small energy range is shown to identify the maximum width of the quasidiscrete states: $\Delta E \approx 0.25 cm^{-1}$.

4.2.1 Estimation of the critical time T_{crit}

We estimate T_{crit} by examining the spectrum at high resolution, and interpreting the spectrum as quasidiscrete lines superposed on continuum absorption. We ask ourselves, what is the broadest structure that we might interpret as a "quasidiscrete" line? Examing Fig. 4.6, we would not claim that this question has a unique, unambiguous answer, but we will propose an answer and examine its consequences. We suggest that most of the broad quasidiscrete structures in Fig. 4.6 have widths comparable to that of the marked peak whose full-width-at-half-max is about 0.25 cm^{-1}. If we translate this into a lifetime according to the relation $T = 2\pi h/\Delta E$, we get a time of about $1.3 \times 10^{-10} sec$, or about 22 cyclotron times at $B = 6T$. Therefore, we did our calculations with several values of T_{crit} between 15 and 30 cyclotron times.

4.2.2 Definition of the lifetime of a trajectory

As we mentioned before, with the electric field only, the potential energy of the system has a local maximum called saddle energy $E_s = -2\sqrt{F}$ at $x_s = -1/\sqrt{F}$. When the magnetic field is included, we find that an orbit can go past the saddle point and return. However, numerical experiments show that in crossed fields, if a trajectory goes past $2x_s$, it does not return to the atom [9]. Therefore, we define the lifetime as the time taken for the trajectory to go from the origin to $x = 2x_s$.

4.2.3 Calculation of the lifetimes of the trajectories

We sample the trajectories with uniform probability for any equal solid angle or any equal area on a sphere centered at the origin with radius R. Fig. 4.5 tells that there is no clear cut boundary between the bound and free motions. However there is a clear boundary between the bound and mixed sectors. Trajectories launched in the bound sector are bound at least for very long times. We set their lifetimes as infinity without calculation. Trajectories launched in the mixed sector can be bound or free. The free motions in both the mixed and the free sectors escape at various times that depend on their initial directions. Therefore, we calculate the trajectories in these two sectors to determine their lifetimes.

- The boundary between bound and mixed sectors

  In a pure electric field, bound and free motions are well separated. Calculations show that when we turn on the magnetic field, the bound motions still stay bound for a long time, and some of the free motions are stabilized by the magnetic field. Therefore, part of the escape sector in the electric field is turned into the mixed sector. Therefore, we may safely take the boundary between bound and escape sectors in the pure electric field to be a boundary between bound and mixed sectors in crossed fields.

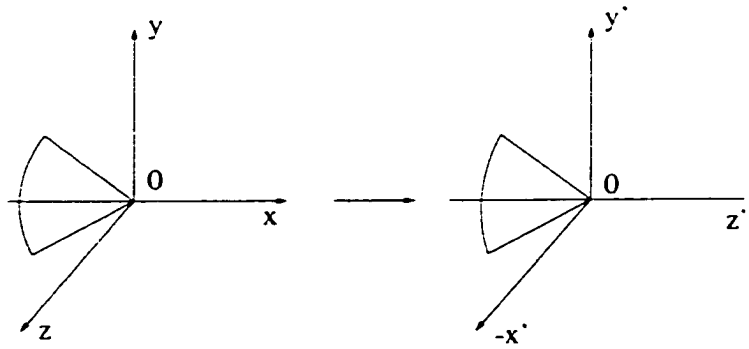

Figure 4.7: The transformation from (x, y, z) to (x', y', z') by rotating xz 90^0 counterclockwise about the y axis.

We already stated (below Eq. (4.1)) that in the pure electric field, the boundary between bound and free motions is given by a critical angle

$$\theta_c = cos^{-1}(1 - E^2/2F).$$

We prove this in appendix 4.A. Trajectories launched outside of this cone have long lifetimes, and we set their lifetimes as "infinity".

- Calculation of the lifetimes of the trajectories launched at the origin

  The trajectories launched outside of the cone in Fig. C.2 are bound and we set their lifetimes as infinity. The lifetimes of the trajectories launched inside the cone are varying and need to be calculated.

  We first rotate the space (x, y, z) 90^0 about the y axis to obtain the new coordinate space (x', y', z') (see Fig. 4.7).

  Then the momenta in (x, y, z) space are related to the momenta in (x', y', z') space by:

$$P'_x = -P_z,$$

$$P'_y = P_y,$$

$$P'_z = P_x,$$

Therefore, we can find the ejection angles (θ, ϕ) for a trajectory in (x, y, z) space from the ejection angles (θ', ϕ') in (x', y', z') space.

In (x', y', z'), the cone is symmetric about the z' axis and is defined as $\theta' \in [\theta'_{min}, \pi]$ with $\theta'_{min} = 2arcsin(-E/2\sqrt{F})$ and $\phi' \in [0, 2\pi]$ where (θ', ϕ') are the polar angle and azimuthal angle in (x', y', z') space. We sample the angles (θ', ϕ') such that the trajectories go out with uniform probability for any equal solid angle or any equal area on a sphere centered at the origin with radius R.

The area centered at z' axis or $\theta' = 0$ with increment $\Delta\theta'$ and $\phi' \in [0, 2\pi]$ is approximately $\pi(R\Delta\theta')^2$. We launch one trajectory in this area. Then in an area at θ' with increment $\Delta\theta'$ and $\phi' \in [0, 2\pi]$, the number of the trajectories launched is :

$$N(\theta') = 2\pi R^2 sin\theta' \Delta\theta' / \pi R^2 \Delta\theta'^2 = 2sin\theta' / \Delta\theta'.$$

We start θ' from $\theta' = \theta'_{min}$ and increment it with $\Delta\theta' = 1^0$. Then randomly pick an initial ϕ', and then increment ϕ' uniformly from 0 to 2π, with $N(\theta')$ points covering the interval. Then we determine the (θ, ϕ) in (x, y, z) from (θ', ϕ'). After that we calculate the lifetime T of the trajectory launched at (θ, ϕ) and record $(\pi - \theta, \phi, T)$. The result is shown in Fig. 4.8. Each point $((\pi - \theta)cos\phi, (\pi - \theta)sin\phi)$ stands for a trajectory launched along (θ, ϕ) at the origin. The color indicates the lifetime T of the trajectory: $T \leq 15T_c$ (black); $T \leq 20T_c$ (green); $T \leq 25T_c$ (red); $T \leq 50T_c$ (yellow); $T \leq 100T_c$ (blue); $T > 100T_c$ (brown) where T_c is the cyclotron time.

The symmetry we see in this graph results from the z reflection symmetry of the crossed field system. The mixing of different colors shows the complex boundary between bound and free motions.

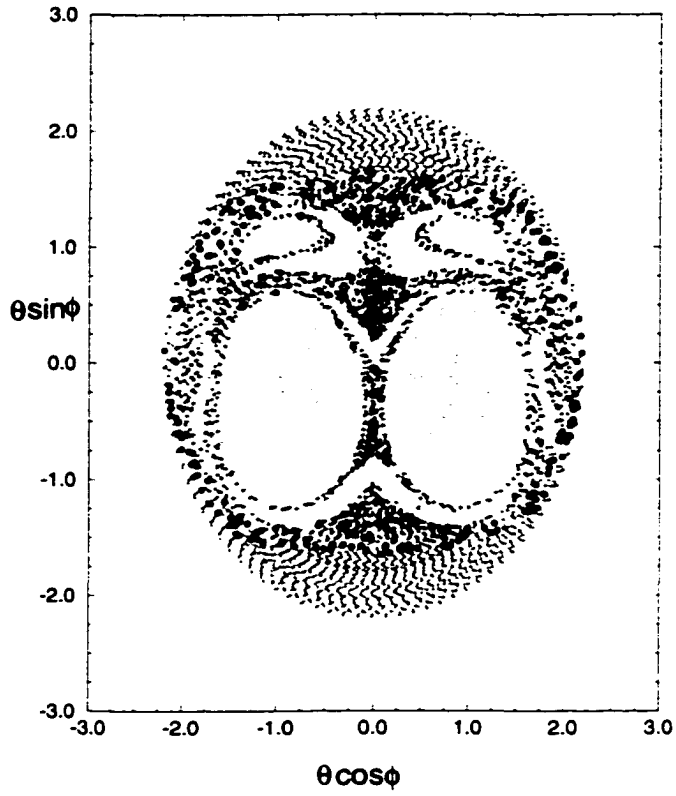

Figure 4.8: The lifetime of the trajectories in the cone defined by the rough escaping region at $E = -110cm^{-1}$, $B = 6T$ and $F = 1000V/cm$. Each point $((\pi - \theta)cos\phi, (\pi - \theta)sin\phi)$ stands for a trajectory launched along (θ, ϕ) at the origin. The color indicates the lifetime T of the trajectory: $T \leq 15T_c$ (black); $T \leq 20T_c$ (green); $T \leq 25T_c$ (red); $T \leq 50T_c$ (yellow); $T \leq 100T_c$ (blue); $T > 100T_c$ (brown).

4.2.4 Calculation of the continuum absorption

We replace the integral (4.1) by a discrete sum to calculate the continuum. Each point in Fig. 4.8 with lifetime $T < T_{crit}$ contributes one term in the summation:

$$Df_{cont.}(E) = \frac{4(E - E_i)}{\hbar^2} \sum_{T<T_{crit}} |Y(\theta'_j, \phi'_k)|^2 \sin\theta' \Delta\theta'_j \Delta\phi'_k \tag{4.2}$$

with $\Delta\theta'_j = 1^0$ and $\Delta\phi_k = 2\pi/N_{\theta'_j} = \pi/sin\theta'_j$.

To compare with the measured spectrum, we normalize the measured spectrum such that its average corresponds to

$$\begin{aligned} Df_0 &= 4(E - E_i) \int |Y(\theta, \phi)|^2 sin\theta d\theta d\phi \\ &\simeq 4(E - E_i) \sum_{j,k} |Y(\theta_j, \phi_k)|^2 sin\theta_j d\theta_j d\phi_k \end{aligned}$$

Fig. 4.2 shows our normalized calculated continuum absorption for three selected values of T_{crit} $(15, 20, 25T_c)$, together with the measured total absorption spectrum. It is clear from the figure that continuum-absorption in this system can be interpreted as the flux of electrons that escape within 20 - 25 cyclotron times.

Chapter 5

The long-lived regular quasidiscrete states in the absorption spectrum

In the measured delayed absorption spectrum of Fig. 1.8, we observe a regular sequence of narrow absorption lines near d. In this chapter, we apply the EBK quantization theory to show that those lines correspond to a regular family of quasiperiodic orbits which oscillate about a stable periodic orbit S_+ that we discussed in chapter 2.

According to EBK quantization theory, each quantum state corresponds to a torus having classical actions restricted to certain integer or half-integer values. The main challenge involved in EBK quantization is the determination of the action variables which are defined as the integrations along the independent loops on the torus. So we need to determine the independent loops. For systems with one or two degrees of freedom, caustics [24] or Poincarè surfaces of section [25] provide convenient loops. For systems with dimension three or higher, these methods become difficult [26].

In this chapter, we adapt the Fourier transform method developed by Martens and Ezra [7, 11] to obtain the independent loops of a three dimensional (or a four-dimensional) torus. The key point of this method is to obtain the angle parameterized torus from a numerically integrated regular trajectory by Fourier transformation.

5.1 Theory of the Fourier transform method

The main theme of the Fourier transform method can be summarized in three points:

1. The time dependent Fourier series of the variables of a regular trajectory

   By integrating the equations of motion (2.12), we can obtain numerical data for $[u_i(s), p_i(s), t(s)]$ for a regular trajectory. By inputing $[u_i, p_i]$ into the KS-transformation in (2.4), we can convert the KS variables $[u_i(s), p_i(s), t(s)]$ to the Cartesian variables $[q_i(s), P_i(s)]$ or $[q_i(t), P_i(t)]$.

   Since regular motion is quasiperiodic with three independent fundamental frequencies $\omega = (\omega_1, \omega_2, \omega_3)$ in the physical space, the variables in the six-dimensional physical phase space can be expressed as [11]:

$$\mathbf{q}(t) = \sum_{\mathbf{k}} \mathbf{q_k} exp[i\mathbf{k} \cdot (\tilde{\omega} t + \boldsymbol{\beta})] \tag{5.1}$$

$$\mathbf{p}(t) = \sum_{\mathbf{k}} \mathbf{p_k} exp[i\mathbf{k} \cdot (\tilde{\omega} t + \boldsymbol{\beta})] \tag{5.2}$$

   or

$$\mathbf{q}(s) = \sum_{\mathbf{k}} \mathbf{q_k} exp[i\mathbf{k} \cdot (\omega s + \boldsymbol{\beta})] \tag{5.3}$$

$$\mathbf{p}(s) = \sum_{\mathbf{k}} \mathbf{p_k} exp[i\mathbf{k} \cdot (\omega s + \boldsymbol{\beta})] \tag{5.4}$$

   where $\mathbf{k} = (k_1, k_2, k_3)$ is a vector of integer components, and $\boldsymbol{\beta} = (\beta_1, \beta_2, \beta_3)$ is a vector of initial phase. In our system, coordinates expressed as functions of s vary more

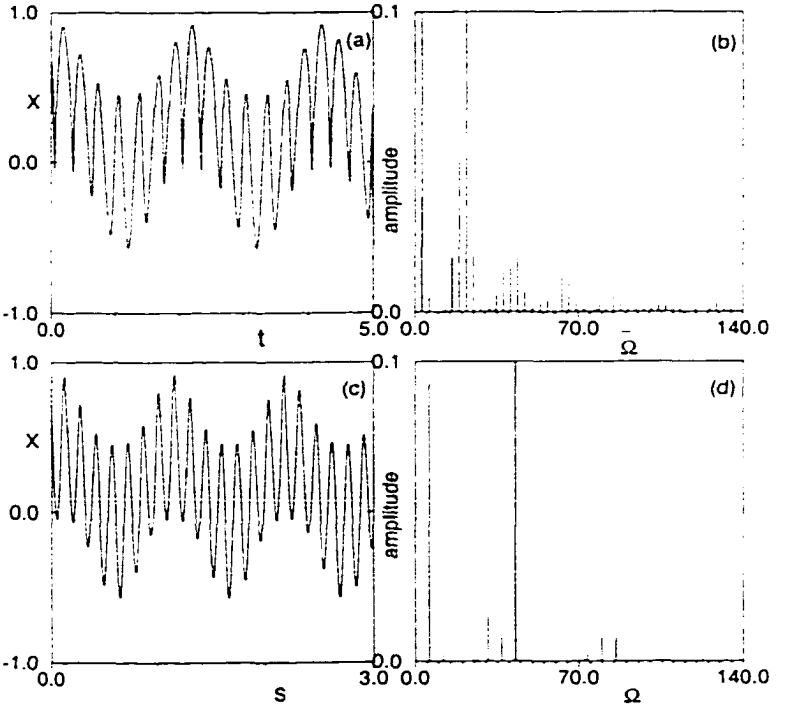

Figure 5.1: Behavior of variables for the trajectory drawn in Fig. 5.2. (a) and (b): $x(t)$ and its Fourier transform. (c) and (d): $x(s)$ and its Fourier transform. $x(t)$ has rather sharp cusps when the electron comes close to the nucleus, so its Fourier transform has many high harmonics. $x(s)$ is smoother, so its Fourier transform has fewer harmonics.

smoothly than those expressed as functions of t (Fig. 5.1(a),(c)): it follows that the Fourier series in the variable s are simpler and have better convergence than those in t (Fig. 5.1(b),(d)). Therefore, we Fourier-transform the numerical data of the variables in s to determine the fundamental frequencies, the amplitude of each oscillatory term, and the initial phase. The detailed numerical procedure and numerical techniques are summarized in the next section.

2. The angle-parameterized torus from a regular trajectory

Regular motion admits action-angle variables $(\boldsymbol{\theta}, I)$ with properties that the actions $\mathbf{I} = (I_1, I_2, I_3)$ are constant and the angles $\boldsymbol{\theta} = (\theta_1, \theta_2, \theta_3)$ evolve linearly in time:

$$\boldsymbol{\theta}(s) = \boldsymbol{\omega} s + \boldsymbol{\beta} \tag{5.5}$$

Therefore, the Fourier series of the variables can be interpreted as the transformation equations from $(\boldsymbol{\theta}, \boldsymbol{I})$ to $(\mathbf{q}, \mathbf{p})$ with actions fixed:

$$\mathbf{q}(\theta, \mathbf{I}) = \sum_{\mathbf{k}} \mathbf{q_k}(\mathbf{I}) exp[i\mathbf{k} \cdot \boldsymbol{\theta}] \tag{5.6}$$

$$\mathbf{p}(\theta, \mathbf{I}) = \sum_{\mathbf{k}} \mathbf{p_k}(\mathbf{I}) exp[i\mathbf{k} \cdot \boldsymbol{\theta}] \tag{5.7}$$

This gives us the angle-parameterized torus.

Since $\mathbf{q}$ and $\mathbf{p}$ must be real, $\mathbf{q_k}$ and $\mathbf{p_k}$ must satisfy:

$$\mathbf{q_k}^* = \mathbf{q_{-k}}$$

$$\mathbf{p_k}^* = \mathbf{p_{-k}}$$

Let $\mathbf{q_k} = |\mathbf{q_k}| e^{i\phi_{\mathbf{q_k}}}$ and $\mathbf{p_k} = |\mathbf{p_k}| e^{i\phi_{\mathbf{p_k}}}$; then we can rewrite the angle-parameterized torus equations as

$$\mathbf{q}(\theta_1, \theta_2, \theta_3) = \mathbf{q}_{000} + 2 \sum_{\mathbf{k}}{}' |\mathbf{q_k}| cos(\mathbf{k} \cdot \boldsymbol{\theta} + \phi_{\mathbf{q_k}}) \tag{5.8}$$

$$\mathbf{p}(\theta_1,\theta_2,\theta_3) = \mathbf{p}_{000} + 2\sum_{\mathbf{k}}{}' |\mathbf{p_k}| cos(\mathbf{k}\cdot\boldsymbol{\theta} + \phi_{\mathbf{p_k}}) \quad (5.9)$$

where the primed summation sums over the terms with $\mathbf{k}\cdot\boldsymbol{\omega} > 0$ only.

3. Three independent loops and actions along the loops

Three independent loops can be defined as loops with one angle variable varying from 0 to 2π and other two angles fixed. We show three independent loops C_i in Fig. 5.2. which are loops with θ_i varying from 0 to 2π and θ_j, θ_k equal to zero:

$$\mathbf{q}(\theta_i) = \mathbf{q}_{000} + 2\sum_{\mathbf{k}}{}' |\mathbf{q_k}| cos(k_i\theta_i + \phi_{\mathbf{q_k}}) \quad (5.10)$$

$$\mathbf{p}(\theta_i) = \mathbf{p}_{000} + 2\sum_{\mathbf{k}}{}' |\mathbf{p_k}| cos(k_i\theta_i + \phi_{\mathbf{p_k}}) \quad (5.11)$$

Actions along the loops are

$$\begin{aligned} I_i &= 1/2\pi \oint_{C_i} \mathbf{p}\cdot d\mathbf{q} \\ &= 1/2\pi \oint_{C_i} \mathbf{p}\cdot\frac{d\mathbf{q}}{d\theta_i}d\theta_i \end{aligned} \quad (5.12)$$

Substituting the loop functions (5.10,5.11) into this equation and performing the integration yields:

$$I_i = 2\sum_{\mathbf{k}}{}' k_i |\mathbf{q_k}||\mathbf{p_k}| cos(\phi_{\mathbf{q_k}} - \phi_{\mathbf{p_k}}) \quad (5.13)$$

The actions depend on $\mathbf{k}$ not only through the amplitudes $\mathbf{q_k}$ and $\mathbf{p_k}$ but also the phases of $\mathbf{q_k}$ and $\mathbf{p_k}$. This is different from Ref. [7, 11] where the actions depend on the k only through the amplitudes $\mathbf{q_k}$. The determination of phases requires high precision in the determination of the fundamental frequencies. A way to achieve precision of 10^{-7} in the frequencies is discussed in the next section. Examing Fig. 5.2. we rename the loops (C_1, C_2, C_3) as $(C_{\rho+\phi}, C_\phi, C_z)$, and the corresponding action variables as $(I_{\rho+\phi}, I_\phi, I_z)$.

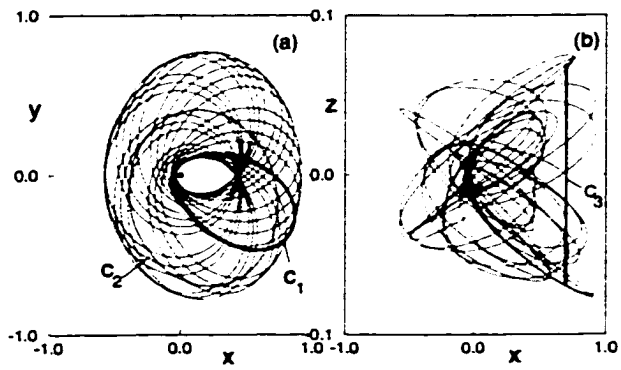

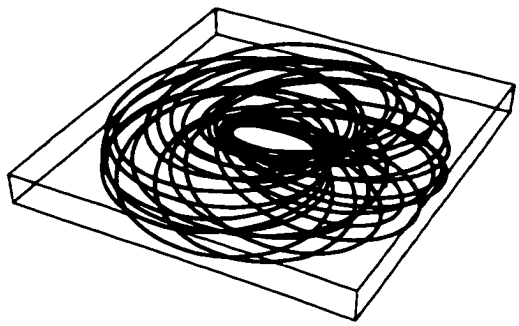

Figure 5.2: The torus explored by the trajectory launched at $E = -110cm^{-1}$ or $\epsilon = -0.5779$, $\theta = 87^0$ and $\phi = 140^0$ and the three loops C_i with $i = (1, 2, 3)$ used to calculate the actions. In (a), (b), we show the loops and the trajectory in two dimensional spaces xy and xz, then show all of them in a three dimensional graph below (a) and (b). (Note the small range of z motion) The first loop C_1 touches two caustics, and includes one loop of angular motion and one loop of radial motion; the second loop C_2 is a loop of angular motion and it touches no caustics; the third loop is one loop of z motion, touching two caustics.

5.2 The computational procedure and techniques of EBK quantization

In the preceding section, we gave a general sketch of the Fourier-transform method for calculating and quantizing tori. Here we give additional details of the procedure. The reader who does not need these details can skip to section 5.3. The primary problem is that Martens and Ezra [7, 11] considered Hamiltonians in the form:

$$H(\mathbf{q},\mathbf{p}) = \frac{1}{2}\sum_{j=1}^{N} p_j^2 + V(q_1, q_2, ..., q_N). \tag{5.14}$$

However we have a "paramagnetic" term in the Hamiltonian. Therefore, p_i is not equal to du_i/ds, and P_i is not equal to dq_i/dt, and so the Fourier series for $u_i(s)$ does not directly give the Fourier series for $p_i(s)$. Hence we have to obtain the series for both $u_i(s)$ and $p_i(s)$ via Fourier transformation. Furthermore, our actions in Eq. (5.13) depend on not only the magnitude, but also the phases of the Fourier series. Because the determination of the phases requires high precision in the determination of the frequencies, we combine two types of Fourier transform (Fast-Fourier-Transform and Quadrature-Fourier-Transform) to achieve precision of 10^{-7} in the determination of the fundamental frequencies.

Below we summarize our numerical procedure and computational techniques.

- **Initial conditions for the classical trajectories**

  In chapter 2, we pointed out that the variables in KS space determine the variables in Cartesian space uniquely, but the converse is not true. We also presented a method to initiate the trajectories at the origin in the KS space. Here we describe a method to initiate the trajectories from other places instead of the origin in KS space.

  For the crossed field system, there are two elementary periodic orbits (S_+, S_-), which are well studied by Flötman and Welge [13]. S_+ is a periodic orbit which goes around

in a right hand sense relative to the magnetic field $\vec{B}$. On this orbit, both the Coulomb force and the Lorenz force point inward. This orbit is stable and quasielliptical in the whole energy range we study. Let's label the coordinate of the crossing of S_+ on the positive x axis as x_r. With $B = 6.002T$ and $F = 1000V/cm$, we numerically calculate x_r at different scaled energies ϵ and find a relation of x_r and ϵ by least-square fit:

$$x_r = a_0 + b_0\epsilon + c_0\epsilon^2 \tag{5.15}$$

We launch trajectories at $x = x_r(\epsilon), y = 0$ and $z = 0$ along directions defined by polar angle θ and azimuthal angle ϕ. If we define

$$\epsilon' = \epsilon + 1/x_r - fx_r \tag{5.16}$$

then the momenta in the physical space are given by

$$\begin{aligned} p_x &= \sqrt{2\epsilon'}sin\theta cos\phi \\ p_y &= \sqrt{2\epsilon'}sin\theta sin\phi \\ p_z &= \sqrt{2\epsilon'}cos\theta \end{aligned}$$

Now we compute the initial conditions for u_α and $p_\alpha (\alpha = 1, 2, 3, 4)$ from

$$u_1^2 + u_4^2 = \frac{1}{2}(r + z), u_2 = \frac{xu_1 + yu_4}{r + z}, u_3 = \frac{yu_1 - xu_4}{r + z}$$

and

$$\begin{aligned} p_1 &= 2(u_1p_z + u_2p_x + u_3p_y) \\ p_2 &= 2(-u_2p_z + u_1p_x + u_4p_y) \\ p_3 &= 2(-u_3p_z - u_4p_x + u_1p_y) \\ p_4 &= 2(u_4p_z - u_3p_x + u_2p_y) \end{aligned}$$

Taking initially $u_4 = 0$, the initial conditions are:

$$\begin{aligned} u_1 &= \sqrt{x_r/2}, & p_1 &= 2u_1(p_z + p_x) \\ u_2 &= u_1, & p_2 &= 2u_2(-p_z + p_x) \\ u_3 &= 0, & p_3 &= 2u_1 p_y \\ u_4 &= 0, & p_4 &= 2u_2 p_y \end{aligned}$$

- **Numerically integrated time series of coordinate and momentum variables**

  From now on, we use (q_i, P_i) with $(i = 1, 2, 3)$ to label the coordinate and momentum variables in physical space and (u_i, p_i) with $(i = 1, 2, 3, 4)$ to label the coordinate and momentum variables in KS space.

  We initiate a trajectory in the way described above and integrate the equations of motion given by (2.12) until we obtain 130000 records of the time series $u_i(s)$ with step length $\delta s = 0.01$. If the trajectory does not pass close to the nucleus, we can convert the KS variables $[u_i(s), p_i(s), t(s)]$ to the Cartesian variables $[q_i(s), P_i(s)]$ or $[q_i(t), P_i(t)]$. Then we carry out the subsequent calculations in the Cartesian space. However, if the trajectory passes close to the origin, we are forced to carry out the calculations of actions and angles in KS space, and later transform the action variables in KS space back to action variables in Cartesian space.

  As shown in Fig. 5.1, coordinates expressed as functions of s vary more smoothly than those expressed as functions of t, so Fourier transforms are simpler and have better convergence. Therefore, we use time series in s for all of our calculations.

- **Determination of the fundamental frequencies**

  1. If the trajectory does not pass near the origin, we do the calculations in Cartesian space, where there are three fundamental frequencies.

In our system, we need to obtain the frequencies with very high precision, so we use two Fourier transform methods together: a Fast-Fourier-Transform (FFT) and a Quadrature-Fourier-Transform (QFT). The FFT beats the QFT in speed. If we measure speed in the time complexity (a measure of the number of operations needed), the FFT is $O(Nlog_2N)$ while the QFT is $O(N^2)$, where N is the number of the data points. For example, in our calculation with $N = 130000$, the QFT is about 11000 slower than the FFT. However, the QFT beats the FFT in precision because FFT generates output at fixed points. With the QFT, we can select the output points in a small region with small steps, and this achieves better precision and avoids redundant calculation if we know the approximate positions of frequencies. In our method, we first use FFT to identify approximate positions of the fundamental frequencies, then we use QFT to obtain two hundred Fourier transform outputs near each fundamental frequency with a small step of 10^{-4}. After that we fit these two hundred points to a Gaussian function by a nonlinear least-squares routine. The centers of the peaks are the fundamental frequencies. We test this method in the determination of the fundamental frequencies on the S_+ fundamental periodic orbit because we can numerically integrate the periodic orbit to find the exact frequency of the periodic orbit. Our test shows that this method calculates this frequency to an accuracy of 10^{-7}.

As Martens and Ezra did in [11], we multiply the time series of $x(s)$ and $z(s)$ with a Blackman-Harris window function $B(s)$,

$$B(s) = \sum_{j=0}^{3}(-1)^j a_j cos(2\pi js/S),$$

where $a_0 = 0.40217$, $a_1 = 0.49703$, $a_2 = 0.09392$, $a_3 = 0.00183$, and S is the length of the time series, then we Fourier transform the products $x(s)B(s)$ and $z(s)B(s)$ to obtain the fundamental frequencies. The window function sharpens

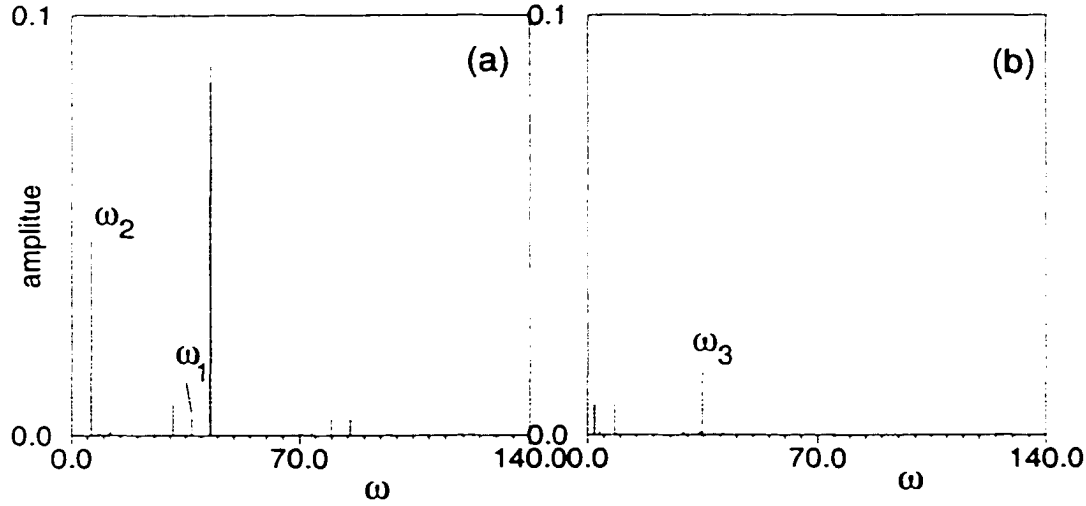

Figure 5.3: The Fourier transform of $x(s), z(s)$ for the trajectory drawn in Fig. 5.2(a): the Fourier transform of $x(s)$; (b) the Fourier transform of $z(s)$. The three fundamental frequencies are labeled as ω_1, ω_2 and ω_3. Numbers given are in scaled units defined by Eq. (2.2) and Eq. (2.11).

the peaks and gets rid of side bands.

A calculated Fourier transform is shown in Fig. 5.3. Now we should identify the fundamental frequencies. They are neither necessarily the smallest frequencies nor the ones with largest amplitudes. We should identify three frequencies $(\omega_1, \omega_2, \omega_3)$ such that every frequency ω in the spectrum is some combination of ω_1, ω_2, and ω_3, that is $\omega = k_1\omega_1 + k_2\omega_2 + k_3\omega_3$, where k_1, k_2 and k_3 are integers (see Fig. 5.3).

2. If the trajectory passes near the origin, we do the calculations in four dimensional KS space. In this space there are four fundamental frequencies.

   The KS transformation gets rid of the singularity in our Hamiltonian at the cost of lifting our system to a space with one more degree of freedom. For example, the orbit S_+ is periodic, and explores a one dimensional curve in physical space. However, in KS space, it is quasiperiodic with two fundamental frequencies, and

it explores a two dimensional torus (Fig. 5.4). The projections of the torus in (u_1, u_4) and (u_2, u_3) subspaces show that the motions along u_1 and u_4 are nearly resonant and u_2 and u_3 are nearly resonant. As a result, the trajectory fills a disc in either of these spaces. However, when plotted in (u_1, u_2) or in (u_3, u_4), the motion is nonresonant, and the trajectory fills a parallelogram.

Just as the one dimensional periodic orbit fills a torus in KS space, so a three dimensional torus in physical space becomes a 4-dimensional torus in KS space. Then there are four fundamental frequencies. We find that for typical orbits, if we get a good Fourier transform in both spaces, then we can identify four fundamental frequencies in KS space ($\omega_i', i = 1, 2, 3, 4$) and three fundamental frequencies in physical space ($\omega_i, i = 1, 2, 3$). We find that they are related by (Fig. 5.5):

$$\begin{aligned} \omega_1 &= 2\omega_1' \\ \omega_2 &= \omega_2' \\ \omega_3 &= \omega_1' + \omega_3' \end{aligned}$$

Using this information, we compute and quantize additional tori in KS space - in particular the tori for which the orbits that come close to the nucleus. The advantage of calculation in physical space is the lower dimension, while the advantage of calculation in KS space is that we can more easily calculate orbits that come close to the nucleus.

- **Determination of the amplitudes**

In determining the amplitudes, we use another window function $W(s)$ which is provided in [11],

$$W(s) = (2k/S)\frac{sin[2\pi K(s/S - 1/2)]}{2\pi K(s/S - 1/2)}.$$

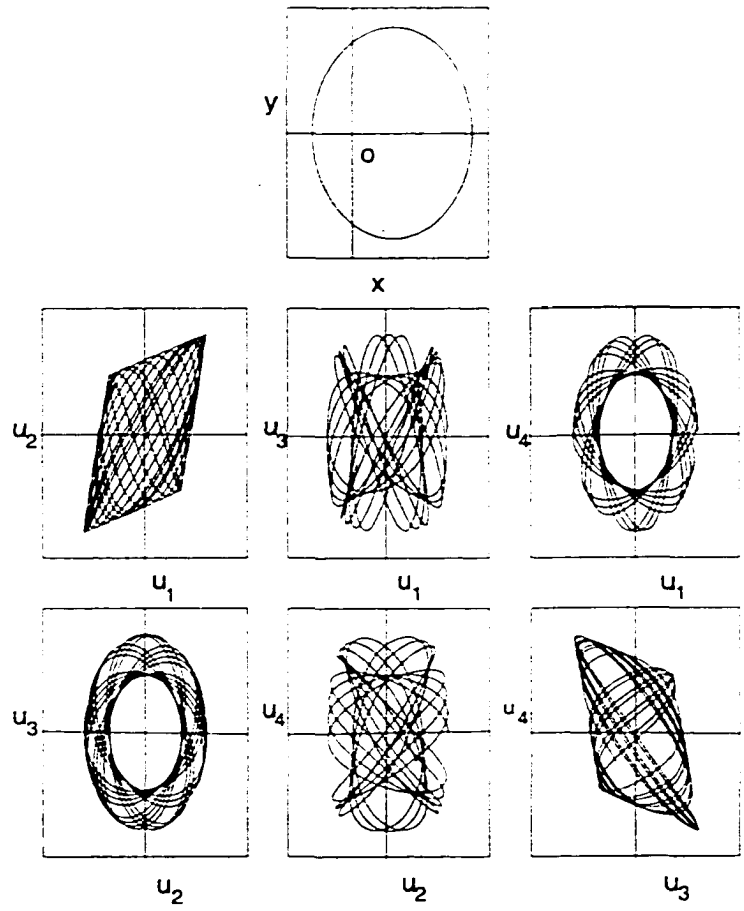

Figure 5.4: The S_+ periodic orbit at $E = -110cm^{-1}$ is drawn in different space. In xy spaces, it is periodic: in KS space, it explores a two dimensional torus. The motions in (u_1, u_4) or (u_2, u_3) are resonant, but the motions in (u_1, u_2) or (u_3, u_4) are nonresonant.

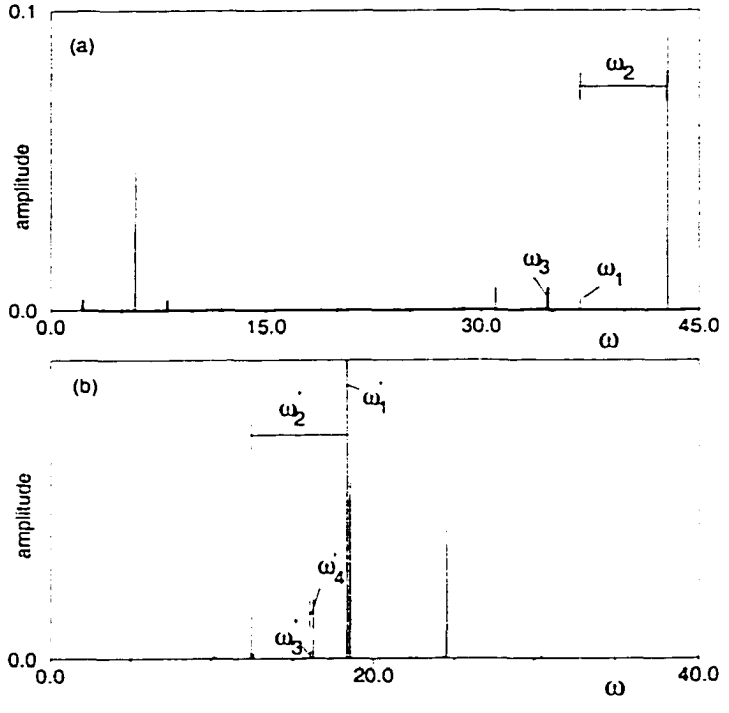

Figure 5.5: (a) The Fourier transform of $x(s)$(fine line) and $z(s)$ (Bold line), and (b) the Fourier transform of $u_1(s)$ for the trajectory drawn in Fig. 5.2. The Fourier transforms of $x(s)$ and $z(s)$ have three fundamental frequencies: $\omega_1 = 36.964077$, $\omega_2 = 5.949679$, $\omega_3 = 34.708708$; the Fourier transform of $u_1(s)$ has four fundamental frequencies: $\omega_1' = 18.482038$, $\omega_2' = 5.949679$, $\omega_3' = 16.226670$, $\omega_4' = 0.088140$. Numbers given are in scaled units defined by Eq. (2.2) and (2.11).

Again S is the length of the time series. This window function flattens the peak and makes the amplitudes nearly constant over the frequency width $4\pi K/S$. Therefore, we can reduce error in determination of the amplitudes. The specific steps are:

1. Use the fundamental frequencies to find the frequencies of the harmonics:

$$\Omega = \mathbf{k} \cdot \boldsymbol{\omega} \tag{5.17}$$

where $\mathbf{k} = (k_1, k_2, k_3)$ in physical space or $\mathbf{k} = (k_1, k_2, k_3, k_4)$ in KS space. k_i is restricted to some finite range chosen to obtain adequate convergence of the Fourier series. In our case, $|k_1| \leq 15$, $|k_2| \leq 8$, $|k_3| \leq 5$ and $|k_4| \leq 1$.

2. Multiply the time series with $B(s)W(s)$ with $K = 3$, then Fast-Fourier-Transform $q_i(s)B(s)W(s)$ and $P_i(s)B(s)W(s)$ to obtain the amplitudes $q_{\mathbf{k}}$ and $p_{\mathbf{k}}$ at each harmonic. The technique to determine the amplitudes through the outputs of Fast-Fourier-Transform is discussed in the appendix of [7]. The only difference in our method is the line shape function given by:

$$F(\delta) = \sum_{i=0}^{3} b_i \delta^i \tag{5.18}$$

with $b_0 = 0.994325177$, $b_1 = -1.75090016 \times 10^{-6}$, $b_2 = -3.84542243 \times 10^{-3}$, $b_3 = -1.38388465 \times 10^{-4}$.

- **Classical actions of the torus**

Once we obtain the amplitudes at each harmonic, we input them into Eq. (5.13) to calculate actions. If we carry out the calculations in KS space, we have four actions I_i' with $i = (1, 2, 3, 4)$. By comparing the actions in physical space and the actions in KS space for those trajectories which do not pass through the origin, we found their relationship:

$$I_{\rho+\phi} = I_1 \quad = \quad (I_1' - I_3')/2 - I_4'$$

$$I_\phi = I_2 = I_2' - I_4' \tag{5.19}$$
$$I_z = I_3 = I_3' - I_4'$$

Then with the actions in KS space, we can obtain the actions in physical space.

5.3 Semiclassical energy spectrum

Since we are only interested in the energy eigenvalues, we do not need to compute every eigentorus. We calculate the actions $(I_{\rho+\phi}, I_\phi, I_z)$ of trajectories with various initial conditions at various energies, and we fit the data set $(I_{\rho+\phi}, I_\phi, I_z, E)$ to a smooth function,

$$\begin{aligned} E = {} & a_0 + a_1 I_{\rho+\phi} + a_2 I_\phi + a_3 I_z + a_4 I_{\rho+\phi}^2 + a_5 I_\phi^2 + a_6 I_z^2 \\ & a_7 I_{\rho+\phi} I_\phi + a_8 I_{\rho+\phi} I_z + a_9 I_\phi I_z \end{aligned} \tag{5.20}$$

determining the coefficients $a_0 ... a_9$ by using a nonlinear least-squares fit routine. Then we input appropriately quantized values of the actions I to find the corresponding energy eigenvalue [25]. In our calculation, the maximum error of our fit function (5.20) is less than $10^{-2} cm^{-1}$. Therefore the numerical precision of our calculated semiclassical energy eigenvalues should be about $10^{-2} cm^{-1}$.

According to EBK quantization theory, the quantization conditions for $I_{\rho+\phi}, I_\phi, I_z$ are:

$$\begin{aligned} I_{\rho+\phi} &= n_{\rho+\phi} + 1/2, \\ I_\phi &= n_\phi, \\ I_z &= n_z + 1/2, \end{aligned}$$

where the half-integer results from the fact that the loops $C_{\rho+\phi}$ and C_z each touch caustics twice. We also define a principal action I as

$$I = I_{\rho+\phi} + I_z.$$

So the quantization condition for I is

$$I = n = n_{\rho+\phi} + n_z + 1.$$

We call n the principal quantum number. Since there is a one-to-one correspondence between the eigentori (whose actions satisfy the quantization condition) and the quantum states, we can use $(n_{\rho+\phi}, n_\phi, n_z)$ or (n, n_ϕ, n_z) to label the states. Here we use the latter.

Our calculation shows that the states we identified all have n_z equal to zero: they have only "zero-point" motion out of plane. Therefore we only use (n, n_ϕ) to label the states. In Table 5.1, we list the semiclassical energy eigenvalues with the quantum numbers of the actions. We also list the experimental values and the values obtained by a quantum mechanical method [27] for comparison. The accuracy of the experiment is $0.007cm^{-1}$.

We mark the identified states on the measured absorption spectrum graph (see Fig. 5.6). The states in the energy range near d in Fig. 1.8 fall into different sequences. The sequences are distinguished by the principal quantum number and the members of a sequence are distinguished by the quantum number n_ϕ. Hence we have proved that the regular quasidiscrete states in the absorption spectrum correspond to regular tori which stay close to the xy plane and oscillate around the stable periodic orbit S_+.

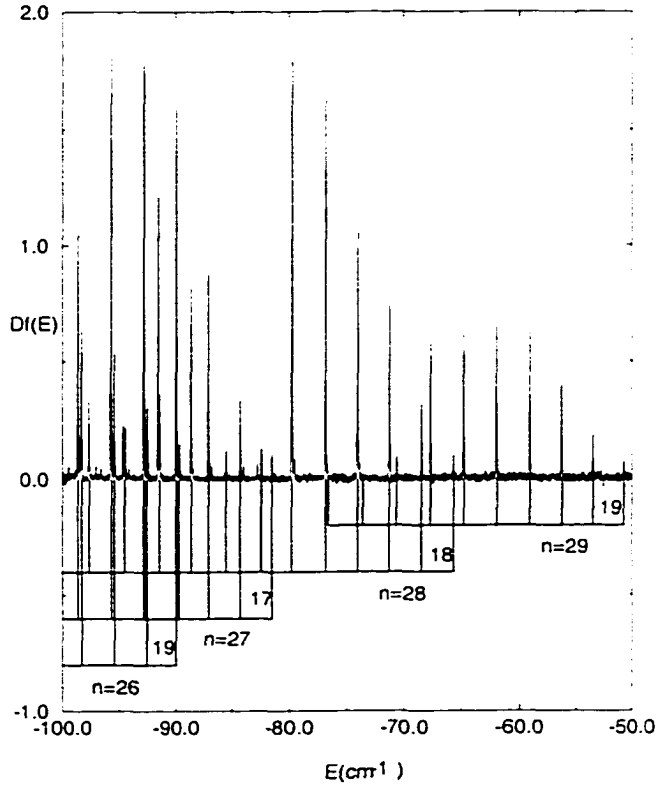

Figure 5.6: The measured delayed absorption spectrum at $F = 1000V/cm$ and $B = 6.002T$. The quantum states are organized by the principal quantum numbers n and the angular quantum number n_ϕ corresponding to the principle action and the azimuthal action. The states with the same quantum number n belong to the same sequence and the states in the same sequence are distinguished by the quantum number n_ϕ.

Table 5.1: List of the energy eigenvalues: $E_{exp}, E_{exact}, E_{semi}$

n	n_o	$E_{exp}(cm^{-1})$	$E_{exact}(cm^{-1})$	$E_{EBK}(cm^{-1})$
26	9	-118.66132		-118.62790
26	10	-115.71537	-115.73	-115.71750
26	11	-112.77931	-112.79	-112.78747
26	12	-109.86435	-109.86	-109.83005
26	13	-106.96499	-106.97	-106.96124
26	14	-104.11635	-104.10	-104.09301
26	15	-101.23860	-101.23	-101.22536
26	16	-98.27655	-98.30	-98.25884
26	17	-95.37632	-95.39	-95.34356
26	18	-92.48411	-92.51	-92.54291
26	19	-89.92901	-89.94	-89.95688
27	4	-119.83373		-119.82059
27	5	-116.74612	-116.80	-116.75103
27	6	-113.66907	-113.71	-113.69182
27	7	-110.61467	-110.64	-110.60441
27	8	-107.57874	-107.61	-107.58828
27	9	-104.57000	-104.59	-104.57163
27	10	-101.59217	-101.25	-101.50445
27	11	-98.61679	-98.65	-98.61998
27	12	-95.70321	-95.72	-95.65637
27	13	-92.80433	-92.82	-92.80165
27	14	-89.65549	-89.65	-89.71642
27	15	-87.07754	-87.09	-87.07008
27	16	-84.26893	-84.26	-84.27282
27	17	-81.47313	-81.46	-81.47466

Chapter 6

Organization and Bifurcations of planar closed orbits

As we mentioned in chapter 3, each closed orbit produces a sinusoidal oscillation in the absorption spectrum as a function of energy, and it produces a peak in the recurrence spectrum. As the energy changes, new closed orbits are created via bifurcations, so new peaks appear in the recurrence spectrum. Therefore, the patterns of bifurcations and the organization of closed orbits are of fundamental interest for understanding of the spectrum. These have been studied experimentally and theoretically for Rydberg atoms in a magnetic field [28, 29] or in an electric field [30, 31] separately as well as in parallel electric and magnetic fields [32, 33].

In [34], Gao organized the closed orbits of pure electric field system by their winding ratio. In this integrable system, all orbits form tori, and periodic orbits correspond to tori with rational winding numbers. Each such rational torus is filled by a family of periodic orbits with fixed action variables and varying relative phases. Each orbit that is closed at the nucleus is one of these periodic orbits. Therefore, Gao showed that we can understand the

closed orbits by understanding the rational tori. As the energy increases, a rational torus, together with its associated closed orbit, bifurcates out of the "downhill" orbit, evolves to an uphill orientation, and then disappears by merging with the "uphill" orbit.

The crossed-field system is completely different. First, part of phase space is filled with chaotic orbits. However, at low energies, regular orbits dominate, so we can gain insight by first focusing our attention on these. For simplicity, we also restrict our attention to orbits which lie in the plane perpendicular to the magnetic field.

We find that because this system has lower symmetry than the parallel-fields system, closed orbits do not in general correspond to periodic orbits. Therefore, none of the well-developed theory of bifurcations of periodic orbits can be applied. We get new patterns of creation and splitting of closed orbits. Some of these patterns are sufficiently similar to the patterns seen in bifurcations of periodic orbits that we can use the same names. We will refer to a "tangent bifurcation" and a "pitchfork bifurcation". However, it must be remembered that we are dealing here with a different phenomenon.

In this chapter, we first present an "observed" sequence of bifurcations of closed orbits (observed by numerical experiment). Then we define a half-Poincaré map which we use to interpret observations. We create a simple model Hamiltonian to model the half-map and illustrate the sequence of bifurcations of closed orbits. Subsequently, we show that bifurcations of the closed orbits in the crossed field system fall into the same sequence as that in the model Hamiltonian. Finally we present a way to organize the planar closed orbits (where "planar" means xy plane) into families and assign each family a family name and each member of a family a given name.

"Closed" always means closed at the nucleus; typically the electron leaves the atom in one direction and returns from another, and the orbit is not periodic. However, as we will see below, some orbits are both closed and periodic.

6.1 The observed sequence of bifurcations of the closed orbits

We have observed two typical sequences of bifurcations of closed orbits. One is shown in Fig. 6.1. In a region of phase space where there is no closed orbit, as the energy is decreased, abruptly a closed orbit appears. We name this one $C_{2,3}$; the names will be explained as we develop the theory. This closed orbit immediately splits into two closed orbits $(C^{-}_{2,3}, C^{+b}_{2,3})$. This creation of a new closed orbit and the splitting of this orbit into two closed orbits we call a tangent bifurcation. As the energy increases further, each of these closed orbits changes its shape, and in particular, $C^{+b}_{2,3}$ evolves until at some energy it becomes both closed at the nucleus and periodic. We then call it $P_{2,3}$. Then two other periodic orbits $(P^{+}_{2,3}, P^{-}_{2,3})$ split out of $P_{2,3}$, while $P_{2,3}$ returns to being closed but nonperiodic. We call the closed orbit $C^{+a}_{2,3}$. Therefore, we observe that the closed orbits appear in a group of four in an orderly sequence. We call this the "normal sequence" of bifurcations of closed orbits.

A different sequence is shown in Fig. 6.2. A closed orbit $C^{+b}_{3,5}$ exists at very low energies. As energy increases, it evolves into one periodic orbit $P_{3,5}$ first, then becomes a nonperiodic orbit $C^{+a}_{3,5}$, and two periodic orbits $(P^{+}_{3,5}, P^{-}_{3,5})$ are created. Here, we observe that the closed orbits appear in a group of three in an orderly sequence. We call this the "truncated sequence" of bifurcations of closed orbits.

The purpose of this chapter is to understand these sequences of creation and splitting of closed orbits. We first give more detail about the crossed-field system, then we create a simple model. This simple model has sequences of bifurcations of closed orbits which are analogous to the "normal sequence" and the "truncated sequence" of bifurcations in the crossed-field system.

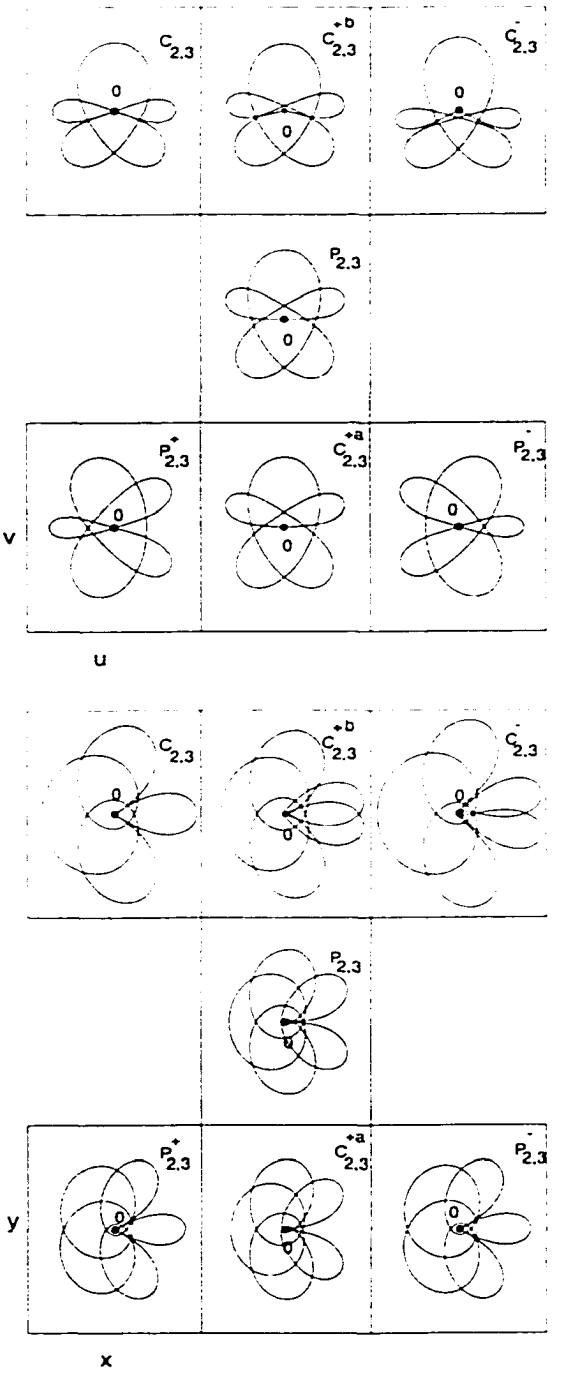

Figure 6.1: An example of the normal sequence of bifurcations of closed orbits. A single closed orbit is created which splits into two (tangent bifurcation). One of them becomes periodic, and then splits off two periodic orbits, becoming again closed but nonperiodic (pitchfork bifurcation).

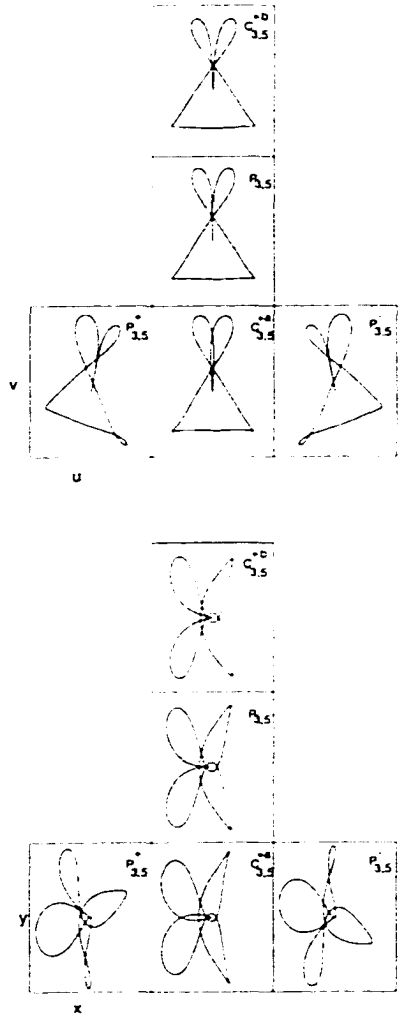

Figure 6.2: An example of the truncated sequence of bifurcations. The orbit $C^{+b}_{3,5}$ exists at very low energies, and as the energy is raised, it undergoes a pitchfork bifurcation.

6.2 Two elementary periodic orbits and their role in the organization of planar motions

The regularized Hamiltonian for planar motions is given by:

$$\frac{2}{\omega} = \frac{1}{2}(p_u^2+p_v^2)+\frac{1}{2}(u^2+v^2)+\frac{f}{2\omega^3}(u^4-v^4)+\frac{1}{4\omega^2}(up_v-vp_u)(u^2+v^2)+\frac{1}{32\omega^4}(u^2+v^2)^3 \quad (6.1)$$

with $\omega = \sqrt{-2\epsilon}$, ϵ is the rescaled energy, and f is the rescaled electric field. In chapter 2, we showed that there are two fundamental planar periodic orbits S_+ and S_-, and they are the "organizers" of the planar motions.

Fig. 6.3 shows the surfaces of section calculated in two different ways at various energies. The surfaces of section on the left are defined by $u = 0$ with $u' > 0$ and the surfaces of section on the right are defined by $v = 0$ with $v' > 0$. The smooth curves on the surface of section (SOS) correspond to regular tori and they are organized into two groups: one is centered at S_+ and another is centered at S_-. However, there is no fundamental distinction between these two groups, since they are not separated by an unstable periodic orbit with a separatrix.

The origin in coordinate space ($u = 0, v = 0$) directly corresponds to the p_u or p_v axis on the SOS, so orbits that are closed at the nucleus are orbits that begin and end on the momentum axis p_u or p_v on the SOS. We may focus our attention on the behavior of the loops on the left-hand-side of each SOS – the loops surrounding S_+ on the $u = 0$ SOS or the loops surrounding S_- on the $v = 0$ SOS.

6.3 Poincaré half-map

The conventional full Poincaré map is commonly used to study bifurcations of the closed periodic orbits [34]. On the surface of section (SOS) generated by the full Poincaré

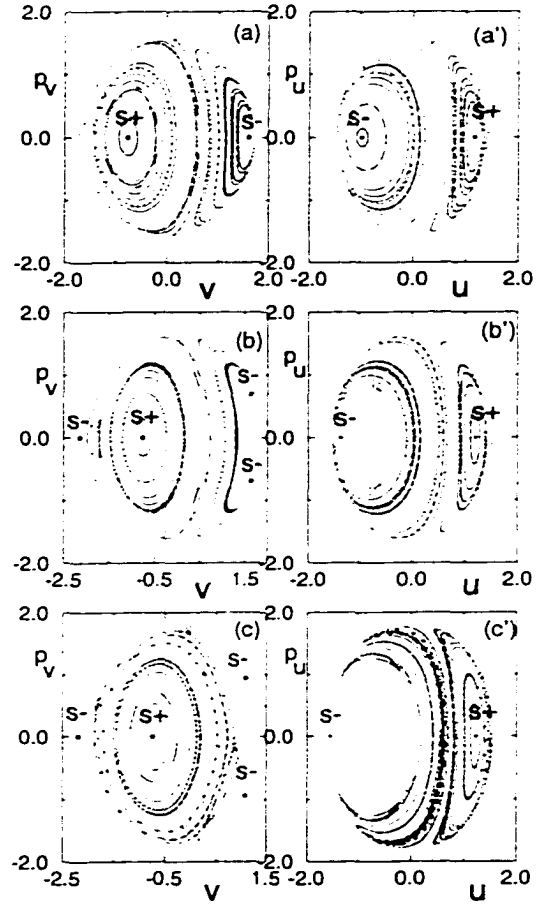

Figure 6.3: The collection of the sos at three different energies with fixed external fields $B = 6T$. $F = 1000V/cm$ or $f = 0.2587$: (a) $E = -250cm^{-1}$ or $\epsilon = -1.313$ and $\omega = 1.620$; (b) $E = -190cm^{-1}$ or $\epsilon = -0.998$ and $\omega = 1.413$; (c) $E = -140cm^{-1}$ or $\epsilon = -0.736$ and $\omega = 1.213$.

map. periodic orbits show up as fixed points, so they can be easily located. However, since most of the closed orbits in the crossed field system are nonperiodic. the full Poincaré map is not so helpful. In this section, we define a Poincaré half-map, which is more useful.

6.3.1 Full Poincaré map

Choosing the surface $q_i = 0$, we define a map $(q_{j_0}, p_{j_0}) \rightarrow (q_{j_1}, p_{j_1})$ by starting the trajectories on the surface $q_i = 0$ with $\dot{q}_i > 0$, integrating the $(q_i(t), q_j(t), p_i(t), p_j(t))$ equations and stopping whenever they pass through $q_i = 0$ with $\dot{q}_i > 0$ again, then recording (q_j, p_j). This is called the Poincaré full map M_p. We denote the pair of variables (q_j, p_j) as

$$z \equiv (q_j, p_j), \tag{6.2}$$

and the mapping is abbreviated as

$$z_1 = M_p(z_0; \epsilon, f), \tag{6.3}$$

where i and j denote different canonical pairs of spatial coordinates and momenta.

The iterations of the Poincaré full map give us the conventional Poincaré SOS. Each fixed point on the SOS corresponds to a periodic orbit of the differential equations.

The surface selected above has its drawback that the trajectories do not always pass through the surface and may be tangent to it. This drawback results in discontinuities of the map. However, we found that the map defined in (6.3) is continuous in substantial regions, hence we can use it to discover orderly bifurcation patterns of closed orbits.

6.3.2 Poincaré half-map

The symmetries of the system allow us to define a kind of "half-map". If we begin trajectories at $q_i = 0$ with $\dot{q}_i > 0$ and stop immediately when they return to $q_i = 0$ with

$\dot{q}_i < 0$, we call this map $M_+(z_0;\epsilon,f)$. Similarly if we start with $\dot{q}_i < 0$ and stop at $q_i = 0$ with $\dot{q}_i > 0$, we call this map $M_-(z_0;\epsilon,f)$. Clearly the full Poincaré map is then

$$M_p(z_0;Es,f) = M_-(M_+(z_0;\epsilon,f)).$$

In appendix D, we will show that because of the symmetries of this system, the maps M_+ and M_- are related by

$$M_-(z_0;\epsilon,f) = -M_+(-z_0;\epsilon,f). \tag{6.4}$$

Therefore,

$$M_p(z_0;\epsilon,f) = M_-M_+(z_0;\epsilon,f) = -M_+(-M_+(z_0;\epsilon,f)). \tag{6.5}$$

that is to say, $M_-M_+ = (-M_+)^2$. We define $-M_+$ as the Poincaré half-map.

6.3.3 Periodic orbits of the Poincaré half-map and the winding ratio of the periodic orbits

- **The correspondence between periodic or closed orbits of the Poincaré half-map and periodic or closed orbits of the dynamical system**

  The Poincaré half-map is defined as $-M_+(z_0,\epsilon,f)$. Starting from any point z_0, we may iterate the map $-M_+$ as many times as we wish,

$$\begin{aligned} z_1' &= -M_+(z_0,\epsilon,f) \\ z_2' &= -M_+(z_1',\epsilon,f) \\ z_3' &= -M_+(z_2',\epsilon,f) \\ z_4' &= -M_+(z_3',\epsilon,f) \\ &\vdots \end{aligned} \tag{6.6}$$

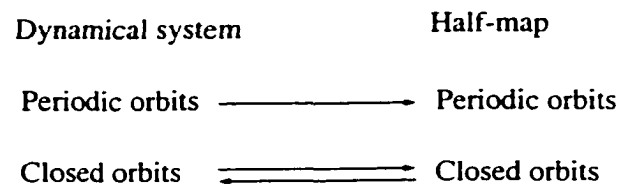

Figure 6.4: Every periodic orbit of the dynamical system (defined by the differential equations) that goes through the surface of section ($u = 0$ or alternatively $v = 0$), is a periodic orbit of some iterate of the half-map. The converse is not necessarily true. Every orbit of the dynamical system that is closed at the origin ($u = 0, v = 0$) is also a closed orbit of some iterate of the half-map. The converse is also true.

We define an periodic orbit of the half map as the set of points $(z_0, z_1', z_2', ..., z_m')$ generated according to Eq. (6.6) such that the m-th iteration returns to the initial point $z_m' = z_0$. We define a closed orbit of the half-map as an orbit such that $q_m' = q_0 = 0$. (Here, as usual, "closed" means closed at the nucleus.)

Every periodic orbit of the dynamical system that goes through the surface of section is also a periodic orbit of some iterate of the half-map. Every closed orbit of the dynamic system is a closed orbit of the half-map, and vice versa (see Fig. 6.4).

- **The winding ratios of the periodic orbits of the Poincaré half-map**

We focus on the loops around S_+ on the $u = 0$ surface to study the closed orbits. In the regular region, S_+ is surrounded by smooth curves, and each curve corresponds to a regular torus in phase space. To show how the trajectories wind around the central periodic orbit, we apply the half map to a horizontal line to get Fig. 6.5. We have the following observations:

1. Points on the SOS wind around the periodic orbit S_+, and we may say that they wind in a clockwise sense.

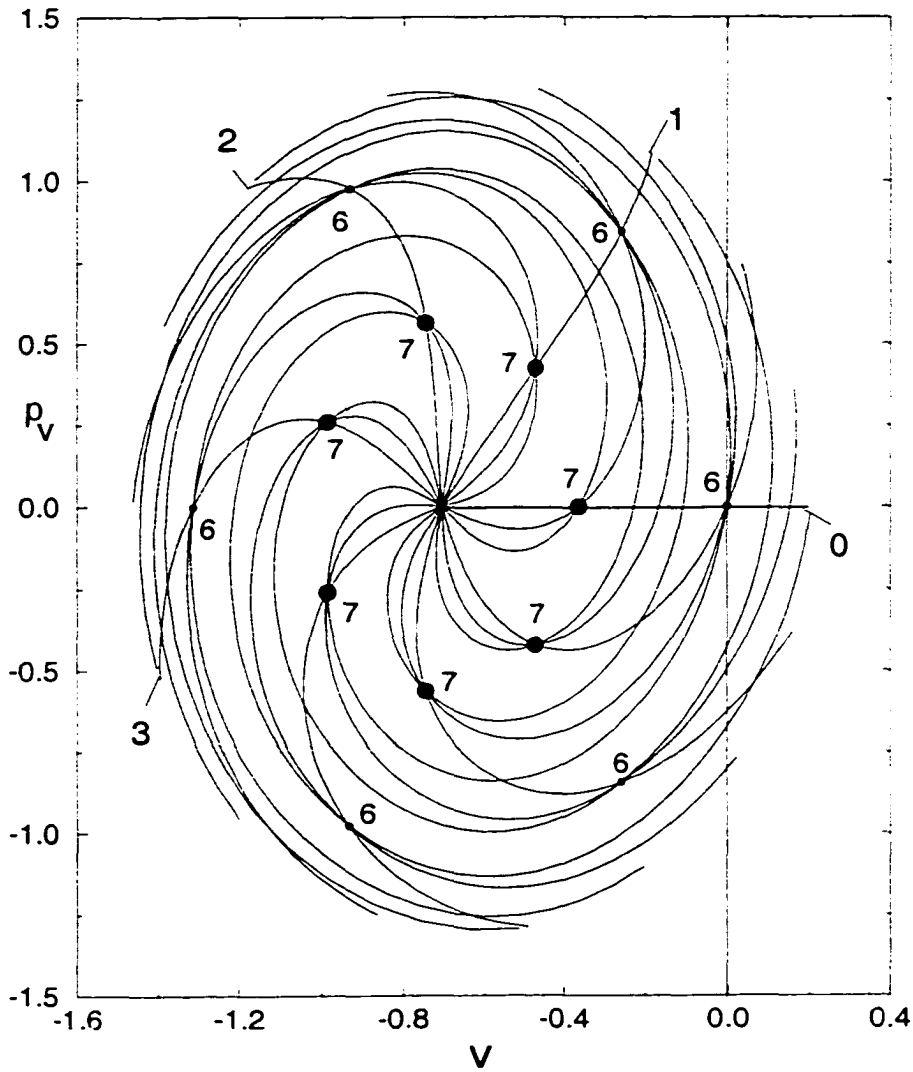

Figure 6.5: The first 20 iterations of the horizontal line at $E = -95cm^{-1}$ with external fields $B = 6T$ and $F = 1000V/cm$. The $5/7$, $2/3$ periodic orbits are marked by dots and labeled by 7 and 6. We use bold $0, 1, 2, 3$ to label the initial horizontal line and the first, second and third iteration of the initial line respectively.

2. The winding rate decreases as we go farther from the central periodic orbit S_+. (If we travel outward from S_+ on a curve, our path bends to the left.)

3. Since the orbits are regular, we can relate the winding rate $\overline{\alpha}(\epsilon, f; v_0, p_{v_0})$ to the fundamental periods of the tori, which we call $T_{u,v}(\epsilon, f; v_0, p_{v_0})$. The winding ratio of the points, defined as the ratio of the periods of u to v motion is:

$$\frac{T_u(\epsilon, f; v_0, p_{v_0})}{T_v(\epsilon, f; v_0, p_{v_0})} = \frac{\overline{\alpha}(\epsilon, f; v_0, p_{v_0}) - \pi}{\pi}. \tag{6.7}$$

In the numerator, we subtract π because the half-map incorporates a reflection $(v \to -v, p_v \to -p_v)$ which we regard as an advance of π upon each return. In the denominator, we divide by π instead of 2π because each return to $u = 0$ corresponds to a half-cycle of the u motion.

4. Besides the central periodic orbit, S_+, there are other periodic orbits corresponding to tori with rational period ratio. These occur when $(\overline{\alpha}(\epsilon, f, v_0, p_{v_0}) - \pi)/\pi$ is a rational fraction m/l. We name the torus and its periodic orbits by this rational fraction m/l. The periodic orbits of the map show up as intersection points of the spirals on the SOS (see Fig. 6.5).

5. As energy decreases, the winding rate $\overline{\alpha}(\epsilon, f; v_0, p_{v_0})$ around the center S_+ increases, and each rational torus moves outward from S_+.

6.4 A model of the half-map

In this section, we present a model Hamiltonian which generates a "twist map". This twist map is a simple model of the half-map, and we use this twist map to illustrate the sequence of bifurcations of closed orbits. We will show in the next section that the bifurcations of closed orbits in the crossed field system fall into the same sequence as the

bifurcations in the model. Hence the model Hamiltonian provides an interpretation of our calculations on the crossed-field system.

6.4.1 A model Hamiltonian

We consider a model in which a particle moves periodically on a single coordinate $q(t)$, with an associated canonical momentum $p(t)$, so phase space is the two-dimensional plane (q, p). We want a model having the following four properties: (1) the flow in phase-space is steady and area-preserving, so it is governed by a time-independent Hamiltonian; (2) the center $(q = 0, p = 0)$ is a fixed point, and there are no other fixed points; (3) points nearby move in a closed curve around the center with average angular velocity ω_0; (4) more distant points move around with a lower average angular velocity. At a later point we will add a fifth property: one of the closed curves defines an outer boundary to the flow.

A Hamiltonian generating such a flow is

$$H = (-\omega_0/a)e^{-aI} \tag{6.8}$$

where $I = (p^2 + q^2)/4\pi$ is the classical action. We may use I and $\theta = arctan(q/p)$ as canonical variables, and then

$$\dot{I} = 0, \quad I = const; \tag{6.9}$$

$$\dot{\theta} = \omega_0 e^{-aI}, \quad \theta(t) = \theta_0 + \omega_0 t e^{-aI}. \tag{6.10}$$

This is a continuous version of a "twist map" - the flow has the properties listed above. Obviously all the orbits are periodic, and any orbit that goes through some point q_0 returns repeatedly to that point (see Fig. 6.6).

In this model, we use the words "closed orbit" to refer to a "closed orbit at q_0 with closure time T": this is an orbit that starts at some location q_0 which is not at the center, and later, at $t = T$, returns to that same point. Let us now fix T, and regard ω_0 as a

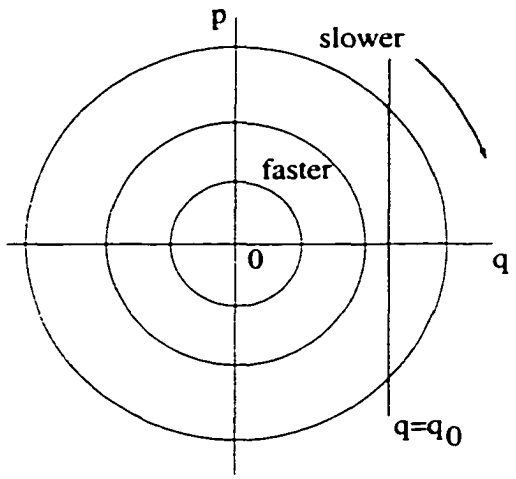

Figure 6.6: The motions described by the model Hamiltonian are circular rotations in the (q, p) phase space.

variable parameter. We will speak of "bifurcations of closed orbits". By this we mean that for some fixed q_0, and some fixed T, as we vary the parameter ω_0, there may be a creation or a splitting of a "closed orbit at q_0 with closure time T". For example, if T is fixed much less than $2\pi/\omega_0$, then there is no closed orbit moving around the center having such a short period. However, for that fixed T, we can increase ω_0 until it exceeds $2\pi/T$, and then such a closed orbit will appear.

This looks like a completely trivial problem. In fact, however, such closed orbits appear in groups of four in an orderly sequence. After we display this behavior, we will show that planar closed orbits in the crossed-field system appear in the same way.

6.4.2 Normal sequence of bifurcations of closed orbits of the model Hamiltonian

We consider the set of initial conditions ($q = q_0, p =$ anything). This corresponds to a vertical line in the (q, p) plane, which we call $\Gamma(0)$. Suppose we allow the points on that line to evolve under Hamiltonian's equations (6.9), (6.10) until $t = T$. The line evolves into a curve which we call $\Gamma(\omega_0 T)$. If the evolved curve $\Gamma(\omega_0 T)$ intersects the original line $\Gamma(0)$, then the intersection point is the final point of a "closed orbit with closure time T".

If we fix T and vary ω_0, then the evolved curve changes in some way; it may develop new or additional intersections with the original line. These are the above-mentioned "bifurcations of closed orbits of closure time T".

We need to know how the curve changes when ω_0 changes at fixed T. To understand this, we only have to look at Eq. (6.10) and note that ω_0 and t appear together as a product. Thus to learn how the curve changes with ω_0 at fixed t, we only have to ask, how does it evolve with t at fixed ω_0? This is shown in Fig. 6.7 for $\omega_0 = 0.5, a = -0.2, q_0 = 1$.

Every point moves clockwise on a circle, with points farther from the origin moving more slowly. Points at $p = \pm\infty$ do not move at all. Therefore, for small t, points on the lower half of the line sweep to the left, and points on the upper half of the line sweep to the right. It follows that there is just one intersection of the final curve with the initial line, and it lies in the lower-half-plane (LHP). At small T, there is always one orbit that moves slightly to the right of $q_0 = 1$ and then returns. We call it C_0. The zero in the subscript means that this orbit does not pass through the center $q = 0$.

As t increases (see Fig. 6.7), the curve $\Gamma(\omega_0 t)$ evolves until eventually the "nose" of the curve is tangent to the vertical line. A new closed orbit has appeared which we name C_1: this orbit moves to the left and then returns, passing back and forth through the center $q = 0$ once.

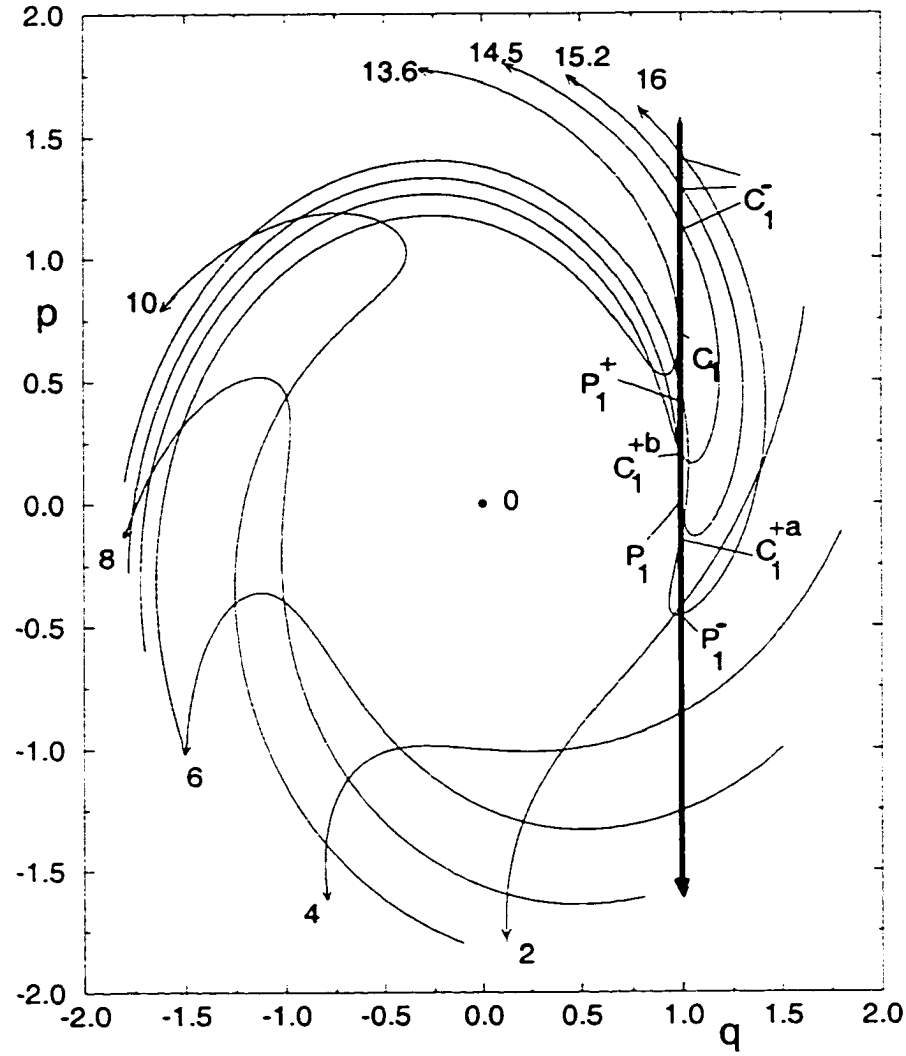

Figure 6.7: Evolution of the vertical line at different times t with $\omega_0 = 0.5$, $a = -0.2$. We label the curves by the time.

As t continues to increase, the "nose" passes through the vertical line. The one closed orbit has split into two. One moves up and one moves down the vertical line, and we call the resulting orbits C_1^- and C_1^{+b} (b stands for "before, for reasons we will see below). We may call this sequence of events a tangent bifurcation.

As t continues to increase, the final point of C_1^{+b} moves downward. To understand what happens next, consider the point $(q = q_0, p = 0)$. This is the point on the initial line which is closest to the origin, so this point moves around the origin with the highest angular frequency,

$$\omega_1 = \omega_0 exp(-aq_0^2/4\pi).$$

When $t = 2\pi/\omega_1$, that point has returned to itself, and we have a periodic orbit. We can also see that the final point of C_1^{+b} has moved down so that it coincides with this periodic orbit, and the formerly closed orbit C_1^{+b} has evolved into a periodic orbit. We may now call it P_1. The subscript means that this periodic orbit has gone around the center $(q = 0)$ once.

At this point, the evolved curve $\Gamma(2\pi\omega_0/\omega_1)$ is again tangent to the original line $q_0 = 1$ at $p = 0$. As t continues to increase, the part in the LHP moves to the left and the part in the upper half plane (UHP) moves to the right. It follows that the point of intersection with $\Gamma(0)$ moves down, and two new intersection points appear, one in the UHP and one in the LHP. The original intersection point is the continuation of C_1^{+b}, it is still closed but not periodic, and we call it C_1^{+a} (a representing "after"). The two new intersection points are periodic orbits; they both lie on the same circle, and the same straight line, i.e. they are reflections of each other through the $p = 0$ axis. The creation of these two orbits may be called a "pitchfork" bifurcation.

Reiterating the sequence of events, a closed orbit C_1 appears which splits into two C_1^- and C_1^{+b}. C_1^- persists as a closed orbit. C_1^{+b} becomes periodic (and we call it P_1), then

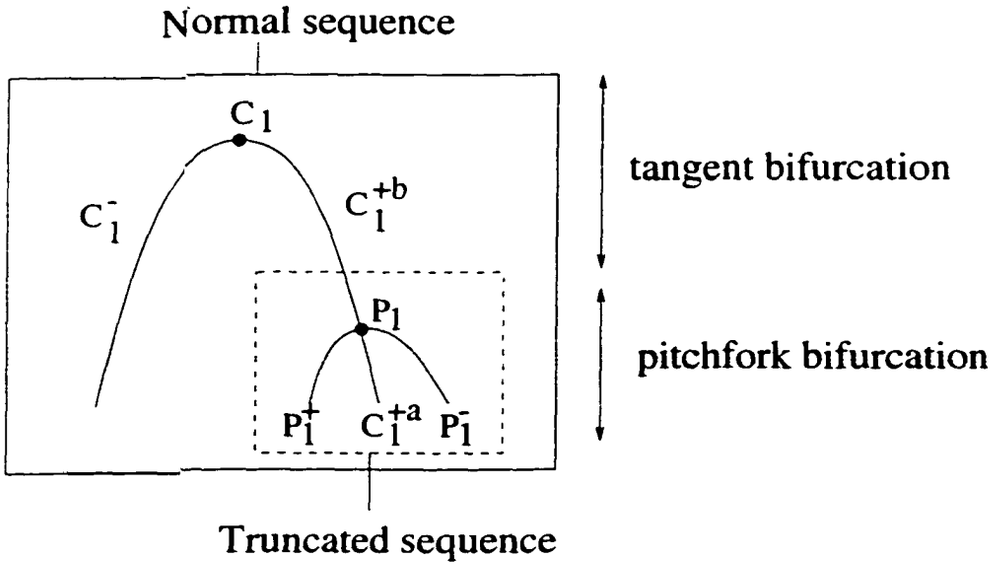

Figure 6.8: The normal sequence of bifurcations: a tangent bifurcation is followed by a pitchfork bifurcation. In the truncated sequence, the tangent bifurcation is not present.

it splits off two periodic orbits P_1^+ and P_1^-, after which it is again closed but not periodic (C_1^{+a}). Four closed orbits survive, two of which are periodic (P_1^+, P_1^-), and two of which are not (C_1^-, C_1^{+a}). A picture is given in Fig. 6.8.

6.4.3 The bifurcation sequences of longer trajectories

If we iterate the vertical line for a longer time, the curve $\Gamma(\omega_0 t)$ curls around the center a second time. Another sequence of bifurcations occurs and creates closed orbits: $C_2 \to (C_2^-, C_2^{+b})$, $C_2^{+b} \to P_2 \to (P_2^+, C_2^{+a}, P_2^-)$. These orbits pass back and forth the center twice (P_2 executes two full circles around the center).

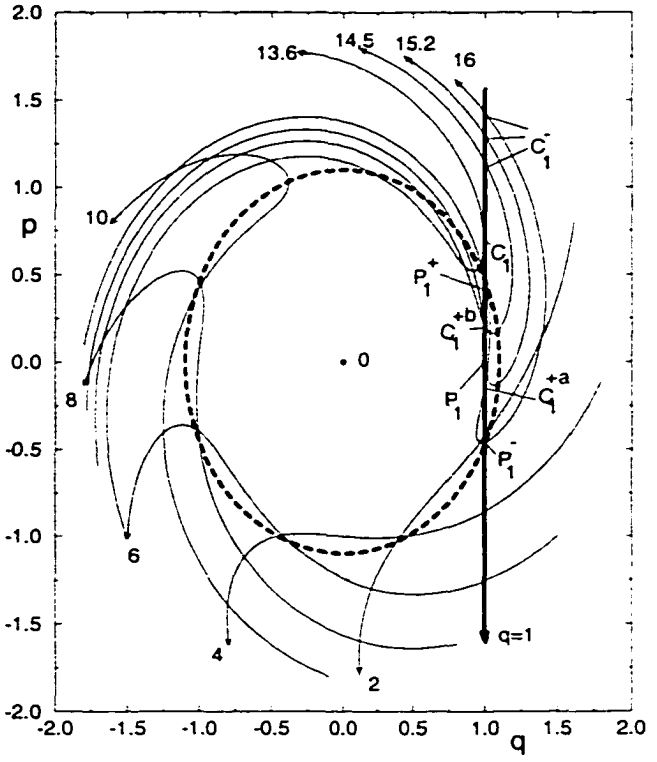

Figure 6.9: The iterations of the vertical line at different time t with $\omega_0 = 0.5$, $b = 0.2$. We label the curves by the iteration time. The dashed line is the forced boundary and the particle is only allowed to move in the inner region.

6.4.4 Truncated sequence of bifurcations of closed orbits of the model Hamiltonian

To understand the observed "truncated sequence" of bifurcations of closed orbits, we add one more element to our model: an outer boundary. Suppose the allowed region of phase space is bounded by a circle (see the dashed circle in Fig. 6.9), and the radius of this circle is too small to include the orbit C_1. Then bifurcation sequence starts from an existing closed orbit C_1^{+b}. As energy increases, C_1^{+b} first evolves into a periodic orbit, then splits into two periodic orbits and a closed orbit by the pitchfork bifurcation already discussed.

The result is that three closed orbits are created in an orderly sequence of events:

C_1^{+a}, P_1^+ and P_1^-. The closed orbit C_1^- is missing. This event of a pitchfork bifurcation without a nearby tangent bifurcation we may call the "truncated sequence of bifurcations of closed orbits in the model system".

6.4.5 Bifurcation sequence of closed orbits at fixed t and varying ω_0

We have discussed above the bifurcation sequences of the closed orbits at fixed ω_0 and varying t. Since t and ω_0 are interchangeable in (6.10), fixing t and varying ω_0 is equivalent to fixing ω_0 and varying t. Therefore, the bifurcation sequences we discussed above also happen as we fix t and vary ω_0. The pitchfork bifurcation for the closed orbits which pass the origin back and forth n times happens when $\omega_0 > 2\pi/T$ and $\omega_n = \omega_0 e^{-aq_0^2/4\pi} = 2\pi n/T$, where ω_n is the winding rate of the point $(q = q_0, p = 0)$.

6.4.6 Local bifurcations *vs.* regional sequences of bifurcations

Mathematical bifurcation theory is focused on "local" properties of bifurcations. The theorems describe what happens within an arbitrarily small neighborhood of a point in phase space in an arbitrarily small region of parameter space. From this perspective, the above described tangent bifurcation and pitchfork bifurcation are independent events which have no relationship to each other. Indeed, from the mathematical perspective the pitchfork bifurcation is considered exceptional ("non-generic").

A physicist's perspective is different. We see that for logical reasons we find a tangent bifurcation and a pitchfork bifurcation in a logical sequence, but not within an arbitrarily small neighborhood. Accordingly, to distinguish this behavior from the local properties of each bifurcation, we will call the pair of bifurcations a regional sequence. Implicit in this discussion is the view that in systems of interest in physics, this connected pair of bifurcations will commonly be found.

On a larger scale in parameter space, one regional bifurcation sequence may be connected with another; we call these "large-scale connections". If one were ever to work out the whole family of closed orbits and their bifurcations in all of phase space and/or all of parameter space, we would have a "global" picture.

In the crossed-field system, we will examine several regional sequences of bifurcations, and a few large-scale connections.

6.5 Local bifurcations and regional sequences of bifurcations in crossed field system

Now we return to the crossed-field system, and we show that what we learned about the model also applies to our real system.

From the above, we see that both the "normal" and "truncated" bifurcation sequences have periodic orbits involved, that is to say, this means that the bifurcation sequence includes the passage of a rational torus through the line of initial conditions. Therefore, in this section, we first give a review of the evolution of rational tori; then we discuss the bifurcations of the closed orbits. In this section, we focus on local bifurcations and regional sequences of bifurcations.

6.5.1 Creation and evolution of rational tori

In Fig. 6.10, we show the evolution of the rational torus 2/3 on both (u, p_u) and (v, p_v) surfaces. On the (v, p_v) plane, the winding ratio decreases with increasing distance from the center S_+, and as energy decreases, the winding ratio around the center S_+ increases. It follows that as energy decreases, the rational torus 2/3 moves outward. At some critical energy, it becomes tangent to the p_v axis. (See curve 2 in (a).) This indicates that

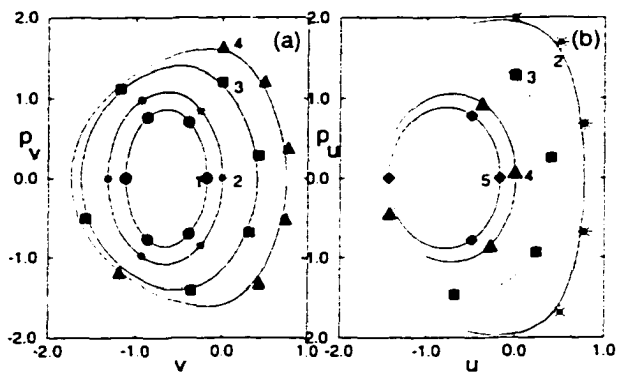

Figure 6.10: The 2/3 rational torus in (v, p_v) and (u, p_u) planes at different energies. In (a), from inner to outer (curve 1 to curve 4), energy decreases and the energies are $70cm^{-1}, 95.3cm^{-1}, 160cm^{-1}$ and $212cm^{-1}$; in (b), from outer to inner (curve 2 to curve 5), energy decreases and the energies are $95.3cm^{-1}, 160cm^{-1}, 212cm^{-1}$ and $230cm^{-1}$.

one of the members on this rational torus passes through the origin and becomes a periodic orbit closed at the origin. We call the energy at which the rational torus m/n is tangent to the p_v axis, $E^+_{m/n}$. When energy continues to decrease, the rational torus 2/3 continues to expand so that it crosses the p_v axis, and two different periodic closed orbits are created. As energy further decreases, at some critical energy, it touches the classical boundary in the (v, p_v) plane, and then it disappears from this plane. We call the critical energy at which rational torus m/n disappears from this plane, $E^-_{m/n}$. To see what is happening there, it is better to look at the other SOS (u, p_u).

On the (u, p_u) plane, the winding ratio increases with increasing distance from the center S_- and as energy increases, the winding ratio around the center S_- decreases. When energy is higher than $E^+_{2/3}$, the rational torus 2/3 does not appear on the (u, p_u) surface. At $E = E^+_{2/3}$, it appears at the boundary. After that, as energy decreases, it moves toward the center S_-. The two crossings of the rational torus on the p_u axis indicate again that two members of the periodic family 2/3 are closed at the origin. At $E = E^-_{2/3}$, the rational torus 2/3 becomes tangent to the p_u axis, and two periodic closed members merge to one

periodic closed member. As energy goes below $E = E^-_{2/3}$, the rational torus moves away from the p_u axis and toward the center S_-. (See curve 5 in (b).) Finally it disappears at the center S_-.

Based on the evolution of the rational torus 2/3, we can reiterate the evolution of a general rational torus m/n. At some high energy, rational torus m/n is created at S_+, and as energy decreases, it moves away from S_+. At $E = E^+_{m/n}$, it becomes tangent to the p_v axis and one periodic closed orbit is created: at that point it also becomes visible in the other SOS. As energy continues to decrease, this rational torus crosses the momentum axes on either SOS, and two members of the periodic family m/n are closed at the origin. At $E = E^-_{m/n}$, the rational torus becomes tangent to p_u axis and two periodic closed members merge to one periodic closed member. As energy further decreases, the rational torus moves away from the p_u axis and toward S_-; it has then disappeared from the (v, p_v) plane. Finally this rational torus is annihilated at S_-. Later we will use the name of the rational tori (m/n) to name a closed family such as $C^{+a}_{2,3}$ where the family name $(2, 3)$ is related to the winding ratio $(2/3)$ of the periodic members in the family.

6.5.2 The sequence of the bifurcation patterns of closed orbits

The evolution of the rational torus shows that the bifurcations of the periodic closed orbits m/n happen at $E^+_{m/n}$ and $E^-_{m/n}$. In this section, we show that both bifurcation sequences illustrated by model Hamiltonian happen in a crossed-field system: we have observed some normal sequences by iterating the p_v axis in the (v, p_v) plane near $E^+_{m/n}$ and we have observed some truncated sequences by iterating the p_u axis in the (u, p_u) plane near $E^-_{m/n}$.

- **"normal" bifurcation sequences**

The 2/3 bifurcation is observed in the sixth iterate of the half-map in the (p_v, v) plane. The starting points lie on the p_v axis. Fig. 6.5 shows that $E^+_{2/3} \approx -95cm^{-1}$. We iterate the p_v axis on the $u = 0$ surface over the energy range $-50cm^{-1}$ to $-105cm^{-1}$ to observe the 2/3 "normal" bifurcation sequence. The result is shown in Fig. 6.11. When energy is below $60.5cm^{-1}$, the sixth iteration does not touch the momentum axis. At the energy $E = 60.5cm^{-1}$, it is tangent to the p_v axis and one closed orbit $C_{2,3}$ is created (see (a)). As we continue to decrease the energy, the sixth iteration crosses the p_v axis, and the closed orbit $C_{2,3}$ splits into two closed orbits $C^{+b}_{2,3}$ and $C^-_{2,3}$ (see (b)). This sequence of events is the tangent bifurcation defined in section 6.4.2. Then the closed orbit $C^{+b}_{2,3}$ moves toward the origin and becomes a periodic orbit $P_{2,3}$ at the critical energy ($E^+_{2/3} = -95.3cm^{-1}$) of the 2/3 rational torus. As the energy passes and goes below the $E^+_{2/3}$, the closed orbit $C^{+b}_{2,3}$ evolves into closed orbit $C^{+a}_{2,3}$ and two periodic orbits ($P^+_{2,3}, P^-_{2,3}$) are created. The creation of these two periodic orbits is the "pitchfork bifurcation" defined in section 6.4.2.

Fig. 6.12 shows the normal bifurcation sequence of the $(5, 7)$ family of orbits, which appears on the seventh iterate of the half-map near $E^+_{5/7} = -135cm^{-1}$. Since it is an odd number iteration, the periodic orbits involved in this bifurcation sequence are periodic orbits of the half Poincaré map and each of them is half of a periodic orbit of the dynamical system.

These bifurcation sequences are the "normal" bifurcation sequence in which the closed orbits are created in a group of four: $C^-_{m,n}$, $C^{+a}_{m,n}$, $P^+_{m,n}$ and $P^-_{m,n}$. Here (m, n) means that periodic members have a rational winding ratio m/n.

- **"Truncated" bifurcation sequence**

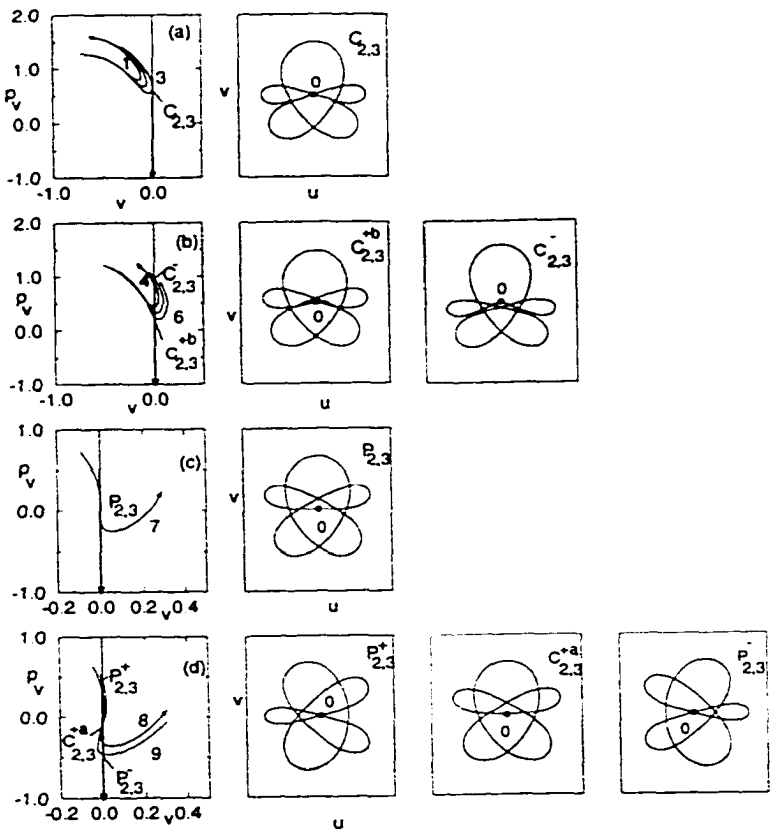

Figure 6.11: The sixth iteration of the bold vertical arrow line with external fields $B = 6T$ and $E = 1000V/cm$ at various energies: (a) $E = -50, -55, -60.5(cm^{-1})$ from 1 to 3; (b) $E = -65, -70, -75(cm^{-1})$ from 4 to 6; (c) $E = -95.3(cm^{-1})$ labeled 7; (d) $E = -100, -105(cm^{-1})$ from 8 to 9.

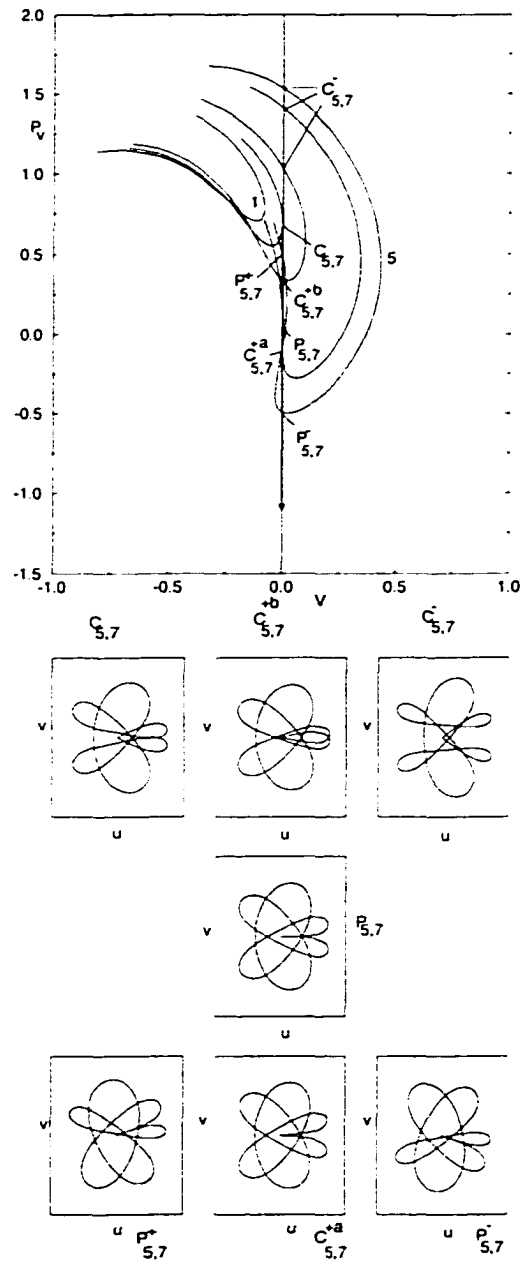

Figure 6.12: The seventh iteration of the bold vertical arrow line with external fields $B = 6T$ and $E = 1000V/cm$ at various energies: $E = -95, -101.5, -110, -135, -145(cm^{-1})$ from 1 to 5

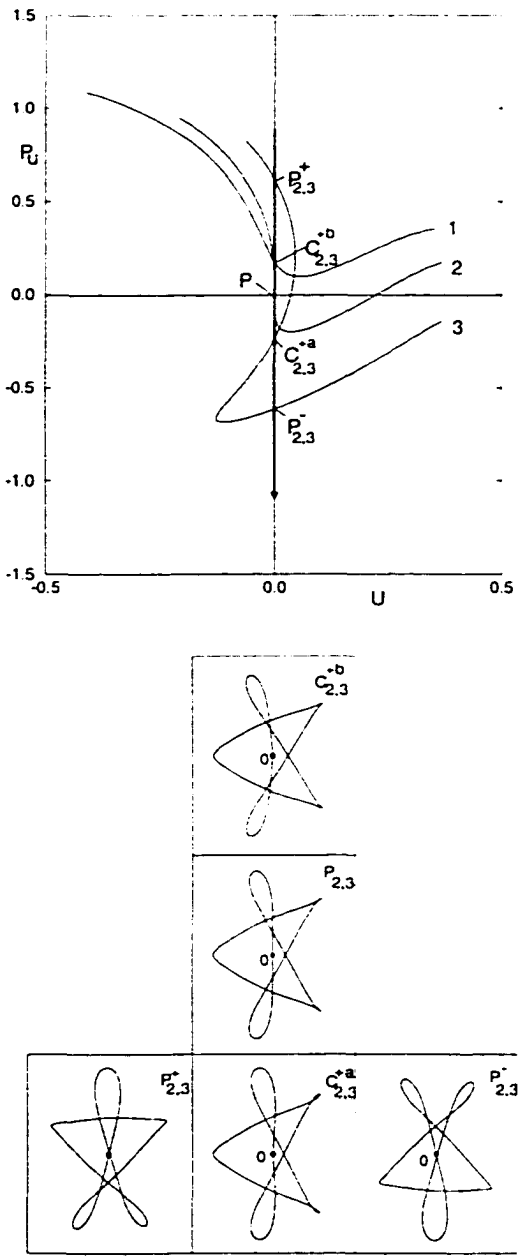

Figure 6.13: The fourth iteration of the bold vertical arrow line with external fields $B = 6T$ and $E = 1000V/cm$ at various energies: $E = -220, -212, -200(cm^{-1})$ from 1 to 3.

The truncated 2/3 bifurcation sequence is observed by the fourth iterate of the half-map on the (u, p_u) plane. $E^-_{2/3} \approx -212cm^{-1}$; i.e. as we go to energy lower than $E^-_{2/3}$, $P_{2,3}$ is destroyed. Therefore we start from below and increase E to observe the creation of the closed orbits. Fig. 6.13 shows the fourth iteration of the momentum axis. Curve 1 corresponds to $E = -220cm^{-1}$. It crosses the momentum axis once, but in contrast to curve 1 in Fig. 6.11, it does not curve back and cross the momentum axis a second time. Hence there is one closed orbit $C^{+b}_{2,3}$ and this closed orbit moves toward the origin as energy increases. At $E = E^-_{2/3}$, $C^{+b}_{2,3}$ becomes a periodic orbit $P_{2,3}$. Then the periodic orbit bifurcates into one closed orbit $C^{+a}_{2,3}$ and two periodic orbits $(P^+_{2,3}, P^-_{2,3})$ as energy goes above $E^-_{2/3}$. In this truncated bifurcation sequence, a group of three closed orbits $C^{+a}_{2,3}, P^+_{2,3}$ and $P^-_{2,3}$ are created in an orderly sequence.

Fig. 6.14 gives another example of the "truncated" bifurcation sequence. This sequence involves the 3/5 rational torus and shows the same pattern as Fig. 6.13.

Hence we observe that both "normal" and "truncated" bifurcation sequences appear in the crossed field system. The "normal" bifurcation sequence involves the bifurcation of a periodic closed orbit at $E^+_{m/n}$, and the "truncated" bifurcation sequence involves the bifurcation of a periodic closed orbit at $E^-_{m/n}$.

6.6 Some large scale connections of regional bifurcations

In the local and regional bifurcations, we observed the creation of the closed orbits $C^-_{m,n}, C^{+a}_{m,n}, P^+_{m,n}, P^-_{m,n}$. Now we ask what happens after they are created. To answer this question, we studied the evolution of the closed orbits after their creation and found that one closed orbit created in one regional bifurcation sequence may evolve and get involved in another regional bifurcation sequence. Hence the regional bifurcation sequences are

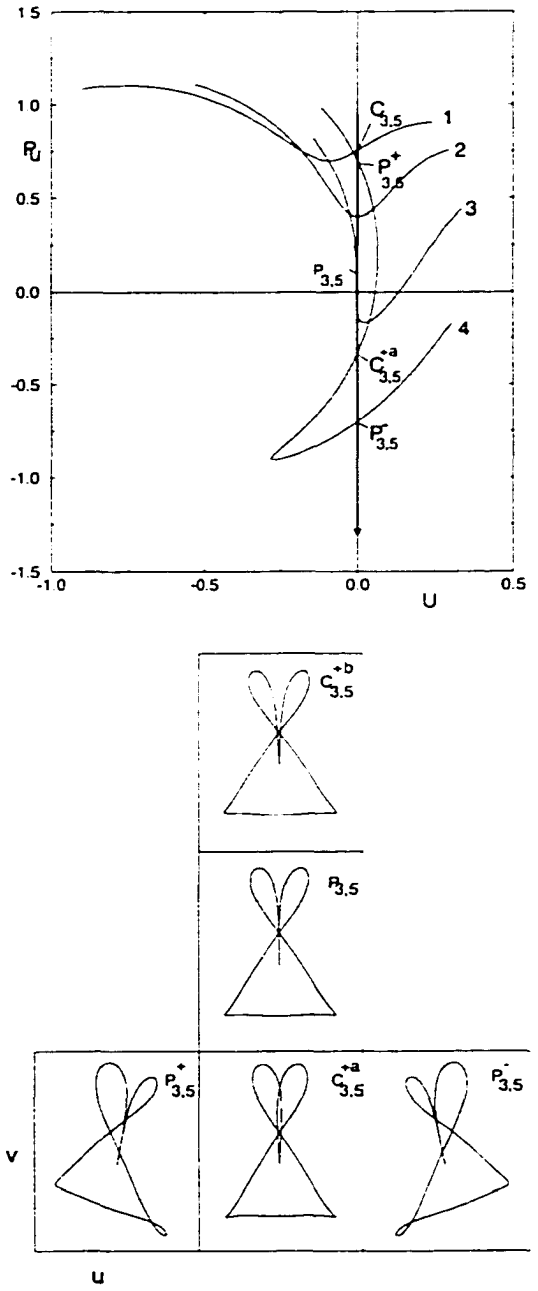

Figure 6.14: The third iteration of the bold vertical arrow line with external fields $B = 6T$ and $E = 1000V/cm$ at various energies: $E = -210, -200, -186, -170(cm^{-1})$ from 1 to 4.

connected with each other. We call a bifurcation sequence which includes more than one regional bifurcation sequences a large scale connection of regional bifurcations. We found that some of the large scale connections are related to the symmetry of the regularized Hamiltonian. In this section, we first review the symmetries of the regularized Hamiltonian, then present some of the large scale connections we observed.

6.6.1 The symmetry properties of the regularized two-dimensional Hamiltonian

The Hamiltonian in (6.1) is invariant with regard to three symmetry operations $(\sigma_u\sigma_v, T\sigma_u, T\sigma_v)$ where σ_u, σ_v and T operations are defined as:

- σ_u, a reflection with respect to v axis, that is, $(u, v, p_u, p_v, t) \rightarrow (-u, v, -p_u, p_v, t)$;
- σ_v, a reflection with respect to u axis, that is, $(u, v, p_u, p_v, t) \rightarrow (u, -v, p_u, -p_v, t)$;
- T, a time reversal, that is, $(u, v, p_u, p_v, t) \rightarrow (u, v, -p_u, -p_v, -t)$.

Therefore, three symmetrical operations are:

- $\sigma_u\sigma_v$, a combination of reflection with respect to v axis and reflection with respect to u axis, that is, $(u, v, p_u, p_v, t) \rightarrow (-u, -v, -p_u, -p_v, t)$;
- $T\sigma_u$ is a combination of time reversal and reflection with respect to v axis, that is, $(u, v, p_u, p_v, t) \rightarrow (-u, v, p_u, -p_v, -t)$;
- $T\sigma_v$ is a combination of time reversal and reflection with respect to u axis, that is, $(u, v, p_u, p_v, t) \rightarrow (u, -v, -p_u, p_v, -t)$.

Therefore a closed orbit which does not have any symmetry must have three siblings which result from these three symmetry operations.

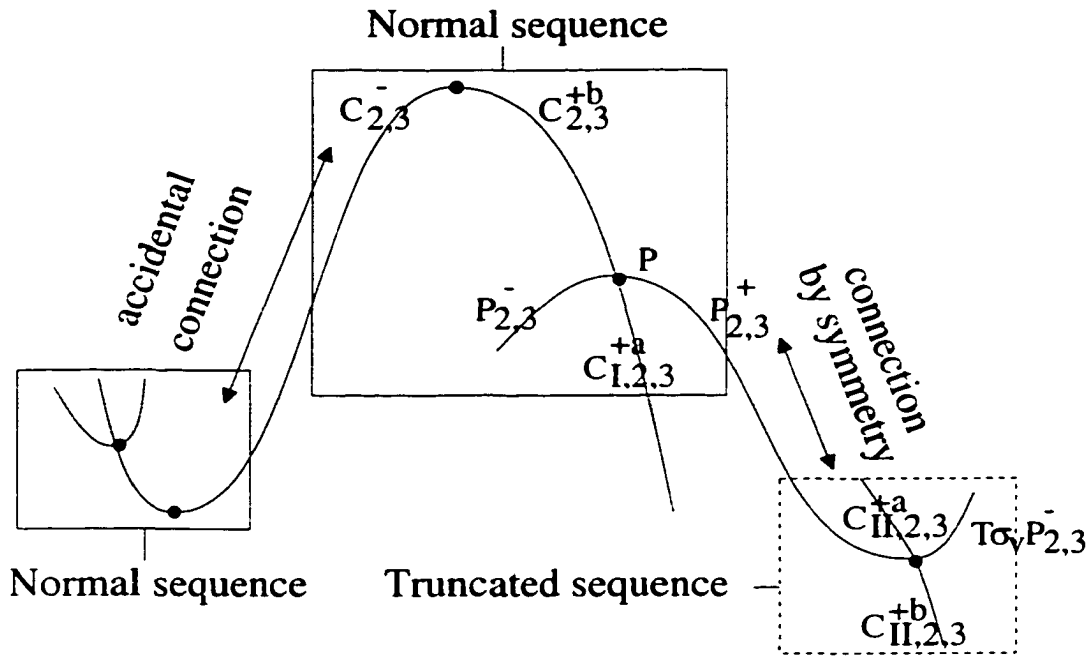

Figure 6.15: We show large scale connections of two normal regional bifurcation sequences and one truncated regional bifurcation sequence. The central normal sequence is connected to the left normal sequence by accidental connection and is connected to the truncated sequence by symmetry. The orbits involved in the large scale connection by symmetry are shown in Fig. 6.17.

6.6.2 Some of the large scale connections of regional bifurcations

In Fig. 6.15, we show the large scale connections of three regional bifurcation sequences. When we follow the orbits in the $(2,3)$ family to lower energies, we find that $P^{+}_{2,3}$ is connected to a truncated sequence of bifurcations. A different closed orbit is involved in this bifurcation, so we now need to add another label to the closed orbits: we call them $C^{+a}_{I,2,3}$ and $C^{+a}_{II,2,3}$. In these two regional bifurcation sequences the periodic orbits are all related by symmetry. We can call this a "connection by symmetry". We show the orbits involved in this connection in Fig. 6.17. Furthermore in Fig. 6.16, we show a whole unit of connections by symmetry and label periodic orbits by symmetry operator and periodic

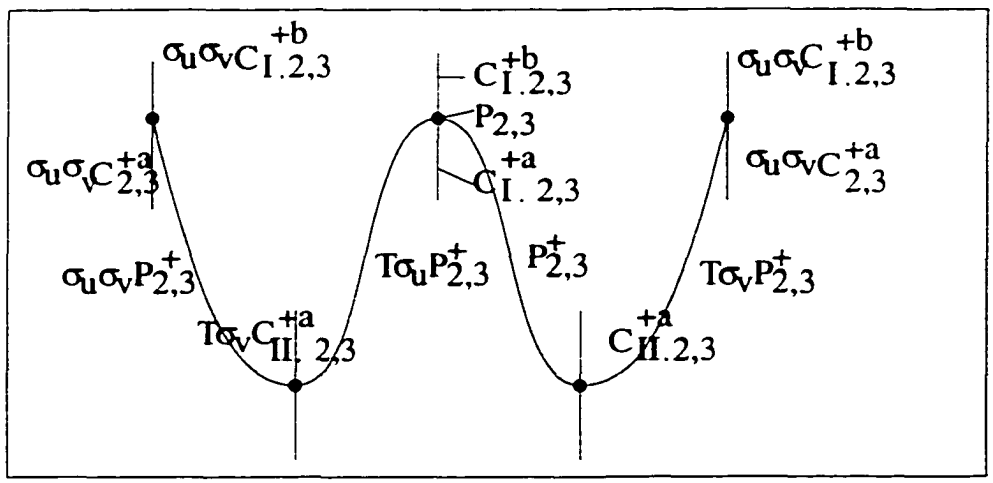

Figure 6.16: We show a unit of symmetry-related large scale connections. All of the periodic closed orbits in the three normal sequences are connected to $P^{+}_{2,3}$ by symmetry operations and the closed and nonperiodic orbits are connected to $C^{+b,a}_{I,2,3}$ and $C^{+b,a}_{I,2,3}$ by symmetry operations.

orbit $P^{+}_{2,3}$ to explicitly indicate the symmetrical relations.

We also find that $C^{-}_{2,3}$ is connected to another normal sequence of bifurcations. We call this "accidental connection" since none of the trajectories in the other sequence is connected to the trajectories in $(2,3)$ sequence by three symmetry operations.

6.7 The organization of the closed orbits

In this section, We classify the closed orbits into families. Each family has a family name and each member is named by a given name plus its family name.

- Family and the name of the family: we classify the closed orbits which are involved in the same regional sequence of bifurcations as a family. Among each family, there are some periodic members and they have a rational fraction winding ratio m/l. We

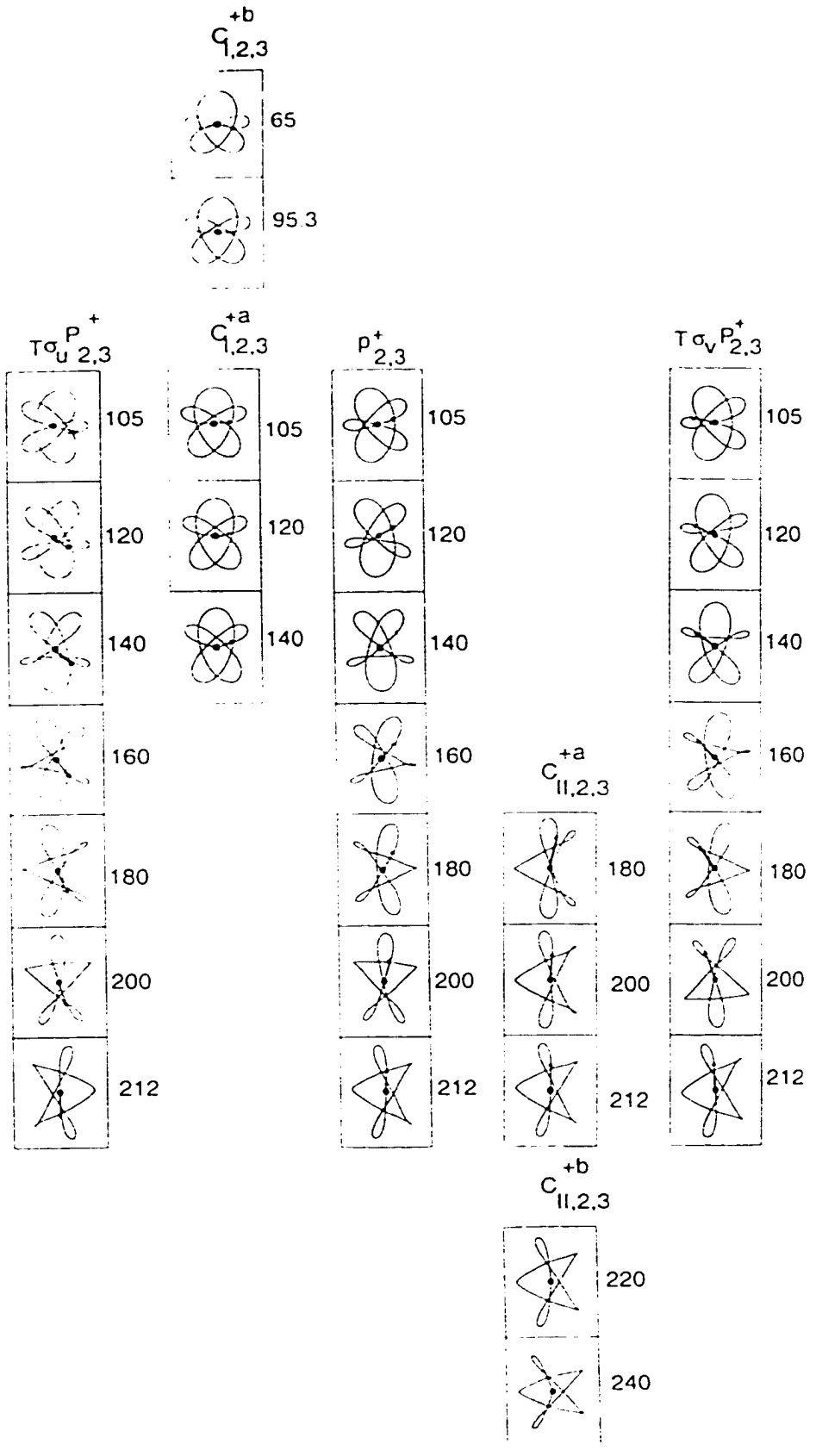

Figure 6.17: We show the orbits which are involved in the large scale connection by symmetry in Fig. 6.15. From top to bottom, energy decreases, and the number beside each trajectory is minus the energy in units of cm^{-1}.

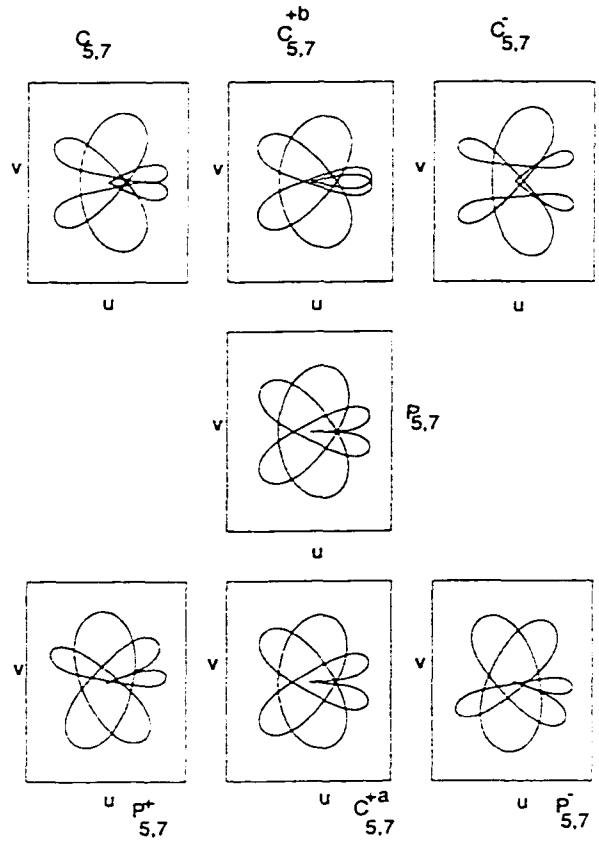

Figure 6.18: The 5/7 closed family.

use m/l to name the family. Fig. 6.18 shows the family (5, 7). This classification only applies locally. The large scale connections of regional bifurcations tell us that the closed orbits may evolve into another family.

- Given names of the family members: we use P to label periodic closed orbits and C to label nonperiodic closed orbits. Then we use a and b to distinguish the closed orbits which are created at different times. For example, C^{+b} and C^{+a} means that the closed orbit is created before or after the pitchfork bifurcation. Also we use $+$ and $-$ to distinguish the closed orbits created at the same time. For example, C^{-} and C^{+b} are created at the same time, $+/-$ indicate bigger and smaller winding ratios respectively. But for the periodic orbit P^{+} and P^{-}, they have the same winding ratio,

then $+/-$ indicate that the momentum of the periodic orbit at the origin is positive /negative. The closed orbit first created is labeled as C. Then we use subscript (m,n) to notate the family name.

6.8 summary

In this chapter, we studied the local and regional sequence of the bifurcations of the closed orbits and created a model Hamiltonian to interpret it. We also presented some of the large scale connections of the regional sequences. We classified the closed orbits into different families according to the regional bifurcation sequences. The family members are born in a regional bifurcation sequence drawn in Fig. 6.8. We used the rational winding ratio of the periodic member as the family name and assigned each member a given name.

Chapter 7

Summary and open problems

We have interpreted the measured absorption spectrum of the hydrogen atom in crossed electric and magnetic fields in the following respects:

- The large scale structure in the absorption spectrum:

  We modified closed orbit theory from two-dimensions to three-dimensions and we applied it to calculate the absorption spectrum of the crossed field system. We also developed a computational method – Chirped-Fourier-Transform. This computational method allows us to extract the closed orbits from an unscaled spectrum. We proved that the large scale structure in the absorption spectrum is correlated with short closed orbits.

- The continuum absorption:

  The lower envelope of the absorption spectrum is called continuum absorption. We provided a quantitative model to calculate both the threshold and the intensity of continuum absorption.

- The regular quasidicrete states:

  We applied EBK quantization theory to quantize three dimensional tori and proved that the regular quasidiscrete states correspond to appropriately quantized regular tori.

In addition, we carried out a theoretical study of the bifurcation patterns of the planar closed orbits. We found an ordered sequence of bifurcation patterns.

What we have done is only one step toward understanding the crossed field system. Following are some of the remaining problems of future research:

- The "prompt" and "delayed" signals:

  The measurements done by Bielefeld group in Germany distinguishes the long-lived and short-lived states. The states with lifetime less than $120ns$ belong to the "prompt" signal and the states with lifetime greater than $120ns$ belong to the "delayed" signal. We have not interpreted them yet in this thesis.

- The fractal structures of the lifetimes:

  Our calculated lifetimes of the electrons as a function of the ejection angles show fractal structures. The understanding of the fractal structure may provide a way to predict the lifetimes of the states, then the measured "prompt" and "delayed" signals may be understood.

- The bifurcation patterns of the spatial closed orbits:

  To visualize the creation of the spatial closed orbits, we should reduce the dimension of the spatial closed orbits. One possible way is to find an approximate conservation law. Cushman and Sadovskii [36], and Milczewski and Uzer [38] have made some progress in finding the approximate conservation laws, but those conservation laws have not been used to help locate the closed orbits. In addition, Raković and Chu [37] discovered an

integrable Hamiltonian system which is similar to the hydrogenic crossed-field system, but which possesses a full set of conservation laws. This is a stimulating discovery, but since the hydrogen atom undergoes chaotic ionization, it is unclear how helpful this new integrable model can be.

Appendix A

Another application of The Chirped-Fourier-Transform

As was stated earlier, for an atom in crossed fields, spectra can be measured by the scaled-variables method. When it is possible, scaled-variable spectroscopy is a more effective way of extracting recurrences than the Chirped-Fourier-Transform. However, for most systems, scaled-variable spectroscopy is impossible. We present here a recurrence spectrum for a model coupled-oscillator system, calculated by using the Chirped-Fourier-Transform.

The Hamiltonian is similar to that of the Henon-Heiles system, but with unequal force-constants.

$$H = \frac{1}{2}(p_1^2 + p_2^2 + \omega_1^2 q_1^2 + \omega_2^2 q_2^2) + \lambda q_2 (q_1^2 + \eta q_2^2) \qquad (A.1)$$

with $\omega_1 = 1.3$, $\omega_2 = 0.7$, $\lambda = -0.1$, $\eta = 0.1$. The quantum energy spectrum calculated by Don Noid [21] with a 30 x 30 (900 functions) harmonic oscillator basis set is shown in Fig.

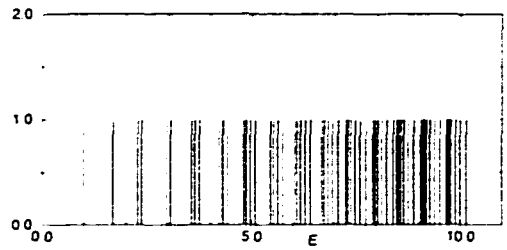

Figure A.1: Energy spectrum of the model Hamiltonian (A.1). Units are not defined for this model.

A.1. The formula for the quantum density of states is:

$$\rho(E) = \sum_i \delta(E - E_i).$$

We apply the Chirped-Fourier-Transform defined by Eq. (3.60) to this density of states

$$\begin{aligned} \tilde{\rho}(T) &= \int e^{-i[T(E-E_0)+\alpha(E-E_0)^2]}\rho(E)dE \\ &= \sum_i e^{-i[T(E_i-E_0)+\alpha(E_i-E_0)^2]} \end{aligned} \tag{A.2}$$

where α is a parameter.

We evaluate $|\tilde{\rho}(T;\alpha)|^2$ *vs.* T with α ranging from 0 to 1.1 in steps of 0.1. The results are shown in Fig. A.2(B). We notice that the peak at $T/2\pi = 1.5$ is very significant in Fig. A.2(0.0)—(0.4). In Fig. A.2(0.5), (0.6), (0.9),(1.1) we see sharp, well-resolved peaks at $T/2\pi = 1.48, 5.95, 7.40, 8.99$ and 10.56 respectively. From a numerical search for periodic orbits, we identify these peaks with various orbits of the system. For example, the peak labeled b corresponds to the periodic orbit b. The period of this orbit is nearly constant over the whole energy range, so we can extract it by ordinary Fourier-Transform (Fig. A.2(0.0)).

In contrast, the peak a at $T/2\pi = 0.75$ corresponding to periodic orbit a is very weak. The peaks labeled c, d, e, f correspond to the periodic orbit c, d, e, f shown right below the recurrence spectra in Fig.14. The theoretical α values for the periodic orbits are

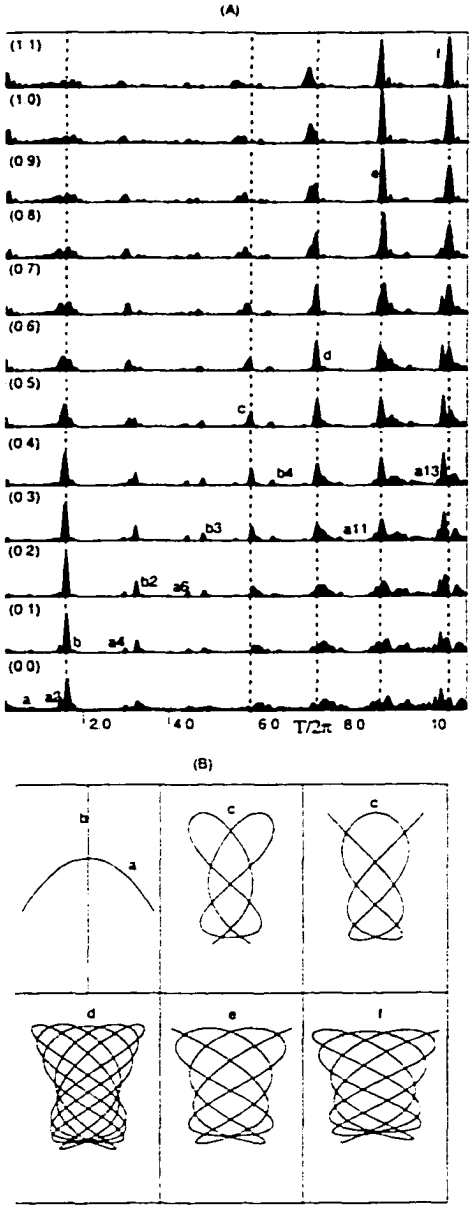

Figure A.2: (A) Chirped-Fourier-Transform of quantum energy spectrum given in Fig. A.1. From bottom up, we input the alpha values from 0.0 to 1.1 in steps of 0.1. a, b, c, d , e, f label the peaks which correspond to periodic orbits a, b, c, d, e, f which are shown in (B). ai(i=2,4,6,11,13) labels the peak which corresponds to the ith return of the periodic orbit a; bi(i=2,3,4) labels the peak which corresponds to the ith return of the periodic orbit b.

0.03, 0.07, 0.55, 0.64, 0.87, 1.02 sequentially. These values are consistent with the values shown in Fig. A.2.(0.1),(0.5),(0.6), (0.9) and (1.1) within ±8%.

In addition, the short and wide peaks a2, a4, a6, a11, a13 are second, fourth, sixth, eleventh and thirteenth repetitions of the periodic orbit a and peaks b2, b3, b4 are second, third and fourth repetitions of periodic orbit b.

In cases like this, the method of scaled-variable spectroscopy is impossible. We see that the CFT extracts strong, narrow, isolated peaks where the ordinary Fourier transform gives no signal. Therefore we expect that the CFT will be a valuable tool for the study of periodic orbits and recurrences.

Appendix B

Closed orbit theory

In this appendix, we derive the formula for the absorption spectrum of hydrogen atoms in crossed electric and magnetic fields and discuss the implementation of the closed orbit theory.

Since this derivation closely follows the method used in [1], we only provide the main formula which are used and different from [1] to avoid duplication.

B.1 The derivation of the closed orbit theory of the crossed field system

The observed absorption spectrum (rate of absorption of photons or rate of production of excited atoms or ions) is proportional to the oscillator strength density $Df(E)$, therefore, we focus on the derivation of the oscillator strength density. It has been shown by Du and Delos [1] that the oscillator-strength density can be expressed as

$$Df(E) = -\frac{2(E - E_i)}{\pi} Im < \psi_i D|G^+|D\psi_i > . \tag{B.1}$$

We have

$$Df(E) = -\frac{2(E_f - E_i)}{\pi} Im < \psi_i D|G^+_{dir} + G^+_{ret}|D\psi_i >, \tag{B.2}$$

where G^+_{dir} and G^+_{ret} have the same physical meaning as that in [1].

Two approximations have been made: (1) In the inner region ($r \leq 50a_0$), effects of external fields are negligible, and the waves are taken as pure Coulomb waves; (2) In the outer region ($r \geq 50a_0$) , the wavelength is short compared to the range over which the potential energy changes and a semiclassical approximation is applied to the wave function.

Based on the first approximation, we can write down G^+_{dir} immediately:

$$G^+_{dir}(q, q'; E = 0) = G^+_c(q, q': E = 0) = \sum_{l,m} Y^*_{lm}(\theta', \phi') g^0_l(r, r') Y_{lm'}(\theta, \phi) \tag{B.3}$$

with $g^0_l(r, r') = -2\pi i \frac{J_{2l+1}(\sqrt{8r'}) H^{(1)}_{2l+1}(\sqrt{8r})}{\sqrt{rr'}}$. With the asymptotic approximation for the outgoing Hankel function which is given by

$$H^{(1)}_\nu(z) \sim \sqrt{\frac{2}{\pi z}} exp[i(z - \frac{1}{2}\nu\pi - \frac{\pi}{4})], \; z \to \infty$$

we obtain

$$G^+_{dir}(q, q'; E = 0) \sim -i\pi^{1/2} 2^{3/4} e^{i\sqrt{8r}}/r^{3/4} \sum_{lm} Y^*_{lm}(\theta', \phi') Y_{lm}(\theta, \phi) \frac{J_{2l+1}(\sqrt{8r'})}{\sqrt{r'}} e^{-i(l+3/4)\pi}. \tag{B.4}$$

The returning Green function G^+_{ret} is gotten by following five steps:

1. In the inner region, the direct Green function produces an outgoing wave and the outgoing waves are given by

$$\psi_{out}(q) = \int G^+_{dir}(q, q'; E) D(q') \psi_i(q') dq' \tag{B.5}$$

with G^+_{dir} given by Eq. (B.4) and $D(q')\psi_i(q')$ the same as Eq. (4.3) in [1]b.

2. In the outer region, according to the semiclassical approximation, the wave function is given by

$$\psi_{semi}(q) = \sum_j \psi_{out}(q^\circ) A_j(q) e^{i(S_j(q)/\hbar - \mu_j \pi/2)} \tag{B.6}$$

where

$$S_j(q) = \int_{q^\circ}^{q} p dq. \tag{B.7}$$

$$A_j(q) = \sqrt{\frac{J(t=0, q_j^\circ)}{J(t, q_j^\circ)}}, \tag{B.8}$$

$$J(t, q_j^\circ) = \left| det \left[\frac{\partial q_j(t, q_j^\circ)}{\partial (t, q_j^\circ)} \right] \right|. \tag{B.9}$$

Here q° represents points on a spherical surface centered on the origin with radius r_{out} where both approximations are applicable. $S_j(q), A_j(q)$ are the classical action function and the classical amplitude function respectively, and μ_j is the Maslov index which describes the additional phase shifts of the wave caused by the singular points on the trajectories. The algorithm to calculate these quantities will be given in section B.2.

3. In the inner region, according to the first approximation, the returning wave is proportional to a zero-energy Coulomb scattering wave:

$$\psi^j_{ret}(\vec{r}) \sim N_j \psi_{c,inc}(r, \theta, \phi) \tag{B.10}$$

with

$$\psi_{c,inc}(r, \theta, \phi) = 2J_{0,inc}(\sqrt{r(1 - cos\theta_k cos\theta - sin\theta_k sin\theta cos(\phi - \phi_k))}), \tag{B.11}$$

where θ_k, ϕ_k denote the spherical polar angles of $\hat{k}$, and θ, ϕ, r denote the spherical coordinates of $\vec{r}$. $J_{0,inc}$ is the incoming part of a Bessel function. Using a partial wave

expansion, $\psi_c(r,\theta,\phi)$ can be expressed as:

$$\begin{aligned}\psi_c(r,\theta,\phi) &= 4\pi/\sqrt{2}\sum_{l,m} Y^*_{lm}(\theta_k,\phi_k)Y_{lm}(\theta,\phi)J_{2l+1}(\sqrt{8r})/\sqrt{r} \\ &= 4\pi/\sqrt{2}\sum_{l,m}(-1)^l Y^*_{lm}(\theta_{ret},\phi_{ret})Y_{lm}(\theta,\phi)J_{2l+1}(\sqrt{8r})/\sqrt{r} \quad \text{(B.12)}\end{aligned}$$

where we have used $\theta_k = \pi - \theta_{ret}, \phi_k = \pi + \phi_{ret}$.

4. On the returning surface ($r = r_{ret}$), both Eq. (B.6) and Eq. (B.10) are applicable. $\psi^j_{semi,ret}(\vec{r}) = \psi^j_{ret}(\vec{r})$, hence N_j is determined.

The returning point of a closed orbit on the returning surface is defined by $(r_{ret}, \theta^j_{ret}, \phi^j_{ret})$. From Eq. (B.6) the corresponding semiclassical returning wave is given by:

$$\psi^j_{semi,ret}(\vec{r}_{ret}) = \psi_{out}(r_{out},\theta^j_{out},\phi^j_{out})A_j(r_{ret},\theta^j_{ret},\phi^j_{ret})e^{i(s_j(t_{ret})/\hbar - \mu_j\pi/2)} \quad \text{(B.13)}$$

Noting that $\theta_k = \pi - \theta_{ret}, \phi_k = \pi + \phi_{ret}$, the returning function given by equations (B.10) and (B.11) can be simplified as:

$$\psi^j_{ret}(r_{ret}) = N_j J_{0,inc}(\sqrt{8r_{ret}})$$

Comparing this to the semiclassical returning wave function given by (B.13), we find that N_j must be

$$N_j = \frac{\psi_{out}(r_{out},\theta^j_{out},\phi^j_{out})}{J_{0,inc}(\sqrt{8r_{ret}})}A_j(q^j_{ret})exp[i(s_j(t^j_{ret})/\hbar - \mu_j\pi/2)]$$

Inserting N_j into (B.10) with the Coulomb wave function given by the partial-wave expansion(B.12), we get:

$$\begin{aligned}\psi^j_{ret}(r,\theta,\phi) &= \sum_{l,m} a_{lm}Y_{lm}(\theta,\phi)J_{2l+1}(\sqrt{8r})\psi_{out}(r_{out},\theta^j_{out},\phi^j_{out})/\sqrt{r} \\ &= \int \sum_{l,m} a_{lm}Y_{lm}(\theta,\phi)\frac{J_{2l+1}(\sqrt{8r})}{\sqrt{r}}G^+_{dir}(q^j_{out},q',E)D(q')\psi_i(q')dq' \quad \text{(B.14)}\end{aligned}$$

where we have used Eq. (B.5). a_{lm} is given by

$$a_{lm} = (-1)^l \frac{4\pi}{\sqrt{2}} \frac{A_j(q_{ret})}{J_{0,inc}(\sqrt{8r})} Y^*_{lm}(\theta_{ret}, \phi_{ret}) e^{i(s_j(t_{ret})/\hbar - \mu_j \pi/2)}$$

5. According to the relation between returning waves and the returning Green's function:

$$\psi_{ret}(q) = \int G^+_{ret}(q, q'; E) D(q') \psi_i(q') dq', \tag{B.15}$$

we can read out G^+_{ret} from Eq. (B.14):

$$G^{+j}_{ret}(q, q'; E) = \sum_{l_1 l_2 m_1 m_2} d^j_{l_1 m_1, l_2 m_2} Y^*_{l_2 m_2}(\theta', \phi') \frac{J_{2l_2+1}(\sqrt{8r'})}{\sqrt{r'}} Y_{l_1 m_1}(\theta, \phi) \frac{J_{2l_1+1}(\sqrt{8r})}{\sqrt{r}} \tag{B.16}$$

with

$$\begin{aligned} d^j_{l_1 m_1, l_2 m_2} &= -i 2^{9/4} \pi^{3/2} r_{out}^{-3/4} \frac{A_j(q^j_{ret})}{J_{0,inc}(\sqrt{8 r_{ret}})} e^{-i3/4\pi} e^{i\sqrt{8 r_{out}}} e^{i(\frac{s_j(t^j_{ret})}{\hbar} - \frac{\mu_j \pi}{2})} \\ &\times (-1)^{l_1+l_2} Y^*_{l_1 m_1}(\theta^j_{ret}, \phi^j_{ret}) Y_{l_2 m_2}(\theta^j_{out}, \phi^j_{out}) \end{aligned} \tag{B.17}$$

From Eq. (B.2) with the formulas for G^+_{dir} in Eq. (B.3) and G^+_{ret} in Eq. (B.16), the oscillator strength density is given as a function of energy by a smooth background plus a sum of oscillatory contributions from the closed orbits:

$$Df(E) = Df_0(E) + \sum_j C_j(E) sin\Delta_j(E) \tag{B.18}$$

The smooth term is the same as Eq. (5.10) in [1]b. In the oscillatory term, the phase is given by

$$\Delta_j = S_j(E)/\hbar - \frac{\pi}{2}\mu_j, \tag{B.19}$$

and the amplitude is given by

$$C_j = (E - E_i) 2^{9/2} \pi r_{out}^{-3/4} r_{ret}^{-1/4} A_j(q^j_{ret}) y^*(\theta^j_{ret}, \phi^j_{ret}) y(\theta^j_{out}, \phi^j_{out}) \tag{B.20}$$

with

$$y(\theta,\phi)=\sum_{l_1 m}(-1)^{l_1} I(n,l,l_1) b_{l_1,m} Y_{l_1 m}(\theta,\phi).$$

B.2 The implementation of closed orbit theory

To calculate the absorption spectrum from the closed orbit theory, we need to search for the closed orbits and calculate the classical quantities associated with each closed orbit. Since in KS coordinates, Coulomb singularity is eliminated, we can launch trajectories at the origin and search for trajectories which return to the origin later. To calculate the classical amplitude, we can integrate the closed orbit with two of its neighbors until the closed orbit returns to the origin.

- The initiation of the trajectories at the origin in KS space

  In the Cartesian coordinate space, the singularity at the origin prevents us from starting the trajectory at the origin. However, in the region $r \leq 50a_0 \sim 100a_0$, the external fields are negligible and the trajectories go outwards radially. The trajectories launched at the origin along the direction defined by polar angle θ and azimuthal angle ϕ are the same as the trajectories radially outgoing along the same direction on a sphere centered at the origin with radius $r_{out} < 50a_0$. Therefore, we can find the initial conditions on the sphere for trajectories which start at the origin, then calculate the corresponding initial conditions in KS space from them. We set $r_{out} = 0$ in the initial conditions in the KS space to find the initial conditions in the KS space at the origin. The Hamiltonian in the 3-D physical space in the region $r \leq 50a_0 \sim 100a_0$ is:

  $$H = p^2/2 - 1/r_{out}.$$

  For $H \approx 0$, we have $p = \dot{r} = \sqrt{2/r_{out}}$.

When we launch trajectories at r_{out} from $t = 0$ along the direction defined by (θ, ϕ), the initial conditions in 3-D physical space are given by:

$$x = r_{out} \sin\theta \cos\phi, \tag{B.21}$$

$$y = r_{out} \sin\theta \sin\phi, \tag{B.22}$$

$$z = r_{out} \cos\theta, \tag{B.23}$$

$$\dot{x} = \sqrt{2/r_{out}} \sin\theta \cos\phi, \tag{B.24}$$

$$\dot{y} = \sqrt{2/r_{out}} \sin\theta \sin\phi, \tag{B.25}$$

$$\dot{z} = \sqrt{2/r_{out}} \cos\theta. \tag{B.26}$$

Now we may compute the initial conditions for u_α and u'_α $(\alpha = 1, 2, 3, 4)$ from:

if $z \geq 0$

$$u_1^2 + u_4^2 = \frac{1}{2}(r + z),\ u_2 = \frac{xu_1 + yu_4}{r + z},\ u_3 = \frac{yu_1 - xu_4}{r + z}$$

else

$$u_2^2 + u_3^2 = \frac{1}{2}(r - z),\ u_1 = \frac{xu_2 + yu_3}{r - z},\ u_4 = \frac{y}{r - z}$$

and

$$u'_1 = 2(u_1\dot{z} + u_2\dot{x} + u_3\dot{y}) \tag{B.27}$$

$$u'_2 = 2(-u_2\dot{z} + u_1\dot{x} + u_4\dot{y}) \tag{B.28}$$

$$u'_3 = 2(-u_3\dot{z} - u_4\dot{x} + u_1\dot{y}) \tag{B.29}$$

$$u'_4 = 2(u_4\dot{z} - u_3\dot{x} + u_2\dot{y}) \tag{B.30}$$

The solution with conditions of $u_4 = 0$ and $u'_4 = 0$ is

$$u_1 = \sqrt{r_{out}} \cos(\theta/2), \qquad u'_1 = 2\sqrt{2} \cos(\theta/2),$$

$$u_2 = \sqrt{r_{out}} \sin(\theta/2) \cos\phi, \qquad u'_2 = 2\sqrt{2} \sin(\theta/2) \cos\phi,$$

$$u_3 = \sqrt{r_{out}} \sin(\theta/2) \sin\phi, \qquad u'_3 = 2\sqrt{2} \sin(\theta/2) \sin\phi,$$

$$u_4 = 0, \qquad u'_4 = 0.$$

Now let $r_{out} = 0$, from Eq. (2.12) we obtain the initial conditions at the origin in the KS space:

$$\begin{aligned} u_1 &= u_2 = u_3 = u_4 = 0, \\ p_1 &= 2\sqrt{2}\cos(\theta/2), \\ p_2 &= 2\sqrt{2}\sin(\theta/2)\cos\phi, \\ p_3 &= 2\sqrt{2}\sin(\theta/2)\sin\phi, \\ p_4 &= 0. \end{aligned} \tag{B.31}$$

- Strategy to search for closed orbits

We use (B.31) to launch the trajectories with θ from 0° to 90°, ϕ from 0° to 360° and find the rest of the closed orbits using reflection through the xy plane (for every orbit beginning at (θ, ϕ), there is another beginning at $(\pi - \theta, \phi)$). We vary θ with stepsize 0.09° and ϕ with stepsize 0.36°. The stepsizes of θ and ϕ are determined by numerical experiments and are just small enough to isolate closed orbits in different boxes.

Since we are seeking relatively short closed orbits, we integrate the equations of motion up to a maximum time $10T_c$, where T_c is the electron cyclotron time. $T_c = (2\pi m_e c/Be)$. Seeking closed orbits includes three steps:

1. For the defined grid of $(\theta_{out,i}, \phi_{out,j})$, we integrate the equations of motion until u_1 comes back to zero. At that point, we record $\theta_{out,i}, \phi_{out,j}$, and $r_{ij} = u_1^2 + u_2^2 + u_3^2 + u_4^2$. We continue the integration until u_1 again returns to zero and record the same information. This is repeated until $t = 10T_c$.

2. We compare r_{ij} with its eight nearest neighbors $r_{i+a,j+b}$, $(a, b = 1, 0, -1)$. If r_{ij} is less than all of its neighbors, we interpret it as a local minimum, and search its vicinity for a closed orbit.

3. We use the Powell hybrid method [39] to seek a local zero of the nonlinear equations $u_2(\theta_{out}, \phi_{out}) = 0$ and $u_3(\theta_{out}, \phi_{out}) = 0$ within the box defined by the neighbors of a local minimum. If we find such a solution and u_4 is also zero (to some tolerance) at that point, this local zero gives us a closed orbit.

After we find the closed orbits, we are ready to calculate the spectral oscillations caused by closed orbits. We need to evaluate classical action, amplitude, and Maslov index corresponding to each closed orbit.

- The classical action in rescaled coordinate space

  The classical action is defined as:

$$S_j(q) = \int p_x dx + p_y dy + p_z dz = \int (p_x \dot{x} + p_y \dot{y} + p_z \dot{z}) dt.$$

  Since the KS transformation defined in chapter 2 is a canonical point-transformation, we may prove that

$$S_j(q) = \int p_i \frac{du_i}{ds} ds = \int (p_1 u_1' + p_2 u_2' + p_3 u_3' + p_4 u_4') ds.$$

  Substituting equations of motion into this expression, we have

$$S_j(q) = \int [p^2 + (2u_2 p_3 - 2u_3 p_2) u^2] ds. \tag{B.32}$$

  Therefore, in order to evaluate the classical action correlated with a closed orbit, we only need to integrate the quantity in the bracket along the closed orbit.

- Classical amplitude and recurrence amplitude

  The classical amplitude is defined as the square root of the ratio of initial and final Jacobians

$$A_j(q) = \sqrt{\frac{J(t = 0, q_j^\circ)}{J(t, q_j^\circ)}}. \tag{B.33}$$

The initial Jacobian can be calculated by evaluating the expression:

$$\begin{aligned} J(0,\theta_{out},\phi_{out}) &= \frac{\partial(x,y,z)}{\partial(t,\theta_{out},\phi_{out})}|_{t=0} \\ &= \frac{\partial(x,y,z)}{\partial(r,\theta,\phi)}\frac{\partial(r,\theta,\phi)}{\partial(t,\theta_{out},\phi_{out})}|_{t=0} \\ &= r^2\sin\theta\frac{\partial(r,\theta,\phi)}{\partial(t,\theta_{out},\phi_{out})}|_{t=0} \end{aligned}$$

which is

$$J(0,\theta_{out},\phi_{out}) = r^2\sin\theta \left| \begin{array}{ccc} \dot{r} & (\partial r/\partial\theta_{out})_{t,\phi_{out}} & (\partial r/\partial\phi_{out})_{t,\theta_{out}} \\ \dot{\theta} & (\partial\theta/\partial\theta_{out})_{t,\phi_{out}} & (\partial\theta/\partial\phi_{out})_{t,\theta_{out}} \\ \dot{\phi} & (\partial\phi/\partial\theta_{out})_{t,\phi_{out}} & (\partial\phi/\partial\phi_{out})_{t,\theta_{out}} \end{array} \right|_{t=0}.$$

Since we start the trajectories radially outgoing.

$$\frac{\partial\theta}{\partial t}|_{t=0} = \frac{\partial\phi}{\partial t}|_{t=0} = 0,$$

so the evaluation of the initial Jacobians is

$$J_{sc}(0,\theta_{out},\phi_{out}) = r_{out}^2\sin\theta_{out}\dot{r}_{out}.$$

We have showed that

$$\dot{r}_{out} = \sqrt{\frac{2}{r_{out}}},$$

so finally, the initial Jacobian is simplified as

$$J_{sc}(0,\theta_{out},\phi_{out}) = \sqrt{2}r_{out}^{3/2}\sin\theta_{out} \tag{B.34}$$

For the final Jacobian, we may write it in terms of the coordinates in R_4

$$J(t_{ret},\theta_{out},\phi_{out}) = \frac{\partial(x,y,z)}{\partial(u_1,u_2,u_3,u_4)}\frac{\partial(u_1,u_2,u_3,u_4)}{\partial(s,\theta_{out},\phi_{out})}\frac{\partial(s,\theta_{out},\phi_{out})}{\partial(t,\theta_{out},\phi_{out})}|_{t=t_{ret}}$$

Here, we take the determinant of the product of matrices. Using the KS transformation from (x, y, z) to (u_1, u_2, u_3, u_4), the first matrix is given by

$$\frac{\partial(x, y, z)}{\partial(u_1, u_2, u_3, u_4)} = \left| \begin{array}{cccc} 2u_2 & 2u_1 & -2u_4 & -2u_3 \\ 2u_3 & 2u_4 & 2u_1 & 2u_2 \\ 2u_1 & -2u_2 & -2u_3 & 2u_4 \end{array} \right|_{t=t_{ret}} \tag{B.35}$$

For a closed orbit, since it is radially incoming, we have the following relations at $t = t_{ret}$:

$$\frac{u_i}{u} = -\frac{p_i}{p} \; (i = 1, 2, 3, 4)$$

with $u^2 = u_1^2 + u_2^2 + u_3^2 + u_4^2$ and $p^2 = p_1^2 + p_2^2 + p_3^2 + p_4^2$.

With these relations, the first matrix can be expressed as

$$\frac{\partial(x, y, z)}{\partial(u_1, u_2, u_3, u_4)} = \left| \begin{array}{cccc} 2\frac{u}{p}p_2 & 2\frac{u}{p}p_1 & -2\frac{u}{p}p_4 & -2\frac{u}{p}p_3 \\ 2\frac{u}{p}p_3 & 2\frac{u}{p}p_4 & 2\frac{u}{p}p_1 & 2\frac{u}{p}p_2 \\ 2\frac{u}{p}p_1 & -2\frac{u}{p}p_2 & -2\frac{u}{p}p_3 & 2\frac{u}{p}p_4 \end{array} \right|_{t=t_{ret}} \tag{B.36}$$

The second matrix is

$$\frac{\partial(u_1, u_2, u_3, u_4)}{\partial(s, \theta_{out}, \phi_{out})} = \left| \begin{array}{ccc} \frac{\partial u_1}{\partial s} & (\frac{\partial u_1}{\partial \theta_{out}})_{s,\phi_{out}} & (\frac{\partial u_1}{\partial \phi_{out}})_{s,\theta_{out}} \\ \frac{\partial u_2}{\partial s} & (\frac{\partial u_2}{\partial \theta_{out}})_{s,\phi_{out}} & (\frac{\partial u_2}{\partial \phi_{out}})_{s,\theta_{out}} \\ \frac{\partial u_3}{\partial s} & (\frac{\partial u_3}{\partial \theta_{out}})_{s,\phi_{out}} & (\frac{\partial u_3}{\partial \phi_{out}})_{s,\theta_{out}} \\ \frac{\partial u_4}{\partial s} & (\frac{\partial u_4}{\partial \theta_{out}})_{s,\phi_{out}} & (\frac{\partial u_4}{\partial \phi_{out}})_{s,\theta_{out}} \end{array} \right|_{s=s_{ret}} \tag{B.37}$$

Through running three trajectories (one closed orbit, and two neighboring trajectories) together, we may get the data for neighboring trajectories at the same time. Hence this matrix can be evaluated by taking finite differences.

Because $\frac{\partial s}{\partial t} = \frac{1}{4r_{ret}}$, the third matrix is simplified as:

$$\frac{\partial(s, \theta_{out}, \phi_{out})}{\partial(t, \theta_{out}, \phi_{out})|_{t=t_{ret}}} = \frac{1}{4r_{ret}} \tag{B.38}$$

If we combine all of them together, the final Jacobian is given by

$$J(t_{ret}, \theta_{out}, \phi_{out})$$

$$= \frac{2r_{ret}^{1/2}}{p_{ret}^3} \begin{vmatrix} p_2 & p_1 & -p_4 & -p_3 \\ p_3 & p_4 & p_1 & p_2 \\ p_1 & -p_2 & -p_3 & p_4 \end{vmatrix}_{t=t_{ret}} \begin{vmatrix} \frac{\partial u_1}{\partial s} & (\frac{\partial u_1}{\partial \theta_{out}})_{s,\phi_{out}} & (\frac{\partial u_1}{\partial \phi_{out}})_{s,\theta_{out}} \\ \frac{\partial u_2}{\partial s} & (\frac{\partial u_2}{\partial \theta_{out}})_{s,\phi_{out}} & (\frac{\partial u_2}{\partial \phi_{out}})_{s,\theta_{out}} \\ \frac{\partial u_3}{\partial s} & (\frac{\partial u_3}{\partial \theta_{out}})_{s,\phi_{out}} & (\frac{\partial u_3}{\partial \phi_{out}})_{s,\theta_{out}} \\ \frac{\partial u_4}{\partial s} & (\frac{\partial u_4}{\partial \theta_{out}})_{s,\phi_{out}} & (\frac{\partial u_4}{\partial \phi_{out}})_{s,\theta_{out}} \end{vmatrix}_{t=t_{ret}} \quad \text{(B.39)}$$

where we have used $u = \sqrt{r_{ret}}$.

After inserting (B.35),(B.40) into (B.34), we have

$$A(t_{ret}, \theta_{out}, \phi_{out}) =$$

$$coef. \left[\begin{vmatrix} p_2 & p_1 & -p_4 & -p_3 \\ p_3 & p_4 & p_1 & p_2 \\ p_1 & -p_2 & -p_3 & p_4 \end{vmatrix}_{t=t_{ret}} \begin{vmatrix} \frac{\partial u_1}{\partial s} & (\frac{\partial u_1}{\partial \theta_{out}})_{s,\phi_{out}} & (\frac{\partial u_1}{\partial \phi_{out}})_{s,\theta_{out}} \\ \frac{\partial u_2}{\partial s} & (\frac{\partial u_2}{\partial \theta_{out}})_{s,\phi_{out}} & (\frac{\partial u_2}{\partial \phi_{out}})_{s,\theta_{out}} \\ \frac{\partial u_3}{\partial s} & (\frac{\partial u_3}{\partial \theta_{out}})_{s,\phi_{out}} & (\frac{\partial u_3}{\partial \phi_{out}})_{s,\theta_{out}} \\ \frac{\partial u_4}{\partial s} & (\frac{\partial u_4}{\partial \theta_{out}})_{s,\phi_{out}} & (\frac{\partial u_4}{\partial \phi_{out}})_{s,\theta_{out}} \end{vmatrix}_{t=t_{ret}} \right]^{-1/2} \quad \text{(B.40)}$$

with $coef. = 2^{-1/4} r_{out}^{3/4} r_{ret}^{-1/4} p_{ret}^{3/2} \sin^{1/2}\theta_{out}$.

From (3.3), the recurrence amplitude is related to the semiclassical amplitude by

$$C_j = (E - E_i) 2^{9/2} \pi \frac{m_e}{\hbar^2} r_{out}^{-3/4} r_{ret}^{1/4} A_j(q_{ret}^j) y^*(\theta_{ret}^j, \phi_{ret}^j) y(\theta_{out}^j, \phi_{out}^j). \quad \text{(B.41)}$$

The product $r_{out}^{-3/4} r_{ret}^{1/4}$ is cancelled by the product $r_{out}^{3/4} r_{ret}^{-1/4}$ in $A(t_{ret}, \theta_{out}, \phi_{out})$, which allows us to take the limit $r_{out} = r_{ret} \to 0$.

As $r_{out} = r_{ret} \to 0$, we have following relations:

$$p_{ret} = 2\sqrt{2}, \; u_i' = p_i \; (i = 1, 2, 3, 4)$$

Substituting them into $A(q_{ret}, \theta_{out}, \phi_{out})$, we get

$$r_{out}^{-3/4} r_{ret}^{1/4} A(t_{ret}, \theta_{out}, \phi_{out})$$

$$= 4 \sin^{1/2}\theta_{out} \left[\begin{vmatrix} p_2 & p_1 & -p_4 & -p_3 \\ p_3 & p_4 & p_1 & p_2 \\ p_1 & -p_2 & -p_3 & p_4 \end{vmatrix} \begin{vmatrix} \frac{\partial u_1}{\partial s} & (\frac{\partial u_1}{\partial \theta_{out}})_{s,\phi_{out}} & (\frac{\partial u_1}{\partial \phi_{out}})_{s,\theta_{out}} \\ \frac{\partial u_2}{\partial s} & (\frac{\partial u_2}{\partial \theta_{out}})_{s,\phi_{out}} & (\frac{\partial u_2}{\partial \phi_{out}})_{s,\theta_{out}} \\ \frac{\partial u_3}{\partial s} & (\frac{\partial u_3}{\partial \theta_{out}})_{s,\phi_{out}} & (\frac{\partial u_3}{\partial \phi_{out}})_{s,\theta_{out}} \\ \frac{\partial u_4}{\partial s} & (\frac{\partial u_4}{\partial \theta_{out}})_{s,\phi_{out}} & (\frac{\partial u_4}{\partial \phi_{out}})_{s,\theta_{out}} \end{vmatrix} \right]^{-1/2}_{t=t_{ret}} \quad \text{(B.42)}$$

Eq. (B.41) and Eq. (B.42) together give the recurrence amplitude at the origin for a closed orbit.

- Maslov index μ_j

  The Maslov index is calculated by counting caustics and foci where the Jacobian goes to zero and $A(q)$ goes to infinity. As the trajectory passes through either of a caustic or a focus, the Maslov index increases by 1. Two methods can be used to find the caustic and foci. One of them monitors the sign of $J(t, \theta_{out}, \phi_{out})$ along the trajectories. Every time a trajectory passes through a caustic or focus, the sign of $J(t, \theta_{out}, \phi_{out})$ changes. We use this method in our calculation. The Jacobian $J(t, \theta_{out}, \phi_{out})$ along the trajectories can be written as :

$$J(t, \theta_{out}, \phi_{out}) = \frac{\partial(x, y, z)}{\partial(u_1, u_2, u_3, u_4)} \frac{\partial(u_1, u_2, u_3, u_4)}{\partial(s, \theta_{out}, \phi_{out})} \frac{\partial(s, \theta_{out}, \phi_{out})}{\partial(t, \theta_{out}, \phi_{out})}.$$

  Here, we take the determinant of the product of matrices.

  The same as in section 3.2.4, substituting in KS transformation for (x, y, z), the first matrix is given by

$$\frac{\partial(x, y, z)}{\partial(u_1, u_2, u_3, u_4)} = \begin{vmatrix} 2u_2 & 2u_1 & -2u_4 & -2u_3 \\ 2u_3 & 2u_4 & 2u_1 & 2u_2 \\ 2u_1 & -2u_2 & -2u_3 & 2u_4 \end{vmatrix}_t \quad \text{(B.43)}$$

The second matrix is

$$\frac{\partial(u_1, u_2, u_3, u_4)}{\partial(s, \theta_{out}, \phi_{out})} = \left| \begin{array}{ccc} \frac{\partial u_1}{\partial s} & (\frac{\partial u_1}{\partial \theta_{out}})_{s,\phi_{out}} & (\frac{\partial u_1}{\partial \phi_{out}})_{s,\theta_{out}} \\ \frac{\partial u_2}{\partial s} & (\frac{\partial u_2}{\partial \theta_{out}})_{s,\phi_{out}} & (\frac{\partial u_2}{\partial \phi_{out}})_{s,\theta_{out}} \\ \frac{\partial u_3}{\partial s} & (\frac{\partial u_3}{\partial \theta_{out}})_{s,\phi_{out}} & (\frac{\partial u_3}{\partial \phi_{out}})_{s,\theta_{out}} \\ \frac{\partial u_4}{\partial s} & (\frac{\partial u_4}{\partial \theta_{out}})_{s,\phi_{out}} & (\frac{\partial u_4}{\partial \phi_{out}})_{s,\theta_{out}} \end{array} \right|_t \tag{B.44}$$

The third matrix is simplified as

$$\frac{\partial(s, \theta_{out}, \phi_{out})}{\partial(t, \theta_{out}, \phi_{out})|_{t=t_{ret}}} = \frac{1}{4r} \tag{B.45}$$

So the Jacobian along the trajectories is given by

$$J(t, \theta_{out}, \phi_{out}) = \frac{1}{4r} \left| \begin{array}{cccc} p_2 & p_1 & -p_4 & -p_3 \\ p_3 & p_4 & p_1 & p_2 \\ p_1 & -p_2 & -p_3 & p_4 \end{array} \right|_t \left| \begin{array}{ccc} \frac{\partial u_1}{\partial s} & (\frac{\partial u_1}{\partial \theta_{out}})_{s,\phi_{out}} & (\frac{\partial u_1}{\partial \phi_{out}})_{s,\theta_{out}} \\ \frac{\partial u_2}{\partial s} & (\frac{\partial u_2}{\partial \theta_{out}})_{s,\phi_{out}} & (\frac{\partial u_2}{\partial \phi_{out}})_{s,\theta_{out}} \\ \frac{\partial u_3}{\partial s} & (\frac{\partial u_3}{\partial \theta_{out}})_{s,\phi_{out}} & (\frac{\partial u_3}{\partial \phi_{out}})_{s,\theta_{out}} \\ \frac{\partial u_4}{\partial s} & (\frac{\partial u_4}{\partial \theta_{out}})_{s,\phi_{out}} & (\frac{\partial u_4}{\partial \phi_{out}})_{s,\theta_{out}} \end{array} \right|_t \tag{B.46}$$

There are two ways to evaluate the partial derivatives in the second matrix:

1. Run three trajectories (one closed orbit, and two neighbors) together and get the data for the neighbor trajectories at the same time. Then we evaluate the partial derivatives by taking finite differences.

   This method is straight forward and easy to implement. However, it is valid only if the neighbor trajectories are well-focused, that is, they remain close to each other.

2. Derive linear equations for $\frac{\partial u_i}{\partial \theta_{out}}$, $\frac{\partial u_i}{\partial \phi_{out}}$, $\frac{\partial p_i}{\partial \theta_{out}}$, $\frac{\partial p_i}{\partial \phi_{out}}$ with $i = 1, 2, 3, 4$ from the Hamiltonian equations of motion. We initialize $\frac{\partial u_i}{\partial \theta_{out}}$, $\frac{\partial u_i}{\partial \phi_{out}}$, $\frac{\partial p_i}{\partial \theta_{out}}$, $\frac{\partial p_i}{\partial \phi_{out}}$ from (B. 31), and integrate the linear equations for $\frac{\partial u_i}{\partial \theta_{out}}$, $\frac{\partial u_i}{\partial \phi_{out}}$, $\frac{\partial p_i}{\partial \theta_{out}}$, $\frac{\partial p_i}{\partial \phi_{out}}$ to find $\frac{\partial u_i}{\partial \theta_{out}}$, $\frac{\partial u_i}{\partial \phi_{out}}$ at any time s.

This method needs more work since we must derive and compute the linear equations for $\frac{\partial u_i}{\partial \theta_{out}}$, $\frac{\partial u_i}{\partial \phi_{out}}$, $\frac{\partial p_i}{\partial \theta_{out}}$, $\frac{\partial p_i}{\partial \phi_{out}}$, but it gives accurate values of the partial derivatives.

Now we derive the linear equations for $\frac{\partial u_i}{\partial \theta_{out}}$, $\frac{\partial u_i}{\partial \phi_{out}}$, $\frac{\partial p_i}{\partial \theta_{out}}$, $\frac{\partial p_i}{\partial \phi_{out}}$.

We apply a time derivative on the partial derivatives to obtain

$$\begin{aligned}
\frac{d}{ds}\frac{\partial u_i}{\partial \theta_{out}} &= \frac{\partial u_i'}{\partial \theta_{out}}, \\
\frac{d}{ds}\frac{\partial u_i}{\partial \phi_{out}} &= \frac{\partial u_i'}{\partial \phi_{out}}, \\
\frac{d}{ds}\frac{\partial p_i}{\partial \theta_{out}} &= \frac{\partial p_i'}{\partial \theta_{out}}, \\
\frac{d}{ds}\frac{\partial p_i}{\partial \phi_{out}} &= \frac{\partial p_i'}{\partial \phi_{out}}.
\end{aligned} \tag{B.47}$$

where the prime is the derivative with respect to s and i goes from 1 to 4. Since u_i' and p_i' depend on u_i, p_i with $i = 1, 2, 3, 4$, the partial derivatives of u_i', p_i' can be written as

$$\begin{aligned}
\frac{\partial u_i'}{\partial \theta_{out}} &= \sum_j \left(\frac{\partial u_i'}{\partial u_j}\frac{\partial u_j}{\partial \theta_{out}} + \frac{\partial u_i'}{\partial p_j}\frac{\partial p_j}{\partial \theta_{out}}\right) \\
\frac{\partial u_i'}{\partial \phi_{out}} &= \sum_j \left(\frac{\partial u_i'}{\partial u_j}\frac{\partial u_j}{\partial \phi_{out}} + \frac{\partial u_i'}{\partial p_j}\frac{\partial p_j}{\partial \phi_{out}}\right) \\
\frac{\partial p_i'}{\partial \theta_{out}} &= \sum_j \left(\frac{\partial p_i'}{\partial u_j}\frac{\partial u_j}{\partial \theta_{out}} + \frac{\partial p_i'}{\partial p_j}\frac{\partial p_j}{\partial \theta_{out}}\right) \\
\frac{\partial p_i'}{\partial \phi_{out}} &= \sum_j \left(\frac{\partial p_i'}{\partial u_j}\frac{\partial u_j}{\partial \phi_{out}} + \frac{\partial p_i'}{\partial p_j}\frac{\partial p_j}{\partial \phi_{out}}\right)
\end{aligned} \tag{B.48}$$

with $i, j = 1, 2, 3, 4$.

Hence the linear equations for $\frac{\partial u_1}{\partial \theta_{out}}$, $\frac{\partial u_1}{\partial \phi_{out}}$, $\frac{\partial p_1}{\partial \theta_{out}}$, $\frac{\partial p_1}{\partial \phi_{out}}$ are given by:

$$\frac{d}{ds}\begin{pmatrix} \frac{\partial u_1}{\partial \theta_{out}} \\ \frac{\partial u_2}{\partial \theta_{out}} \\ \frac{\partial u_3}{\partial \theta_{out}} \\ \frac{\partial u_4}{\partial \theta_{out}} \\ \frac{\partial p_1}{\partial \theta_{out}} \\ \frac{\partial p_2}{\partial \theta_{out}} \\ \frac{\partial p_3}{\partial \theta_{out}} \\ \frac{\partial p_4}{\partial \theta_{out}} \end{pmatrix} = \frac{\partial(u_1', u_2', u_3', u_4', p_1', p_2', p_3', p_4')}{\partial(u_1, u_2, u_3, u_4, p_1, p_2, p_3, p_4)} \begin{pmatrix} \frac{\partial u_1}{\partial \theta_{out}} \\ \frac{\partial u_2}{\partial \theta_{out}} \\ \frac{\partial u_3}{\partial \theta_{out}} \\ \frac{\partial u_4}{\partial \theta_{out}} \\ \frac{\partial p_1}{\partial \theta_{out}} \\ \frac{\partial p_2}{\partial \theta_{out}} \\ \frac{\partial p_3}{\partial \theta_{out}} \\ \frac{\partial p_4}{\partial \theta_{out}} \end{pmatrix} \tag{B.49}$$

$$\frac{d}{ds}\begin{pmatrix} \frac{\partial u_1}{\partial \phi_{out}} \\ \frac{\partial u_2}{\partial \phi_{out}} \\ \frac{\partial u_3}{\partial \phi_{out}} \\ \frac{\partial u_4}{\partial \phi_{out}} \\ \frac{\partial p_1}{\partial \phi_{out}} \\ \frac{\partial p_2}{\partial \phi_{out}} \\ \frac{\partial p_3}{\partial \phi_{out}} \\ \frac{\partial p_4}{\partial \phi_{out}} \end{pmatrix} = \frac{\partial(u_1', u_2', u_3', u_4', p_1', p_2', p_3', p_4')}{\partial(u_1, u_2, u_3, u_4, p_1, p_2, p_3, p_4)} \begin{pmatrix} \frac{\partial u_1}{\partial \phi_{out}} \\ \frac{\partial u_2}{\partial \phi_{out}} \\ \frac{\partial u_3}{\partial \phi_{out}} \\ \frac{\partial u_4}{\partial \phi_{out}} \\ \frac{\partial p_1}{\partial \phi_{out}} \\ \frac{\partial p_2}{\partial \phi_{out}} \\ \frac{\partial p_3}{\partial \phi_{out}} \\ \frac{\partial p_4}{\partial \phi_{out}} \end{pmatrix} \tag{B.50}$$

From the Hamiltonian differential equations, the partial derivatives of u_i', p_i' are given by:

$$\begin{array}{llllll}
u_1': & \frac{\partial u_1'}{\partial u_1} = 0 & \frac{\partial u_1'}{\partial u_2} = 0 & \frac{\partial u_1'}{\partial u_3} = 0 & \frac{\partial u_1'}{\partial u_4} = 0 \\
 & \frac{\partial u_1'}{\partial p_1} = 1 & \frac{\partial u_1'}{\partial p_2} = 0 & \frac{\partial u_1'}{\partial p_3} = 0 & \frac{\partial u_1'}{\partial p_4} = 0 \\
u_2': & \frac{\partial u_2'}{\partial u_1} = -8u_3u_1 & \frac{\partial u_2'}{\partial u_2} = -8u_3u_2 & \frac{\partial u_2'}{\partial u_3} = -4u^2 - 8u_3^2 & \frac{\partial u_2'}{\partial u_4} = -8u_3u_4 \\
 & \frac{\partial u_2'}{\partial p_1} = 0 & \frac{\partial u_2'}{\partial p_2} = 1 & \frac{\partial u_2'}{\partial p_3} = 0 & \frac{\partial u_2'}{\partial p_4} = 0
\end{array}$$

$$
\begin{array}{lllll}
u_3': & \frac{\partial u_3'}{\partial u_1} = 8u_2u_1 & \frac{\partial u_3'}{\partial u_2} = 4u^2 + 8u_2^2 & \frac{\partial u_3'}{\partial u_3} = 8u_2u_3 & \frac{\partial u_3'}{\partial u_4} = 8u_2u_4 \\
 & \frac{\partial u_3'}{\partial p_1} = 0 & \frac{\partial u_3'}{\partial p_2} = 0 & \frac{\partial u_3'}{\partial p_3} = 1 & \frac{\partial u_3'}{\partial p_4} = 0 \\
u_4': & \frac{\partial u_4'}{\partial u_1} = 0 & \frac{\partial u_4'}{\partial u_2} = 0 & \frac{\partial u_4'}{\partial u_3} = 0 & \frac{\partial u_4'}{\partial u_4} = 0 \\
 & \frac{\partial u_4'}{\partial p_1} = 0 & \frac{\partial u_4'}{\partial p_2} = 0 & \frac{\partial u_4'}{\partial p_3} = 0 & \frac{\partial u_4'}{\partial p_4} = 1
\end{array}
$$

$$
\begin{aligned}
p_1': \frac{\partial p_1'}{\partial u_1} &= 8\epsilon - 48fu_2u_1 + 16fu_3u_4 - 8(u_2p_3 - u_3p_2) \\
&\quad -16(u_2^2 + u_3^2)u^2 - 64u_1^2(u_2^2 + u_3^2) - 16(u_2^2 + u_3^2)(u_1^2 + u_4^2) \\
\frac{\partial p_1'}{\partial u_2} &= -8fu^2 - 16f(u_1^2 + u_2^2) - 8p_3u_1 - 64u_1u_2u^2 \\
\frac{\partial p_1'}{\partial u_3} &= -16fu_2u_3 + 16fu_4u_1 + 8p_2u_1 - 64u_1u_3u^2 \\
\frac{\partial p_1'}{\partial u_4} &= -16fu_2u_4 + 16fu_3u_1 - 64u_1u_4(u_2^2 + u_3^2) \\
\frac{\partial p_1'}{\partial p_1} &= 0 \quad \frac{\partial p_1'}{\partial p_2} = 8u_3u_1 \quad \frac{\partial p_1'}{\partial p_3} = -8u_2u_1 \quad \frac{\partial p_1'}{\partial p_4} = 0 \\
p_2': \frac{\partial p_2'}{\partial u_1} &= -8fu^2 - 16f(u_1^2 + u_2^2) - 8p_3u_1 - 64u_1u_2u^2 \\
\frac{\partial p_2'}{\partial u_2} &= 8\epsilon - 32fu_1u_2 - 16f(u_2u_1 - u_3u_4) - 16p_3u_2 - 8(u_2p_3 - u_3p_2) \\
&\quad -16(u_1^2 + u_4^2)u^2 - 64u_2^2(u_1^2 + u_4^2) - 16(u_2^2 + u_3^2)(u_1^2 + u_4^2) \\
\frac{\partial p_2'}{\partial u_3} &= 16f(u_2u_4 - u_1u_3) - 8p_3u_3 + 8p_2u_2 - 64u_2u_3(u_1^2 + u_4^2) \\
\frac{\partial p_2'}{\partial u_4} &= -16fu_1u_4 + 16fu_3u_2 - 8p_3u_4 - 64u_2u_4u^2 \\
\frac{\partial p_2'}{\partial p_1} &= 0 \quad \frac{\partial p_2'}{\partial p_2} = 8u_3u_2 \quad \frac{\partial p_2'}{\partial p_3} = -4u^2 - 8u_2^2 \quad \frac{\partial p_2'}{\partial p_4} = 0 \\
p_3': \frac{\partial p_3'}{\partial u_1} &= 16fu_4u_1 - 16fu_2u_3 + 8p_2u_1 - 64u_1u_3u^2 \\
\frac{\partial p_3'}{\partial u_2} &= 16fu_4u_2 - 16fu_1u_3 + 8p_2u_2 - 8p_3u_3 - 64u_2u_3(u_1^2 + u_4^2) \\
\frac{\partial p_3'}{\partial u_3} &= 8\epsilon + 32fu_3u_4 - 16f(u_2u_1 - u_3u_4) + 16p_2u_3 - 8(u_2p_3 - u_3p_2) \\
&\quad -16(u_1^2 + u_4^2)u^2 - 64u_3^2(u_1^2 + u_4^2) - 16(u_2^2 + u_3^2)(u_1^2 + u_4^2) \\
\frac{\partial p_3'}{\partial u_4} &= 8fu^2 + 16fu_4^2 + 16fu_3^2 + 8p_2u_4 - 64u_3u_4u^2
\end{aligned}
$$

$$
\begin{aligned}
& \frac{\partial p_3'}{\partial p_1} = 0 \quad \frac{\partial p_3'}{\partial p_2} = 4u^2 + 8u_3^2 \quad \frac{\partial p_3'}{\partial p_3} = -8u_2u_3 \quad \frac{\partial p_3'}{\partial p_4} = 0 \\
p_4' : & \frac{\partial p_4'}{\partial u_1} = 16fu_3u_1 - 16fu_2u_4 - 64(u_2^2 + u_3^2)u_1u_4 \\
& \frac{\partial p_4'}{\partial u_2} = 16fu_3u_2 - 16fu_1u_4 - 8p_3u_4 - 64u_2u_4u^2 \\
& \frac{\partial p_4'}{\partial u_3} = 8fu^2 + 16fu_3^2 + 16fu_4^2 + 8p_2u_4 - 64u_3u_4u^2 \\
& \frac{\partial p_4'}{\partial u_4} = 8\epsilon + 32fu_3u_4 - 16f(u_2u_1 - u_4u_3) - 8(u_2p_3 - u_3p_2) \\
& \qquad -16(u_2^2 + u_3^2)u^2 - 64u_4^2(u_2^2 + u_3^2) - 16(u_2^2 + u_3^2)(u_1^2 + u_4^2) \\
& \frac{\partial p_4'}{\partial p_1} = 0 \quad \frac{\partial p_4'}{\partial p_2} = 8u_3u_4 \quad \frac{\partial p_4'}{\partial p_3} = -8u_2u_4 \quad \frac{\partial p_4'}{\partial p_4} = 0
\end{aligned}
$$

From (B. 31), the initial values of $\frac{\partial u_i}{\partial \theta_{out}}$, $\frac{\partial u_i}{\partial \phi_{out}}$, $\frac{\partial p_i}{\partial \theta_{out}}$, $\frac{\partial p_i}{\partial \phi_{out}}$ are

$$
\begin{aligned}
\frac{\partial u_i}{\partial \theta_{out}} &= 0, \\
\frac{\partial u_i}{\partial \phi_{out}} &= 0, \\
\frac{\partial p_1}{\partial \theta_{out}} &= -\sqrt{2}sin(\theta_{out}/2), \\
\frac{\partial p_2}{\partial \theta_{out}} &= \sqrt{2}cos(\theta_{out}/2)cos\phi_{out}, \\
\frac{\partial p_3}{\partial \theta_{out}} &= \sqrt{2}cos(\theta_{out}/2)sin\phi_{out}, \\
\frac{\partial p_4}{\partial \theta_{out}} &= 0, \\
\frac{\partial p_1}{\partial \phi_{out}} &= 0, \\
\frac{\partial p_2}{\partial \phi_{out}} &= -2\sqrt{2}sin(\theta_{out}/2)sin\phi_{out}, \\
\frac{\partial p_3}{\partial \phi_{out}} &= 2\sqrt{2}cos(\theta_{out}/2)cos\phi_{out}, \\
\frac{\partial p_4}{\partial \phi_{out}} &= 0.
\end{aligned} \tag{B.51}
$$

Appendix C

The derivation of the boundary between bound and free motions in an electric field

Here we derive the formula for the boundary between bound and free motions in an electric field. Since the pure electric field system is cylindrically symmetric with respect to the electric field direction, we can find the boundary between bound and free motions in two steps: we first find the boundary between bound and free motions in the xy plane, where the positive x direction is the electric field direction. The boundary is a line. Then we rotate the line with respect to the x axis to obtain the boundary between bound and free motions in the xyz space. The boundary becomes a surface – a cone with x axis as symmetric axis. The cone is the boundary between bound and mixture sectors in the crossed fields.

The 2-dimensional Hamiltonian of the hydrogen atom in electric field is given by:

$$H = \frac{P^2}{2} - \frac{1}{r} + Fx$$

Transforming to semiclassical coordinates which are defined as

$$\begin{aligned} x &= (u^2 - v^2)/2, \\ y &= uv, \end{aligned} \tag{C.1}$$

we obtain the regularized Hamiltonian:

$$2 = \frac{p_u^2 + p_v^2}{2} - (u^2 + v^2)E + \frac{F}{2}(u^4 - v^4). \tag{C.2}$$

This Hamiltonian can be separated into two parts:

$$p_u^2 - u^2 E + \frac{F}{2}u^4 = E_u, \tag{C.3}$$

$$p_v^2 - v^2 E - \frac{F}{2}v^4 = E_v \tag{C.4}$$

with $E_u + E_v = 2$. The u motions are bound and the v motions can be bound or free. The potential energy $U(v)$ along the v direction is:

$$U(v) = -v^2 E - \frac{F}{2}v^4.$$

It has a local maximum $U_{max} = E^2/(2F)$ at $v = \pm\sqrt{-E/F}$. If $E_v > U_{max}$, the trajectory escapes. Otherwise, it is bound. Therefore the escaping boundary is determined by

$$E_v = E^2/(2F). \tag{C.5}$$

From transformation (C.1), the u axis corresponds to the positive x axis, and v axis corresponds to the negative x axis. Therefore, launching the trajectory at the origin with azimuthal angle ϕ in the (x, y) plane is equivalent to launching the trajectory in the (u, v) along $\phi/2$ (see Fig. C.1).

At the origin, the Hamiltonian in (C.2) is simplified to

$$\frac{p_u^2 + p_v^2}{2} = 2.$$

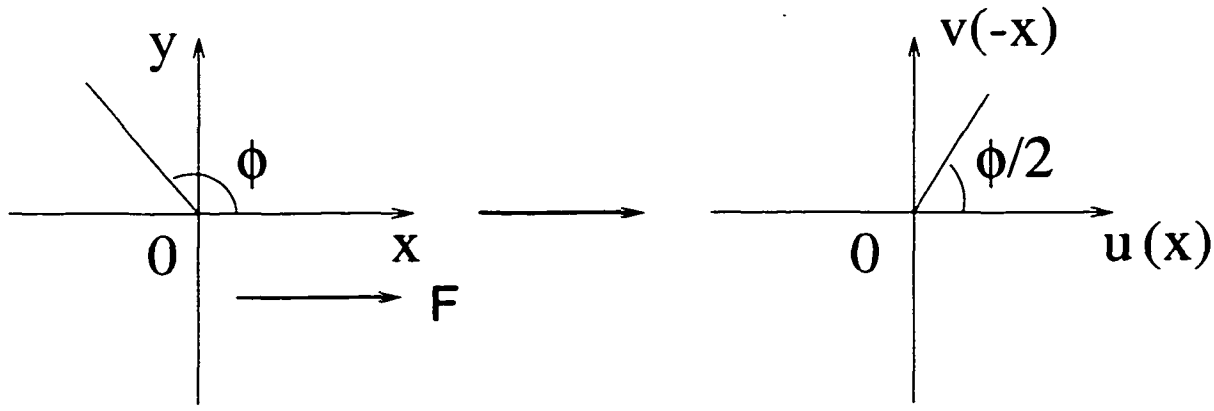

Figure C.1: The transformation from (x, y) to (u, v) projects the whole xy plane to half of the (u, v) plane. The trajectory launched at the origin with azimuthal angle ϕ in (x, y) is equivalent to the trajectory launched in (u, v) along $\phi/2$.

If we launch the trajectory along ϕ in (x, y) space, or $\phi/2$ in (u, v) space, we have

$$p_v = 2sin(\phi/2),$$

and from (C.4), E_v is given by

$$E_v = p_v^2/2 = 2sin^2(\phi/2).$$

Inserting E_v into (C.5), the escaping boundary is:

$$\phi_c = 2sin^{-1}(-E/2\sqrt{F}).$$

We now rotate the boundary defined by $\phi_c = 2sin^{-1}(-E/2\sqrt{F})$ about x axis by 2π, and we obtain a cone with the negative x axis as the symmetry axis. The angle between the ray on the cone and the positive x axis is $\phi_c = 2sin^{-1}(-E/2\sqrt{F})$ (see Fig. C.2). This cone is the boundary between bound and free sectors in a pure electric field, and we take it to be a boundary between bound and mixed sectors in crossed fields.

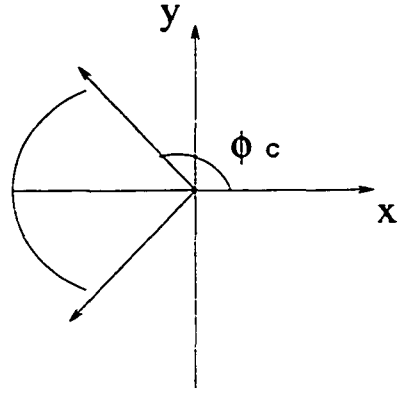

Figure C.2: The boundary of the escaping trajectories in a pure electric field is a cone with the negative x axis as symmetry axis. The angle between the ray on the cone and the positive x axis is ϕ_c.

Appendix D

Proofs of the relation (6.4) and the two theorems

We use the existence and uniqueness theorem for differential equations [35] to prove Eq. (6.4)

$$M_{-}(z_0;\epsilon,f) = -M_{+}(-z_0;\epsilon,f).$$

Proof:

- Uniqueness theorem for differential equation: If a collection of differential equations

$$\dot{\mathbf{Z}} = \begin{pmatrix} dZ_1/dt \\ dZ_2/dt \\ \vdots \\ dZ_n/dt \end{pmatrix} = \begin{pmatrix} f_1(t, Z_1, Z_2, ..., Z_n) \\ f_2(t, Z_1, Z_2, ..., Z_n) \\ \vdots \\ f_n(t, Z_1, Z_2, ..., Z_n) \end{pmatrix} = \mathbf{f}(t, \mathbf{Z}) \qquad \text{(D.1)}$$

  is defined in a continuous domain and the first derivatives $df(t,\mathbf{Z})/d\mathbf{Z}$ exist and are bounded, then there exists a unique solution $\mathbf{Z}(t,\mathbf{Z_0})$ for a given set of initial condi-

tions,

$$\mathbf{Z}(t_0) = \begin{pmatrix} Z_1^0 \\ Z_2^0 \\ \vdots \\ Z_n^0 \end{pmatrix} = \mathbf{Z}_0. \tag{D.2}$$

Therefore, if two collections of functions $\mathbf{Z}_1(t)$ and $\mathbf{Z}_2(t)$ satisfy the same collection of differential equations and $\mathbf{Z}_1(0) = \mathbf{Z}_2(0)$, then $\mathbf{Z}_1(t) = \mathbf{Z}_2(t)$.

- From Uniqueness theorem, we can prove that if the differential equations have the symmetry

$$\mathbf{f}(t, -\mathbf{Z}) = -\mathbf{f}(t, \mathbf{Z}) \tag{D.3}$$

and there are two solutions, $\mathbf{Z}_1(t, \mathbf{Z}_0)$ with $\mathbf{Z}_1(t_0) = \mathbf{Z}_0$ and $\mathbf{Z}_2(t, -\mathbf{Z}_0)$ with $\mathbf{Z}_2(t_0) = -\mathbf{Z}_0$, then $\mathbf{Z}_1(t, \mathbf{Z}_0) = -\mathbf{Z}_2(t, -\mathbf{Z}_0)$. (This is proved in theorem 1)

- Now we prove Eq. (6.4) $M_-(z_0, \epsilon, f) = -M_+(-z_0, \epsilon, f)$ by proving that the pair of maps M_+, M_- are a special case of theorem 1.

The differential equations are the equations of motion of the reduced 2-D Hamiltonian:

$$\dot{\mathbf{Z}} = \begin{pmatrix} \dot{u} \\ \dot{v} \\ \dot{p_u} \\ \dot{p_v} \end{pmatrix} = \mathbf{f}(t, \mathbf{Z}) \tag{D.4}$$

with

$$\begin{aligned} \dot{u} &= p_u - \frac{1}{4\omega^2} v(u^2 + v^2) \\ \dot{v} &= p_v + \frac{1}{4\omega^2} u(u^2 + v^2) \\ \dot{p_u} &= -u - \frac{2f}{\omega^3} u^3 - \frac{1}{4\omega^2} p_v(u^2 + v^2) \end{aligned}$$

$$
\begin{aligned}
& -\frac{1}{2\omega^2}u(up_v - vp_u) - \frac{3}{16\omega^4}u(u^2+v^2)^2 \\
\dot{p_v} \;=\; & -v + \frac{2f}{\omega^3}v^3 + \frac{1}{4\omega^2}p_u(u^2+v^2) \\
& -\frac{1}{2\omega^2}v(up_v - vp_u) - \frac{3}{16\omega^4}v(u^2+v^2)^2
\end{aligned}
$$

where all the differentiations are with respect to the fictitious time s defined in chapter 2. This collection of differential equations has the symmetry defined by Eq. (D.3). According to theorem 1, we have

$$\mathbf{Z}(s, \mathbf{Z}_0) = -\mathbf{Z}(s, -\mathbf{Z}_0) \tag{D.5}$$

Writing this out explicitly, they are:

$$u(s; u_0, p_{u_0}, v_0, p_{v_0}) = -u(s; -u_0, -p_{u_0}, -v_0, -p_{v_0}) \tag{D.6}$$

$$p_u(s; u_0, p_{u_0}, v_0, p_{v_0}) = -p_u(s; -u_0, -p_{u_0}, -v_0, -p_{v_0}) \tag{D.7}$$

$$v(s; u_0, p_{u_0}, v_0, p_{v_0}) = -v(s; -u_0, -p_{u_0}, -v_0, -p_{v_0}) \tag{D.8}$$

$$p_v(s; u_0, p_{u_0}, v_0, p_{v_0}) = -p_v(s; -u_0, -p_{u_0}, -v_0, -p_{v_0}) \tag{D.9}$$

Suppose we initiate trajectories on the $u = 0$ surface and pick initial conditions in following way: we first set $u_0 = 0$ and pick v and p_v in the energetically allowed region:

$$z_0 = \begin{pmatrix} v_0 \\ p_{v_0} \end{pmatrix}.$$

then calculate p_u via Hamiltonian (6.1), which is quadratic in p_u and there are two solutions. One of the solutions gives $\dot{u} \geq 0$ and another one gives $\dot{u} \leq 0$ (we will prove

it in theorem 2). We pick that p_u which gives $\dot{u} > 0$, and call it p_{u_0}. So we have

$$\mathbf{Z_0} = \begin{pmatrix} 0 \\ v_0 \\ p_{u_0} \\ p_{v_0} \end{pmatrix},$$

which gives us the initial conditions to calculate trajectories. We integrate the equations to obtain the solution $\mathbf{Z}(s, \mathbf{Z_0})$, stopping when $u = 0$ ($\dot{u} < 0$) to record $(v_1, p_{v_1}) = z(s, \mathbf{Z_0})$. This final value is $M_+(z_0)$ by definition.

Now we change the sign of $\mathbf{Z_0}$ and start at

$$-\mathbf{Z_0} = \begin{pmatrix} -0 \\ -v_0 \\ -p_{u_0} \\ -p_{v_0} \end{pmatrix}.$$

This initial condition gives the same value of the Hamiltonian as $\mathbf{Z_0}$, but it changes the sign of $\dot{u}$. We integrate equations to find $\mathbf{Z}(s, -\mathbf{Z_0})$, stopping when $u = 0$ ($\dot{u} > 0$) to record $(v_2, p_{v_2}) = z(s, -\mathbf{Z_0})$ which is $M_-(-z_0)$ by definition. The existence and uniqueness theorem tells us

$$\mathbf{Z}(s, -\mathbf{Z_0}) = -\mathbf{Z}(s, \mathbf{Z_0})$$

which implies

$$\begin{pmatrix} v_2 \\ p_{v_2} \end{pmatrix} = \begin{pmatrix} -v_1 \\ -p_{v_1} \end{pmatrix}$$

Hence

$$M_-(-z_0) = -M_+(z_0)$$

QED.

Theorem 1: suppose the differential equations have the symmetry

$$\mathbf{f}(t, -\mathbf{Z}) = -\mathbf{f}(t, \mathbf{Z}) \tag{D.10}$$

and there are two solutions, $\mathbf{Z_1}(t, \mathbf{Z_0})$ with $\mathbf{Z}_1(t_0) = \mathbf{Z_0}$ and $\mathbf{Z_2}(t, -\mathbf{Z_0})$ with $\mathbf{Z}_2(t_0) = -\mathbf{Z_0}$, then $\mathbf{Z}_1(t, \mathbf{Z_0}) = -\mathbf{Z}_2(t, -\mathbf{Z_0})$.

Proof: According to the uniqueness theorem, in order to prove $\mathbf{Z}_1(t, \mathbf{Z_0}) = -\mathbf{Z}_2(t, -\mathbf{Z_0})$, we only need to prove that $\mathbf{Z}_3(t) \equiv -\mathbf{Z}_2(t, -\mathbf{Z_0})$ obeys the same differential equation and initial condition as $\mathbf{Z}_1(t, \mathbf{Z_0})$.

We are given:

$$\dot{\mathbf{Z}}_1 = \mathbf{f}(t, \mathbf{Z}_1) \tag{D.11}$$

$$\mathbf{Z}_1(0, \mathbf{Z_0}) = \mathbf{Z_0}.$$

$$\dot{\mathbf{Z}}_2 = \mathbf{f}(t, \mathbf{Z}_2) \tag{D.12}$$

$$\mathbf{Z}_2(0, -\mathbf{Z_0}) = -\mathbf{Z_0}$$

We define $\mathbf{Z}_3(t) = -\mathbf{Z}_2(t, -\mathbf{Z_0})$. Then, from Eq. (D.10), the differential equation satisfied by $\mathbf{Z}_3$ is

$$\dot{\mathbf{Z}}_3 = -\dot{\mathbf{Z}}_2 = -\mathbf{f}(t, \mathbf{Z}_2) = \mathbf{f}(t, -\mathbf{Z}_2) = \mathbf{f}(t, \mathbf{Z}_3) \tag{D.13}$$

and $\mathbf{Z}_3(t_0) = \mathbf{Z_0}$. Therefore $\mathbf{Z}_3(t, \mathbf{Z_0})$ and $\mathbf{Z}_1(t, \mathbf{Z_0})$ satisfy the same collection of differential equations and the same initial conditions, hence

$$\mathbf{Z}_3(t, \mathbf{Z_0}) = -\mathbf{Z}_2(t, -\mathbf{Z_0}) = \mathbf{Z}_1(t, \mathbf{Z_0}) \tag{D.14}$$

QED.

Theorem 2: For $u = 0$ and any energetically allowed (v_0, p_{v_0}), we calculate p_u from Eq. (6.1). There are two solutions: one of them gives $\dot{u} \geq 0$ and another one gives $\dot{u} \leq 0$.

Proof: Set $u = 0$, $v = v_0$ and $p_v = p_{v_0}$ in Hamiltonian (6.1), then we obtain:

$$\frac{1}{2}p_u^2 - \frac{1}{4\omega^2}v_0^3 p_u + \frac{1}{2}p_{v_0}^2 - \frac{1}{2}v_0^2 - \frac{f}{2\omega^3}v_0^4 + \frac{1}{32\omega^4}v_0^6 - \frac{2}{\omega} = 0$$

This equation has two solutions for p_u

$$p_{u\pm} = \frac{v^3}{4\omega^2} \pm \sqrt{\Delta}$$

where

$$\Delta = b^2 - 4ac$$

with

$$\begin{aligned} a &= 1/2, \\ b &= -\frac{1}{4\omega^2}v_0^3, \\ c &= \frac{1}{2}p_{v_0}^2 - \frac{1}{2}v_0^2 - \frac{f}{2\omega^3}v_0^4 + \frac{1}{32\omega^4}v_0^6 - \frac{2}{\omega} \end{aligned}$$

Since (v_0, p_{v_0}) are energetically allowed, p_u must be real, and therefore $\Delta \geq 0$.

Now we notice that

$$\dot{u} = p_{u\pm} - \frac{v^3}{4\omega^2} = \pm\sqrt{\Delta},$$

so, for $u = 0$ and any allowed (v_0, p_{v_0}) , the calculated p_{u_+} gives $\dot{u} \geq 0$ and p_{u_-} gives $\dot{u} \leq 0$.

QED.

Appendix E

Algorithms and implementations

This research work involves lots of scientific computation and software implementations. Except for some commercial software tools, such as Mathematica, Maple, xvgr, etc. we developed the programs to find the closed orbits as well as to calculate various parameters. Some were downloaded from Internet; some were developed by ourselves. Of course, we also need to develop some shell scripts to glue them together to finish our research work. In this chapter, we will list some of them, including their purposes, interfaces, and algorithms. All of our programs are developed in Fortran 77, double precision and run in SunOS SPARC station 2.

E.1 Programs from Our Group and Internet

The advantage of downloading programs from the Internet is obvious. It is very fast, and in some cases, the programs are well tested. What we need to do is to understand their functions and their interfaces. The location to search for programs we used the most is gopher://archives.math.utk.edu:70/11/software/multi-platform/SLATEC. We learned from our research that a good use of those public resources is very important to our

research.

E.1.1 Integration program for differential equations from our group

- **Purpose:**

  This subroutine integrates a system of N first order non-linear ordinary differential equations of form $DY/Dt = F$.

- **Interface**

  DPODRT(F,N,Y,T,TOUT,RELERR,ABSERR,IFLAG,WORK,IWORK, G,REROOT,AEROOT

  - F — A function to evaluate derivatives $DY/DT = F$.
  - N — Number of equations to be integrated.
  - Y — Solution vector at time T.
  - T — Input, T is the integration starting time; output, T is the real integration stop time.
  - TOUT — Specified integration stop time. However, integration may stop before TOUT.
  - RELERR — Relative error tolerances for local error test.
  - ABSERR — Absolute error tolerances for local error test.
  - IFLAG - Indicates status of integration.
  - WORK,IWORK - Internal working places.
  - G — An input function of T, Y. Whenever $G = 0$ is satisfied, the subroutine stops.
  - REROOT — Relative error tolerances for accepting the root.
  - AEROOT — Absolute error tolerances for accepting the root.

E.1.2 The root finding program for a system of nonlinear equations

- **Purpose**

  This subroutine finds the solution of a system of N nonlinear functions with N variables by the Powell hybrid method.

- **Interface**

  HYBRD1(F,N,X,FVEC,TOL,INFO,WA,IWA)

  - F — Subroutine to calculate those function values.
  - N — The number of functions and variables.
  - X — An array of length N. On input X contains an initial estimate of the solution vector. On output X contains the final estimate of the solution vector.
  - FVEC — An output array of length N which contains the function values at the solution of X.
  - TOL — An input value to terminate the program when the relative error between X and the solution is less than tol.
  - INFO — The termination status.
  - WA — A work array of length Iwa.
  - IWA — a positive integer not less than $(N(3N + 13))/2$.

E.1.3 A nonlinear function minimization program

- **Purpose**

  This subroutine minimizes the sum of the squares of M nonlinear functions in N variables based on a modified Levenberg-Marquardt algorithm.

- **Interface**

  DNLS1E (FCN, IOPT, M, N, X, FVEC, TOL, NPRINT, INFO, IW, WA, LWA)

  - FCN — The sum of the squares of M nonlinear functions.
  - IOPT — An input variable which specifies how the Jacobian will be calculated.
  - M — The number of the functions.
  - N — The number of the variables.
  - X — An array of length N. On input, X contains an initial estimate of the solution vector. On output, X contains the final estimate of the solution vector.
  - FVEC — An output array of length M which contains the functions evaluated at the output X.
  - TOL — A non-negative input variable. Termination occurs when the algorithm estimates either that the relative error in the sum of squares is at most TOL or that the relative error between X and the solution is at most TOL.
  - NPRINT — An integer input variable that enables controlled printing of iterates if it is positive.
  - INFO — Termination status.
  - IW — An INTEGER work array of length N.
  - WA — A work array of length LWA.
  - LWA — A positive integer input variable not less than $N(M+5)+M$ for $IOPT = 1$ and 2 or $N(N+5)+M$ for $IOPT = 3$..

E.1.4 Fast-Fourier-Transform program

- **Purpose**

  This subroutine computes the Fourier coefficients of a complex periodic sequence.

- **Interface**

  SUBROUTINE DCFFTF(N,C,WSAVE)

  - N — The length of the complex sequence C.
  - C — A complex array of length N which contains the sequence of data at input and the sequence of coefficients at output.
  - WSAVE — a double precision work array which must be dimensioned at least 4*N+15.

E.2 Programs developed by myself

The advantage of developing programs by ourselves is the flexibility. Sometimes, we cannot find the program which we want in the public resources; sometimes, the programs in the Internet can not fit our special requirements. Then we have to develop the program by ourselves. Also, most programs in the Internet are in the form of functions or subroutines. We need some programs to combine them together to satisfy our requirements. In this section, we list some of these programs.

E.2.1 General trajectory calculation program 1

- **Purpose**

  This program integrates the differential equations with initial conditions to find the trajectories as well as the surfaces of section.

- **Interface**

  SUBROUTINE TRAJ(T0,Y0,TP,YP,TSTEP,IFLAG)

  - T0 — initial integration time.

- TP — final integration time.
- Y0 — initial function values.
- YP — final function values.
- TSTEP — the time step for output.
- IFLAG — the status of the integration termination.
  - 2: overran the time limit.
  - 4: local error parameter exceeded.
  - 7: reached SOS.
  - Other: error.

- **Algorithm**

  This integration starts from the SOS $G = 0$. We first use a small step to check whether the trajectory leaves the SOS. If so, we use a big step to continue the integration, otherwise, we stop.

  1. Initiate $T0, TSTEP, Y0$.
  2. Set $T = T0, TPMO = TSTEP/100, Y = Y0, TOUTB = T + TPMO/2$.
  3. CALL DPODRT(F,N,Y,T,TOUTB,RELERR,ABSERR, IFLAG,WORK,IWORK, 1,REROOT,AEROOT).
  4. if ($IFLAG \neq 2$), give error message, return.
  5. while ($IFLAG = 2$) do

     TOUT = T + TSTEP

     CALL DPODRT(F,N,Y,T,TOUT,RELERR,ABSERR,IFLAG,WORK,IWORK,G, REROOT,AEROOT)

     print the data to a file for trajectory plot

End do

6. If ($IFLAG = 7$ and $|T - T0| > TPMO$) do

   output the data to files for trajectory plot or SOS plot.

   return

   end if

7. Otherwise, give error message, return.

E.2.2 Trajectory calculation program 2

- **Purpose**

  This program integrates the differential equations with the initial conditions to find the trajectories as well as the surfaces of section. It outputs the trajectory data at time TOUT and SOS data at $G = 0$. The program stops after it reaches the SOS a specific number of times.

- **Interface**

  SUBROUTINE POINTSOLVE(QI,PI)

  - QI — On the input, they are the initial coordinates; on the output, they are the final coordinates.
  - PI — On the input, they are the initial momenta; on the output, they are the final momenta.
  - NB — The number of times that the trajectory has intersected the surface $G = 0$.
  - NBS — The number of times that the trajectory should intersect the surface $G = 0$.

- **Algorithm**

  This integration is accomplished by calling subroutine of TRAJ(T0,Y0,TP,YP,TSTEP,IFLAG).

1. Set $T0 = 0$, $NB = 0$.

2. Set the first half of $Y0$ equal to QI and the second half of $Y0$ equal to PI.

3. call TRAJ(T0,Y0.TP,YP,TSTEP,IFLAG)

4. while ($IFLAG = 7$ and $NB < NBS$) do

   Y0=YP

   T0=TP

   call TRAJ(T0,Y0,TP,YP,TSTEP,IFLAG)

   end do

5. return

E.2.3 Simulation program

- **Purpose**

  This program calculates the Poincaré surface of section by Monte Carlo simulation.

- **Interface**

  Program SURFACE includes following variables:

  - E — Energy.
  - F — Electric field quantity.
  - B — Magnetic field quantity.
  - NTRAJ — Total number of trajectories to be calculated.
  - ITRAJ — The number of trajectories calculated.
  - NBS — Total number of times that a trajectory should intersect the surface $G = 0$.
  - NB — The number of times that a trajectory has intersected the surface $G = 0$.

- u, v, p_u, p_v — The coordinates and the momenta variables in (u.v) space.

- **Algorithm** This program involves random number generator.

  1. Input $E, F, B, NBS, NTRAJ$
  2. Input the simulation range for v and p_v.
  3. Set $ITRAJ = 0$
  4. Calculate ω and f from E, F, B.
  5. While $ITRAJ < NTRAJ$ do
     - Set $u = 0$, $\Delta = -1$.
     - While $\Delta < 0$ do

       Generate v, p_v from random number generator,

       Calculate $\Delta = 1.0/(16.0\omega^4)v^6 - 2.0(p_v^2/2.0 + v^2/2.0$

       $+1.0/(32.0\omega^4)v^6 + f/(2.0\omega^3)v^4 - 2/\omega)$
     - End do
     - Calculate p_u by $p_u = v^3/(4.0\omega^2) + \sqrt{\Delta}$
     - Set $itraj = itraj + 1$
     - Call POINTSOLVE(u, v, p_u, p_v)
  6. End do
  7. Return

E.2.4 Closed-orbit searching program 1

- **Purpose**

  This program finds the approximate initial conditions for closed orbits.

- **Interface**

  The program CLOSORBIT-APPROX includes following variables:

  - E, F — Energy and electronic field.
  - NBSMIN, NBSMAX — The minimum and maximum number of times that the closed orbits intersect the surface $G = 0$.
  - $\theta_{min}, \theta_{max}$ — The range of the out-going polar angle of the trajectories.
  - ϕ_{min}, ϕ_{max} - The range of the out-going azimuthal angle of the trajectories.
  - i_{max}, j_{max} — The maximum number of different initial polar and azimuthal angles.
  - $\Delta\theta$, $\Delta\phi$ — The step-lengths of the initial polar angle and azimuthal angle.

- Algorithm

  Basic idea: we start the trajectories with θ from 0 to $\pi/2$ at stepsize $\Delta\theta$ and ϕ from 0 to 2π at stepsize $\Delta\phi$. At each grid $(\theta_{out,i}, \phi_{out,j})$, we integrate the equations of motion until the trajectory hits the surface $G = u_1 = 0$ $NBSMIN$ times, then we record $\theta_{out,i}, \phi_{out,j}$, and $R^{nb}_{i,j} = u_1^2 + u_2^2 + u_3^2 + u_4^2$ where $nb = NBMIN$ which is the number of times that the trajectory intersects the surface. We continue the integration until u_1 returns to zero again and record the same information. Repeat the same procedure until the trajectory intersects the surface $u_1 = 0$ NBSMAX times. Then we compare $R^{nb}_{i,j}$ with its eight nearest neighbors $R^{nb}_{i+a,j+b}, (a, b = 1, 0, -1)$. If $R^{nb}_{i,j}$ is less than all of its neighbors, we interpret $(\theta_{out,i}, \phi_{out,i})$ as an approximate initial condition for a closed orbit with nb-th return.

  1. Set $\theta_{min} = 0, \theta_{max} = \pi/2$, $\phi_{min} = 0, \phi_{max} = 2\pi$, $i_{max} = 100, j_{max} = 100$, $\Delta\theta = (\theta_{max} - \theta_{min})/i_{max}, \Delta\phi = (\phi_{max} - \phi_{min})/j_{max}$.

2. Do i from 0 to i_{max}: $\theta_{out,i} = \theta_{min} + i\Delta\theta$

3. Do j from 0 to j_{max}: $\phi_{out,j} = \phi_{min} + j\Delta\phi$.

4. Calculate the initial values of (U, P) from $(\theta_{out,i}, \phi_{out,j})$, where $U = (u_1, u_2, u_3, u_4)$. $P = (p_1, p_2, p_3, p_4)$.

5. Set NBS = NBSMAX.

6. Call POINTSOLVE(U,P). Note that in POINTSOLVE, when trajectory comes back to the surface $u_1 = 0$, if $nb > NBSMIN$, we record $R_{ij}^{nb} = \sqrt{u_1^2 + u_2^2 + u_3^2 + u_4^2}$.

7. End do j.

8. End do i.

9. Do nb from NBSMIN to NBSMAX

10. Do i from 0 to i_{max}

11. Do j from 0 to j_{max}

12. Compare $R_{i,j}^{nb}$ with $R_{i+a,j+b}^{nb}$, $(a, b = 1.0, -1)$ and output $\theta_{out,i}, \phi_{out,j}, nb$ as an approximate initial condition for a closed orbit to a file.

13. end do j.

14. end do i.

15. end do nb.

E.2.5 Closed-orbit searching program 2

- **Purpose**

  This program finds the accurate initial conditions for the closed orbits.

- **Interface**

  closeorbit-accurate($\theta_{out,i}, \phi_{out,j}$)

- $\theta_{out,i}$ - The approximate initial polar angle of a closed orbit.
- $\phi_{out,j}$ - The approximate initial azimuthal angle of a closed orbit.
- nb - The number of times which the trajectory passes through the surface $G = 0$.

- **Algorithm**

  For each approximate initial $(\theta_{out,i}, \phi_{out,j}, nb)$, we define two nonlinear equations $u_2(\theta, \phi) = 0, u_3(\theta, \phi) = 0$ in the area with $\theta \in [\theta_{out,i} - \Delta\theta, \theta_{out,i} + \Delta\theta]$ and $\phi \in [\phi_{out,j} - \Delta\phi, \phi_{out,j} + \Delta\phi]$ and try to find the solution by calling HYBRD1. If we find such a solution and u_4 is also zero (to some tolerance) at that point, this local zero gives us a closed orbit.

  1. Read the approximate initial $(\theta_{out,i}, \phi_{out,j}, nb)$ from a data file.
  2. Set n = 2, NBS=nb, TOL = 1.0D-12, LWA = 180.
  3. Define x(n) and set $x(1) = \theta_{out,i}, x(2) = \phi_{out,j}$.
  4. CALL HYBRD1(FCN,N,X,FVEC,TOL,INFO,WA,LWA).
  5. If $INFO = 1$, then $(\theta_{out,i} = x(1), \phi_{out,i} = x(2))$ gives the accurate initial conditions for a closed orbit with nb-th return.
  6. Else Error message.
  7. Return

E.3 Closed-orbit parameter calculation subroutine

- **Purpose**

  This program integrates a closed orbit with two of its neighbors to calculate the classical action, classical amplitude, Maslov index and return angles of the closed orbit.

- **Interface**

  SUBROUTINE CLOSEDORB(θ_1,ϕ_1,θ_2,ϕ_2, θ_3,ϕ_3)

  - θ_1, ϕ_1 — The initial polar and azimuthal angles of a closed orbit.
  - θ_2, ϕ_2 — The initial polar and azimuthal angles of a neighbor of the closed orbit, which has the same azimuthal angle as the closed orbit.
  - θ_3, ϕ_3 — The initial polar and azimuthal angles of a neighbor of the closed orbit, which has the same polar angle as the closed orbit.
  - NB — The number of times that the trajectory has intersected the surface $G = 0$.
  - NBS — The number of times that the trajectory should intersect the surface $G = 0$. .

- **Algorithm**

  This calculations is accomplished by calling subroutine of TRAJ(T0,Y0,TP,YP,TSTEP,IFLAG).

  1. Calculate U, P from θ_1, ϕ_1 with $U = (u_1, u_2, u_3, u_4)$ and $P = (p_1, p_2, p_3, p_4)$.
  2. Set $Y0(i) = u_i$ with $i = 1, 2, 3, 4$, $Y0(i+4) = p_i$ with $i = 1, 2, 3, 4$.
  3. Calculate U, P from θ_2, ϕ_2 with $U = (u_1, u_2, u_3, u_4)$ and $P = (p_1, p_2, p_3, p_4)$.
  4. Set $Y0(i+9) = u_i$ with $i = 1, 2, 3, 4$, $Y0(i+13) = p_i$ with $i = 1, 2, 3, 4$.
  5. Calculate U, P from θ_3, ϕ_3 with $U = (u_1, u_2, u_3, u_4)$ and $P = (p_1, p_2, p_3, p_4)$.
  6. Set $Y0(i+18) = u_i$ with $i = 1, 2, 3, 4$, $Y0(i+22) = p_i$ with $i = 1, 2, 3, 4$.
  7. Set $Y0(9) = 0$, $Y0(18) = 0$.
  8. Calculate the initial Jacobian from $Y0$.
  9. Set $TSTEP = 0.01$.
  10. Call TRAJ(T0,Y0,TP,YP,TSTEP,IFLAG).

11. Calculate the closed-orbit parameters.

12. Return

E.4 Least-square fit subroutine

- **Purpose**

  This program fits the numerical data to a smooth function.

- **Interface**

  Subroutine SMOOTHDATA1 includes following variables:

  - $G(i)$ - The numerical data for the variable.
  - G_{min}, G_{max} - The range of the variable.
  - $SIGNAL(i)$ - The numerical data for the function value.
  - M — The total number of the data sets $(G(i), SIGNAL(i))$.
  - N — The number of the unknown coefficients in the fit function.
  - X — An array of length N. On input, X contains an initial estimate of the unknown coefficients. On output, X contains the final estimate of the unknown coefficients.

- **Algorithm**

  We read the numerical data sets of (variable, function) from a data file, then call subroutine DNLS1E to fit the data sets to a smooth function.

  1. Set G_{min}, G_{max}
  2. set $i = 1$
  3. Read $G(i), SIGNAL(i)$ from a data file

4. While $G(i) < G_{min}$ Read $G(i), SIGNAL(i)$ from a data file

5. While $G(i) < G_{max}$ do

6. Set $i = i + 1$

7. Read $G(i).SIGNAL(i)$ from a data file

8. End do

9. Set $M = i, N = 9$

10. Set $X(i)$ with $(i = 1, ..., 9)$ to estimated values.

11. Set $IOPT = 1$, $LWA = N(M + 5) + M$, $NPRINT = 0$, $TOL = 1.0 \times 10^{-8}$

12. Define $FCN = \sum_{i=1}^{M}(signal(i) - f(G(i)))^2$ where $f(h) = \sum_{i=1}^{N} X(i)h^{i-1}$.

13. Call DNLS1E(FCN,IOPT,M,N,X,FVEC,TOL,NPRINT,INFO,IW,WA,LWA)

14. If $INFO = 1$, output $X(i)$ with $(i = 1, ..., N)$

15. Otherwise, give error message

16. End

E.5 Theoretical absorption spectrum calculation program

- **Purpose**

  This program calculates the theoretical absorption spectrum.

- **Interface**

  Program SPECTRUM includes the following variables::

  - E - Energy.
  - E_{min}, E_{max} - The energy range of the spectrum.
  - *ipoint* - The total data points of the spectrum in the energy range $[E_{min}, E_{max}]$.

- $A_j(E)$ - The classical amplitude of the jth closed orbit as the function of E.
- $S_j(E)$ - The classical action of the jth closed orbit as the function of E.
- $\mu_j(E)$ - The Maslov index of the jth closed orbit as the function of E.
- $NTRAJ$ - Total number of the closed orbits included in the spectrum calculation.
- Df_{Re}, Df_{Im} - The real, imaginary part of the spectrum

- **Algorithm**

We first call subroutine SMOOTHDATA1 to find the $A(E), S(E), \mu(E)$ for each closed orbit, then calculate the spectrum.

1. Set $NTRAJ = 20, i = 1, \hbar = 1.120901$
2. While $i \leq NTRAJ$ do
3. Open the file for the classical amplitude for the ith closed orbit
4. Call SMOOTHDAT1
5. Open the file for the classical action for the ith closed orbit
6. Call SMOOTHDATA1
7. Open the file for the Maslov index for the ith closed orbit
8. Call SMOOTHDATA1
9. End do
10. Set $E_{min}, E_{max}, ipoints, \Delta E = (E_{max} - E_{min})/ipoints$
11. $i = 0$
12. While $i \leq ipoints$ do
13. Set $E = E_{min} + \Delta E, Df_{Re} = 0, Df_{Im} = 0$
14. $j = 1$

15. While $j \leq NTRAJ$ do

    - $Df_{Re} = Df_{Re} + A_j(E)cos(S_j(E)/\hbar + \mu_j(E)\pi/2)$
    - $Df_{Im} = Df_{Im} + A_j(E)sin(S_j(E)/\hbar + \mu_j(E)\pi/2)$
    - $j = j + 1$

16. End do j

17. Output E, $\sqrt{Df_{Re}^2 + Df_{Im}^2}$ to the spectrum data file

18. $i = i + 1$

19. End do i

20. return

E.6 Lifetime calculation program

- **Purpose**

  This program calculates the lifetimes of the trajectories in the escape and mixture sectors.

- **Interface**

  Subroutine LIFETIME includes following variables:

  - E - Energy.
  - F - Electric field.
  - B - Magnetic field.
  - $\theta_{min}, \theta_{max}$ - The range of the polar angle for the trajectories in the escape and mixture region.
  - θ', ϕ' - The outgoing polar and azimuthal angles of a trajectory in (x', y', z') space.

- NBS - The total number of times that a trajectory crosses the surface $G = 0$.
- n_ϕ - The number of the trajectories with the same θ' and different ϕ'.

- **Algorithm**

We call the subroutine POINTSOLVE to calculate the lifetimes of the trajectories.

1. Set E, F, B
2. Set $\theta_{max} = \pi - 2arcsin(E/(2\sqrt{F})), \theta_{min} = 0$
3. Set $\Delta\theta = \pi/180, \theta' = \theta_{min}$
4. While $\theta' \leq \theta_{max}$ do
5. Set $n_\phi = \Delta\theta/(2sin\theta'), i_\phi = 0$
6. While $i_\phi \leq n_\phi$ do
   - Set $\phi' = (2\pi/n_\phi)i_\phi$
   - Calculate the initial coordinates $U = (u_1, u_2, u_3, u_4)$ and initial momenta $P = (p_1, p_2, p_3, p_4)$.
   - Call POINTSOLVE(U,P)
   - Record θ', ϕ', T
   - Set $i_\phi = i_\phi + 1$
7. End do i_ϕ
8. Set $\theta' = \theta' + \Delta\theta$
9. End do θ'
10. End

E.7 Continuum calculation program

- **Purpose**

  This program calculates the continuum absorption.

- **Interface**

  Program CONTINUUM includes following variables:

  - Δ_E - The step-length of E.
  - T_{crit} - The critical lifetime.
  - Df_{cont} - The calculated continuum.
  - E_{min}, E_{max} - The energy range of the continuum absorption to be calculated.

- **Algorithm**

  We read the outgoing angles and lifetimes of the trajectories from a data file, then include the trajectories with lifetime $T \leq T_{crit}$ to calculate the continuum absorption.

  1. Set $T_{crit} = 25, E_{min}, E_{max}, \Delta E$
  2. Set $E = E_{min}$
  3. While $E \leq E_{max}$ do
     - Open the file which record the lifetimes of the trajectories at E
     - Read data
     - Calculate the continuum absorption Df_{cont} with $T < T_{crit}$.
     - Record E, Df_{cont}
     - $E = E + \Delta E$
  4. End do

5. Return

E.8 Measured absorption spectrum convolution program

- **Purpose**

  This program convolutes the measured absorption spectrum to obtain the large scale structures in the absorption spectrum.

- **Interface**

  Subroutine INT-SPECTRA includes following variables:

  - E_{min}, E_{max} - The energy range.
  - $ipoints$ - The total number of data points in the convoluted spectrum.
  - Df_{int} - The convoluted spectra.
  - $E(i), SIGNAL(i)$ - The data sets
  - $nmax$ - The total number of the data sets.
  - δ - The width of the Gaussian function.

- **Algorithm**

  We replace each data point in the measured absorption spectrum with a Gaussian function. Then the sum of the contributions from all of the Gaussian functions at E gives the convoluted spectrum at E.

  1. Set E_{min}, E_{max}
  2. Read $E(i), SIGNAL(i)$ from data file with $E_{min} \leq E(i) \leq E_{max}$
  3. $\Delta E = (E_{max} - E_{min})/nmax$
  4. $j = 1$

5. While $j < ipoints$ do

6. $E = E_{min} + \Delta E, Df_{int} = 0$

7. $i = 1$

8. While $i < nmax$ do

   - $Df_{int} = Df_{int} + SIGNAL(i) \cdot exp[-(E(i) - E)^2/(2.0\delta^2)]$

   - Set $i = i + 1$

9. End do i

10. Output data E, Df_{int} into the convoluted spectrum data file

11. Set $j = j + 1$

12. End do j

13. Return

E.9 Chirped-Fourier-Transform program

- **Purpose**

  This program carries out the Chirped-Fourier-Transform to extract the closed orbits from the measured absorption spectrum.

- **Interface**

  The Program FOURIER-CHIRP includes the following variables:

  - E_{min}, E_{max} - The energy range.

  - T_{min}, T_{max} - The range of the time.

  - ΔT - The steplength of the time.

  - F_{Re} - The real part of the Fourier spectra.

- F_{Im} - The imaginary part of the Fourier spectra.
- $E(i), SIGNAL(i)$ - The measured data sets.
- $nmax$ - The total number of the data sets.
- α, β, γ - The parameters in the Chirped-Fourier-Transform.

- **Algorithm**

We read the data sets from the file, then do the Chirped-Fourier-Transform.

1. Set E_{min}, E_{max}
2. $E_{avg} = (E_{max} + E_{min})/2$
3. Set $T_{min}, T_{max}, \alpha, \beta, \gamma$
4. Read $E(i), SIGNAL(i)$ from data file with $E_{min} \leq E(i) \leq E_{max}$
5. Set $T = T_{min}$
6. While $T \leq T_{max}$ do
7. Set $i = 1, F_{Re} = 0, F_{Im} = 0$
8. While $i \leq nmax$ do
   - Set $h = T(E(i) - E_{avg})1.120901 + \alpha(E(i) - E_{avg})^2 + \beta(E(i) - E_{avg})^3$
   - $F_{Re} = F_{Re} + SIGNAL(i) \cdot cos[h(E(i) - E(i-1))] \cdot exp[-\gamma(E(i) - E_{avg})]$
   - $F_{Im} = F_{Im} + SIGNAL(i) \cdot sin[h(E(i) - E(i-1))] \cdot exp[-\gamma(E(i) - E_{avg})]$
   - Set $i = i + 1$
9. End do i
10. Output data T, $\sqrt{F_{Re}^2 + F_{Im}^2}$
11. $T = T + \Delta T$
12. End do T
13. End

E.10 The equal steplength time series calculation program

- **Purpose**

  This program calculates the time series of $x(t), y(t), z(t), p_x(t), p_y(t), p_z(t)$ of a regular trajectory.

- **Interface**

  The Program ORBIT3D includes following variables:

  - E, F, B - energy, electric field, magnetic field.
  - NBS - The number of times that the trajectory should pass through the surface $G = 0$, which is equal to the total number of the data sets (t, x).
  - nb - The number of times that the trajectory has passed through the surface $G = 0$.
  - u_i, p_i - The coordinates and momenta.
  - x_r - The x coordinate at the crossing between the stable periodic orbit and the x axis.
  - θ, ϕ - The ejection angles of the regular trajectory.
  - ΔT - The time steplength.

- **Algorithm**

  We obtain the equal step time series by calling the subroutine POINTSOLVE(u_i, p_i) and defining the surface as $G = T/(2\pi) - \Delta T \cdot nb = 0$. The time step is ΔT in the unit of 2π.

  1. Set E, F, B
  2. Set x_r, θ, ϕ

3. Calculate u_i, p_i with $i = (1, 2, 3, 4)$ from $x = x_r, y = 0, z = 0, \theta, o$

4. Set $NBS = 130000$

5. Set $\Delta T = 0.01$

6. Calculate x, y, z, p_x, p_y, p_z from u_i, p_i

7. Output $(0, x)$ to the file (orbit-x.d) for the time series of x; output $(0, y)$ to the file (orbit-y.d), output $(0, z)$ to the file (orbit-z.d); output $(0, p_x)$ to the file (orbit-p_x.d), output $(0, p_y)$ to the file (orbit-p_y); output $(0, p_z)$ to the file (orbit-p_z).

8. Call POINTSOLVE($u_1, u_2, u_3, u_4, p_1, p_2, p_3, p_4$)

   (This subroutine pauses at $G = 0$, calculates x, y, z, p_x, p_y, p_z from u_i, p_i, then outputs $(T/2\pi, x), (T/2\pi, y), (T/2\pi, z), (T/2\pi, p_x), (T/2\pi, p_y), (T/2\pi, p_z)$ to the corresponding time series data files.)

9. End

E.11 Torus's fundamental frequencies calculation program 1

- **Purpose**

  This program calculates the Fourier Transform of $x(T), y(T), z(T)$ by the Fast-Fourier-Transform method for identifying the approximate locations of the fundamental frequencies.

- **Interface**

  The Program FREQUENCY-FFT includes following variables:

  - N - The total number of data sets in a data file.
  - $K, a(i)$ - The parameters in the Window function B.
  - ΔT - The time step-length.

- T - The maximum time T.
- u_i, p_i - The coordinates and momenta.
- x_r - The x coordinate at the crossing point between the stable periodic orbit and the x axis.
- θ, ϕ - The ejection angles of the regular trajectory.
- $BB(i)$ - The values of the window function.
- $COE(i)$ - The input complex data.
- $SQTM1$ - The unit of the imaginary number.

- **Algorithm**

We multiply the signal by a window function B, then call the Fast-Fourier-Transform subroutine DCFFTF.

1. Setup all parameters
2. Calculate the window function values $BB(i)$.
3. Read data (T, x) from the orbit data file (orbit-x.d)
4. Output data $(T, x \cdot BB(i))$ to the data file (orbit-xb.d)
5. $COE(i) = CMPLX(x \cdot BB(i), 0)$
6. Call DCFFTF(N,COE,WSAVE)
7. Set $j = 0$
8. While $j < N$ do
9. $Re = REAL(COE(j)/N)$
10. $Im = REAL(COE(J)/NSQTM1)$
11. $xx = \sqrt{Re^2 + Im^2}$, $\theta = arctan(Im/Re)$

12. Output $j/(2\pi T), xx, \theta$ to the file (output-x.d)

13. Set $j = j + 1$

14. End do

15. Read data (T, y) from the data file (orbit-y.d)

16. Output data $(T, x \cdot BB(i))$ to the data file (orbit-yb.d)

17. $COE(i) = CMPLX(y \cdot BB(i), 0)$

18. Call DCFFTF(N,COE,WSAVE)

19. Set $j = 0$

20. While $j < N$ do

21. $Re = REAL(COE(j)/N)$

22. $Im = REAL(COE(J)/NSQTM1)$

23. $yy = \sqrt{Re^2 + Im^2}$, $\theta = arctan(Im/Re)$

24. Output $j/(2\pi T), yy, \theta$ to the file (output-y.d)

25. Set $j = j + 1$

26. End do

27. Read data (T, z) from the data file (orbit-z.d)

28. Output data $(T, z \cdot BB(i))$ to the data file (orbit-zb.d)

29. $COE(i) = CMPLX(z \cdot BB(i), 0)$

30. Call DCFFTF(N,COE,WSAVE)

31. Set $j = 0$

32. While $j < N$ do

33. $Re = REAL(COE(j)/N)$

34. $Im = REAL(COE(J)/NSQTM1)$

35. $zz = \sqrt{Re^2 + Im^2}$, $\theta = arctan(Im/Re)$

36. Output $j/(2\pi T), zz, \theta$ to the file (output-z.d)

37. Set $j = j + 1$

38. End do

39. End

E.12 Torus's fundamental frequencies calculation program 2

- **Purpose**

  This program calculates the Fourier transform data near one fundamental frequency.

- **Interface**

  The subroutine SFOURE1(ff) includes following variables:

  - ff - The approximate location of the fundamental frequency.
  - f_{min}, f_{max} - The frequency range of the Fourier transform.
  - $E(i), SIGNAL(i)$ - The input data sets.
  - F_{Re}, F_{Im} - The real and imaginary parts of the Fourier transform.
  - Δf - The steplength of the frequency.
  - $nmax$ - The number of the data sets.

- **Algorithm**

  We obtain the Fourier Transform data in the range $[ff - 0.001, ff + 0.001]$ in two steps: we first calculate the Fourier transform data in the range $[ff - 0.01, ff + 0.01]$ and update ff to the frequency of the local maximum in this range; then calculate

the Fourier transform data in the range $[ff - 0.001, ff + 0.001]$. This program uses Quadrature-Fourier-Transform.

1. Set $f_{min} = ff - 0.01$, $f_{max} = ff + 0.01$, $\Delta f = 0.0001$
2. Read the data $(E(i), SIGNAL(i))$ from the data file
3. Set $f = f_{min}$
4. While $(f < f_{max})$ do
5. Set $F_{Re} = 0$, $F_{Im} = 0$, $signal_{max} = 0.0$
6. $F_{Re} = \sum_{i=1}^{nmax} SIGNAL(i)cos(f \cdot E(i))$
7. $F_{Im} = \sum_{i=1}^{nmax} SIGNAL(i)sin(f \cdot E(i))$
8. $FF = \sqrt{F_{Re}^2 + F_{Im}^2}$
9. If $(signal_{max} < FF)$, Set $ff = f$, $signal_{max} = FF$
10. $f = f + \Delta f$
11. End do f
12. Set $f_{min} = ff - 0.001$, $f_{max} = ff + 0.001$, $\Delta f = 0.00001$
13. $f = f_{min}$
14. While $(f < f_{max})$ do
15. Set $F_{Re} = 0$, $F_{Im} = 0$
16. $F_{Re} = \sum_{i=1}^{nmax} SIGNAL(i)cos(f \cdot E(i))$
17. $F_{Im} = \sum_{i=1}^{nmax} SIGNAL(i)sin(f \cdot E(i))$
18. $FF = \sqrt{F_{Re}^2 + F_{Im}^2}$
19. Output (f, FF) to the file
20. $f = f + \Delta f$

21. End do f

22. Return

E.13 Torus's fundamental frequencies calculation program 3

- **Purpose**

  This program calculates the Fourier transform data near three fundamental frequencies.

- **Interface**

  The Program FREQUENCY-3 includes following variables:

  - f_1, f_2, f_3 - Three fundamental frequency.
  - f_{1min}, f_{1max} - The approximate range for f_1
  - f_{2min}, f_{2max} - The approximate range for f_2
  - f_{3min}, f_{3max} - The approximate range for f_3

- **Algorithm**

  This program first calls FREQUENCY-FFT to find the approximate locations of the three fundamental frequencies f_1, f_2, f_3, then calls SFOURE1 three times to find the accurate accurate fundamental frequencies.

  1. Call FREQUENCY-FFT to find the approximate locations of three fundamental frequencies f_1, f_2, f_3.
  2. Call SFOURE1(f_1)
  3. Call SFOURE1(f_2)
  4. Call SFOURE1(f_3)
  5. return

E.14 Torus's action variables calculation program

- **Purpose**

  This program calculates amplitudes and phases of the harmonics in the Fourier series of $x(T), y(T), z(T), p_x(T), p_y(T), p_z(T)$.

- **Interface**

  The Program ACTION-3D includes following variables:

  - $WC(i)$ — The parameters in the shape function.
  - SQTM1 — The unit complex number.
  - f_i — Fundamental frequencies.
  - $\omega(n, j)$ - The nth harmonic.
  - nf - The total number of the harmonics.
  - $WW(i)$ - The values of the window function.
  - $S(i)$ — The action variables of a regular torus.

- **Algorithm**

  We first call subroutine SMOOTHDATA1 to fit the data files frequency-1.d, frequency-2.d, frequency-3.d with Gaussian functions $x(1)exp[-x(2)(E(i) - x(3))^2]$ to find the fundamental frequencies which are given by $x(3)$; then find all the harmonics $f = k_1 f_1 + k_2 f_2 + k_3 f_3$ with $|k_1| \leq 8, |k_2| \leq 5, |k_3| \leq 3$. Finally we call the subroutine DCFFTF to calculate the amplitude and the phase at each of the harmonics in the Fourier series of $x(T), y(T), z(T), p_x(T), p_y(T), p_z(T)$.

  1. Open data file fundamental-1.d
  2. Call SMOOTHDATA1 to find f_1

3. Open data file fundamental-2.d

4. Call SMOOTHDATA1 to find f_2

5. Open data file fundamental-3.d

6. Call SMOOTHDATA1 to find f_3

7. Set nf=1

8. Do k_1 from -8 to 8, k_2 from -5 to 5, k_3 from -3 to 3

9. $ff = k_1 f_1 + k_2 f_2 + k_3 f_3$

10. If $ff > 0$

11. $\omega(nf, 1) = ff$

12. $\omega(nf, 2) = k_1$

13. $\omega(nf, 3) = k_2$

14. $\omega(nf, 4) = k_3$

15. $nf = nf + 1$

16. End if

17. End do k_1, k_2,k_3

18. Sort the harmonics ω in ascending order

19. Calculate the window functions $WW(i)$

20. FFT on $x(T) \cdot WW(i)$

21. Calculate the amplitudes and phases of harmonics in $x(T)$

22. FFT on $y(T) \cdot WW(i)$

23. calculate the amplitudes and phases of the harmonics in $y(T)$

24. Repeat the same procedure for $z(T), p_x(T), p_y(T), p_z(T)$

25. Calculate actions $S(1), S(2), S(3)$.

26. Output actions $S(1), S(2), S(3)$ to a file.

27. Return

E.15 Simple shell scripts

- **Purpose**

  This shell program automates the action calculation procedure which includes the time series calculation, fundamental frequency calculation and action calculation.

- **Interface**

  Program RUNCMD

- **Algorithm**

  1. #!/bin/sh
  2. For ϕ in 89 88 87 86 85 84 83 82 81 80
  3. Do
  4. Echo $ ϕ | ORBIT3
  5. FREQUENCY-FFT
  6. FREQUENCY-3
  7. ACTION-3D
  8. Done

Bibliography

[1] M.L.Du and J.B.Delos, Phys. Rev A38, (a) 1896 (1988); (b) 1913 (1988).

[2] M.L.Du, Phys. Rev. A43, 256 (1989).

[3] Aaron D. Peters and J.B. Delos, Phys. Rev. A47, 3020 (1993).

[4] J.Gao and J.B.Delos, Phys. Rev. A46, 1449 (1992).

[5] M.R.Haggerty, J.Gao, and J.B.Delos, Phys. Rev. Lett. (1997).

[6] J. B. Delos and M. L. Du, IEEE Journal of Quantum Electronics, 24, 1445 (1988).

[7] Craig C. Martens and Gregory S. Ezra, J. Chem. Phys. 86, 279(1987).

[8] M. C. Gutzwiller, *Chaos in Classical and Quantum Mechanics*. Springer-Verlag (1990)

[9] P. Schmelcher and L. S. Cederbaum, Phys. Rev. A, 47, 2634(1993) show some consequences of nuclear motions. If the electron "escapes" from the proton, then both electron and proton undergo cyclotron motion and $\vec{F} \times \vec{B}$ drift. After one proton cyclotron time, they come together again. We believe that this phenomenon is not relevant to the interpretation of the present experiments.

[10] S. Freund, K. Welge, D.M. Wang, and J. Delos, "The absorption and recurrence spectra of the hydrogen atom in crossed electric and magnetic fields", to be submitted to Phys. Rev. A.

[11] Craig C. Martens and Gregory S. Ezra, J. Chem. Phys. 83, 2990(1985).

[12] E.L. Stiefel, G.Scheifele, Linear and Regular Celestial Mechanics, Springer, Berlin. 1971.

[13] Eugen Flöthmann and Karl H. Welge, Phys. Rev. A54, 1884(1996).

[14] Charles Jaffé, David Farrelly and T. Uzer, Phys. Rev. A60, 3833(1999).

[15] D. A. Sadovskii and B. I. Žhilinskii, Phys. Rev. A57, 2867(1998).

[16] H. Goldstein.*Classical Mechanics*, (Addison-Wesley 1965).

[17] Steven H. Strogatz, *Nonlinear Dynamics and Chaos*, (Addison-Wesley 1994).

[18] E. Atlee Jackson, *Perspectives of Nonlinear Dynamics*, (Cambridge University Press 1990).

[19] Alternative definitions of the Chirped-Fourier-Transform are given by G. Bonmassar and E.L. Schwartz in IEEE transactions on pattern analysis and machine intelligence 19, 1080(1997).

[20] A different method was used by M. Baranger *et al.*, Chaos 5, 261(1995).

[21] Personal communication to J. B. Delos, published in R. T. Swimm and J. B. Delos, J. Chem. Phys. 71, 1706(1979).

[22] V. Kondratovich and J. Delos, Phys. Rev. A57, 4654(1998):

[23] T.Uzer and David Farrelly, Phys. Rev. A52, R2501(1995)

[24] W. Eastes and R. A. Marcus, J. Chem. Phys. 61, 4301(1974):

[25] D. W. Noid and R. A. Marcus, J. Chem. Phys. 62, 2119(1975):

[26] D. W. Noid, M. L. Koszykowski, and R. A. Marcus, J. Chem. Phys. 73, 391(1980):

[27] Eugen Flöthmann, Dissertation, der University Bielefeld, April 1994.

[28] J. -M. Mao and J. B. Delos, Phys. Rev. A45, 1746 (1992).

[29] J. Main, G. Wiebusch, K. Welge, J. Shaw and J. B. Delos, Phys. Rev. A49, 847(1994).

[30] Michael Courtney, Hong Jiao, Neal Spellmeyer, Daniel Kleppner, J. Gao and J. B. Delos, Phys. Rev. Lett. 1538 (1995).

[31] J. Gao and J. B. Delos, Phys. Rev. A56, 356(1997).

[32] A. D. Peters, C. Jaffé, J.Gao and J. B. Delos, Phys. Rev. A56, 345(1997).

[33] J.-M. Mao, K. A. Rapelje, S. J. Blodgett-Ford, J. B. Delos, A. König and H. Rinneberg, Phys. Rev. A48, 2117(1993).

[34] J.Gao and J.B.Delos, Phys. Rev. A49, 869(1994).

[35] J.H. Hubbard and B.H. West, Differential Equations: A Dynamical Systems Approach (Springer–Verlag New York,1990(P14)).

[36] R. Cushman and D. A. Sadovskii, J. de Physique Lett. 47, 1(1999).

[37] M J Raković and Shih-I Chu, J. Phys. A30, 733(1997).

[38] Jan von Milczewski and T. Uzer, Phys. Rev. A56, 220(1997).

[39] William H. Press, Brian P. Flannery, Saul A. Teukolsky and William T. Vetterling, Numerical Recipes (Cambridge University Press, 1986(P294).

Vita

The author got her BS in Physics in Sichuan Normal University in China in 1992 and MS in Physics in Beijing Normal University in 1995. Then she taught one year in Beijing Medical University.

In 1996. she came to the United states to pursue her PhD in Physics in College of William and Mary. Her research interests focus on providing theoretical interpretation of measurements in atomic physics and nonlinear dynamics. and on developing computational methods to solve problems in this area. Under the guidance of Dr. John Delos. she realized her dream and received her PhD in four years.